Al-Cu-Fe QUASICRYSTALLINE COATINGS AND COMPOSITES STUDIED BY MECHANICAL SPECTROSCOPY

THÈSE N^{O} 2707 (2002)

PRÉSENTÉE À LA FACULTÉ SCIENCES DE BASE

SECTION DE PHYSIQUE

ÉCOLE POLYTECHNIQUE FÉDÉRALE DE LAUSANNE

POUR L'OBTENTION DU GRADE DE DOCTEUR ÈS SCIENCES

PAR

Jan FIKAR

physicien diplômé de l'Université Masaryk, Brno, République Tchèque
et de nationalité tchèque

acceptée sur proposition du jury:

Dr R. Schaller, directeur de thèse
Dr N. Baluc, rapporteur
Prof. W. Benoit, rapporteur
Prof. J. Bonneville, rapporteur
Prof. P. Stadelmann, rapporteur
Dr M. Weller, rapporteur

Lausanne, EPFL
2003

“Physics is like sex: sure,
it may give some practical results,
but that’s not why we do it.”

— Richard P. Feynman

Version abrégée

Des mesures de spectroscopie mécanique ont été effectuées dans deux types de matériaux. D'une part, dans des couches de quasicristaux décagonaux Al-Cu-Fe-Cr déposées sur acier doux, d'autre part dans des composites à matrice d'aluminium ou de magnésium renforcés par des particules quasicristallines icosaédriques Al-Cu-Fe.

Les mesures de frottement interne du substrat d'acier avec trois épaisseurs différentes de couches indiquent que le frottement interne d'un tel composite est localisé à l'intérieur de la couche quasicristalline. Les contributions dues au substrat et à l'interface sont minimes.

Le module de cisaillement mesuré en torsion augmente avec la température, tandis que le module de Young mesuré en flexion se comporte normalement. Cette anomalie du module de cisaillement est causée par le frottement sec entre les sections fissurées de la couche quasicristalline. Ce phénomène permet également d'expliquer le large maximum athermique qui est observé lors des mesures de frottement interne en fonction de la température. Un modèle quantitatif reproduisant avec succès le comportement observé est développé.

Finalement, le fond exponentiel réversible à haute température est interprété comme le début de la transition fragile-ductile qui peut être associée aux mouvements de dislocations contrôlés par des sauts collectifs de phasons dans la couche quasicristalline. L'enthalpie d'activation mesurée correspond parfaitement à la valeur déduite des essais de compression effectués sur le Al-Cu-Fe.

Des composites à matrice d'aluminium ou de magnésium renforcés par des particules Al-Cu-Fe ont été élaborés par infiltration sous pression gazeuse, et caractérisés par diffraction des rayons X, microscopie électronique, mesures de micro-dureté, ainsi que par des essais de compression.

Les spectres de frottement interne des composites présentent également un fond exponentiel à haute température, contrairement aux mesures effectuées sur la matrice seule ou renforcée par de courtes fibres d'Al_2O_3, qui présentent un comportement différent. Cette différence peut être expliquée par une transformation de phase partielle de la matrice due à la présence des particules quasicristallines.

Le fond exponentiel est probablement provoqué par le mouvement des dislocations dans la matrice, mais le rapport avec le renfort quasicristallin ne peut être ni exclu ni confirmé avec certitude.

Abstract

Mechanical spectroscopy measurements were performed on two types of materials: decagonal quasicrystalline Al-Cu-Fe-Cr coatings deposited on a mild steel substrate and aluminium or magnesium matrix composites reinforced with icosahedral quasicrystalline Al-Cu-Fe particles.

The internal friction spectra of the substrate with three different thicknesses of the coating indicate that the internal friction of such composites is mostly caused by the quasicrystalline coating and that the contributions of the steel substrate and of the interface are small.

The shear modulus measured in torsion increases with temperature, while the Young's modulus measured in flexion behaves normally. This shear modulus anomaly is interpreted as due to a solid friction between cracked segments of the quasicrystalline coating. This phenomenon can also explain the broad athermal maximum, which was found to occur in isochronal internal friction measurements. A quantitative model successfully reproducing the observed behaviour was developed.

Finally, the reversible high-temperature exponential background was interpreted as due to the onset of the brittle-to-ductile transition, which may be associated with dislocation motion controlled by collective phason flips in the quasicrystalline coating. The measured activation enthalpy is similar to the value that was deduced from compression tests performed on icosahedral Al-Cu-Fe bulk material.

Aluminium or magnesium matrix composites reinforced with icosahedral Al-Cu-Fe particles were processed by gas pressure infiltration and characterised by X-ray diffractometry, electron microscopy observations, micro-hardness measurements, and compression tests.

The internal friction spectra of these composites also show a high-temperature exponential background, while measurements of the matrix alone or of the matrix with Al_2O_3 short fibres exhibit a different behaviour. The difference can be explained by a partial phase transformation of the matrix due to the presence of the quasicrystalline particles.

The exponential background is probably caused by dislocation motion in the matrix, however, the effect of the quasicrystalline reinforcement can be neither excluded nor confirmed with certainty.

Table of Contents

Introduction

The objective of this work is to contribute to the understanding of mechanical properties of quasicrystalline coatings and composites, which represent the main potential applications of quasicrystals, by combining conventional mechanical testing with mechanical spectroscopy. The investigation is focused on quasicrystalline coatings and on aluminium or magnesium matrix composites reinforced with quasicrystalline particles.

Bulk quasicrystalline materials are extremely brittle at room temperature, which excludes any chance of their use as structural materials, although their behaviour becomes ductile enough to accommodate the plastic deformation at high temperature. Alternative ways to avoid the brittleness of quasicrystals are to disperse them into a ductile matrix or to deposit them as a coating on a substrate.

The use of an Al-Cu-Fe quasicrystalline phase as a discontinuous reinforcement to produce aluminium- or magnesium-based composites is reasonable because of the low cost of Al-Cu-Fe, its relatively low density, high thermal stability, high hardness, and compatibility with aluminium matrix.

The other properties of quasicrystals, such as their low thermal conductivity, low friction coefficient, good oxidation resistance, and high hardness are also remarkable and make them a good candidate for a surface protection and wear applications.

For investigating the origin and the properties of the defects controlling the plasticity of quasicrystals at temperatures below the brittle-to-ductile transition temperature, mechanical spectroscopy can be used as a non-destructive technique, which provides important information about the mobility of structure defects.

This work contains results of numerous mechanical spectroscopy measurements on the obtained composites and on the coatings as well. The microstructural characterisation of all the samples was carried out by scanning electron microscopy, transmission electron microscopy, and X-ray diffractometry.

A bibliographic overview is presented in the first chapter, covering the points relevant to the subject. In the second chapter, details of the experimental methods are

provided. The obtained results for the quasicrystalline coatings and for the metal matrix composites reinforced with quasicrystalline particles are presented in chapter three and four, respectively. Finally, some of the results are analysed and discussed in chapter five.

Chapitre 1

Scientific background

1.1 Recent discoveries in material science

"The matter can exist in solid, liquid, gas or plasma form; solids are either crystalline or amorphous". Such a traditional classification of possible structures of the matter seems to be nowadays a simplified description of the reality since it does not include materials as liquid crystals, bulk metallic glasses, amphiphile systems, flexible macromolecules or quasicrystals [de Gennes, 1984]. In spite of the fact that materials and their properties are studied, developed, improved and used since the origin of the humankind, new fascinating discoveries still appear. Some examples are given in the following part of this work. Apparently, the variety of nature in the field of the material science is far from being fully explored.

1.1.1 Carbon and its variants

Surprisingly, many of recent findings were accomplished while studying simple materials or even pure elements only. The extreme example of this fact is carbon. Twenty years ago, only two stable carbon solid phases were known: hexagonal graphite and diamond with the diamond lattice. Since that time at least four other possible arrangements of carbon atoms have been discovered.

The big spherical molecules of *fullerenes* (see Fig. 1.1 (a) and (b)) with typically 60 atoms were evidenced [Kroto et al., 1985] and this discovery was awarded the Nobel prize in 1996. The closed molecular structure is referred to as an atomic *microcluster*. It represents a new solid phase having exotic chemical and physical characteristics. The most important among them is an increased reaction activity. The microclusters easily

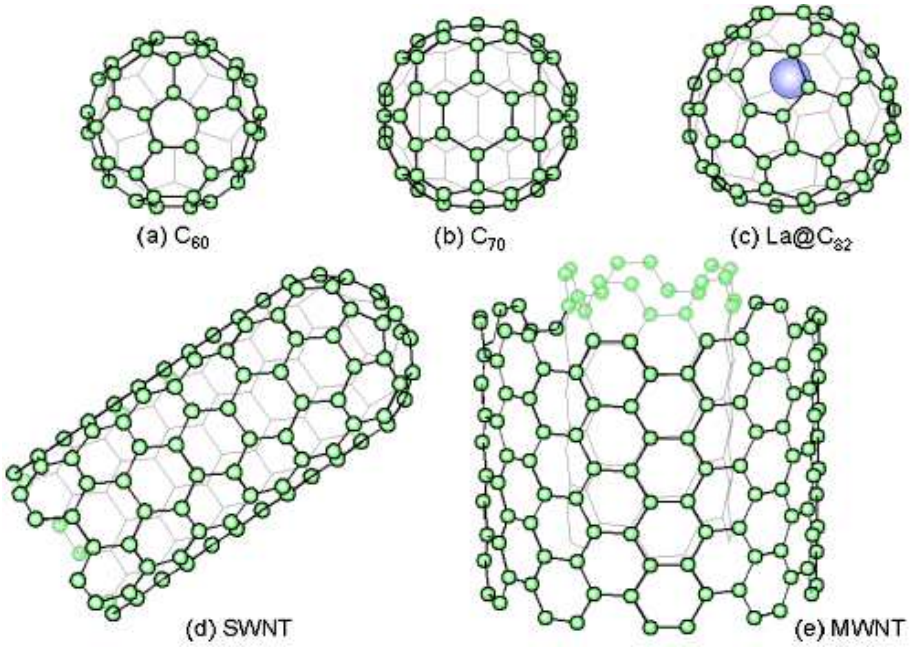

Figure 1.1: Typical structures of fullerenes and nanotubes, (a) C60, (b) C70, (c) La atom inside C82, (d) single wall carbon nanotube, (e) multi-walled carbon nanotube.

seize atoms of other substances (see Fig. 1.1 (c)) and create materials that have principally new properties. They are based on the new carbon stereo-chemistry that allows to create purposefully new organic molecules and, therefore, substances of defined forms and features.

Carbon *onions* were first observed in transmission electron microscopy. An intense electron irradiation of amorphous or graphitic specimens results first in graphitisation (when an amorphous precursor is irradiated), then in curling of the graphene planes and finally in closure, leaving perfectly spherical concentric-shell graphitic onions. The onions can be composed of C36, C180, C500, C960 etc. spheres. The pressure in the centre of such an onion increases rapidly with the number of outside layers and it can reach the level necessary for the stability of the diamond phase [Banhart and Ajayan, 1996].

Carbon *nanotubes* are fullerenes-related structures which consist of long cylinders closed at their ends with caps containing pentagonal rings (see Fig. 1.1 (d) and (e)). They were discovered in 1991 by the Japanese electron-microscopy specialist Sumio Iijima who was studying the material deposited on a cathode during arc-evaporation

synthesis of fullerenes [Iijima, 1991]. Individual nanotubes can be bundled in "nanotube ropes". This material exhibits an extremely high Young's modulus, around 1000 GPa [Salvetat et al., 1999a], which together with its small density makes possible A. C. Clarke's dream to connect the satellites on the stationary orbit with the Earth. Multi-walled carbon nanotubes, formed by coaxial cylindrical nanotubes of different diameters, were also elaborated [Salvetat et al., 1999b].

Carbyne is considered as a linear carbon allotrope with pure sp-hybridisation. Due to their unique geometrical structure, carbynes are expected to have many interesting properties as do fullerenes and carbon nanotubes. However, in contrast with the discovery of fullerenes and carbon nanotubes, the existence of carbynes has continuously been disputed since the early 1980's [Li et al., 2000].

1.1.2 High temperature superconductivity

Bednorz and Müller found in 1986 that Ba-doped $LaCuO_3$ exhibits some peculiarities indicative of a possible high temperature superconductivity [Bednorz and Müller, 1986]. This was confirmed by a direct measurement of a critical temperature of 30 K in Ba-doped La_2CuO_4 [Takagi et al., 1986]. This discovery opened the new world of high temperature superconductivity, which enabled a rapid development of new materials, as for example the famous $XBa_2Cu_3O_7$ (X refers to Y, Nb, Sm or Gd). The highest critical temperature currently reported is 135 K for a Hg-Ba-Ca-Cu-O compound.

1.1.3 Bulk metallic glasses

Unlike polymeric and network glass forming systems, the metallic supercooled liquid state has become experimentally accessible only very recently, following the discovery of *bulk metallic glasses*. They have extraordinary magnetic properties and a high thermal stability of supercooled (under-cooled) liquid with respect to crystallisation, which enables the study of thermo-physical properties of metallic melts in the supercooled state and the exploration of their properties and possible applications [Busch, 2000]. These materials exhibit a kind of short range ordering where a heavy atom is surrounded by several lighter ones in a sort of cage while these cages do not mutually form an organised structure [Ehmler et al., 1999].

In the present thesis, other recently discovered materials exhibiting a quasiperiodic long range ordered lattice, commonly called *quasicrystals*, are investigated.

Quasicrystal	Local n-fold symmetry	Cubic hyperlattices
icosahedral	5	simple, body-centred, face-centred
octagonal	8	simple, body-centred
decagonal	10	simple
dodecagonal	12	simple

Table 1.1: Quasicrystals and their symmetries.

1.2 Quasicrystals

In classical crystallography, a crystal is defined as a three-dimensional (3-D) periodic arrangement of atoms with translational periodicity along its three principal axes. Thus, it is possible to obtain an infinitely extended crystal structure by aligning building blocks called unit-cells until the space is filled up without leaving any space between the unit cells. Normal crystal structures can be divided into 230 space groups, which describe the rotational and translational symmetry elements present in the different structures. Therefore, diffraction patterns of these normal crystals show crystallographic point group symmetries[1].

In 1984, however, Shechtman, Blech, Gratias and Cahn published a paper which meant the discovery of quasicrystals [Shechtman et al., 1984]. They showed electron diffraction patterns of a rapidly solidified $Al_{86}Mn_{14}$ alloy with sharp reflections and an apparent 10-fold symmetry (see Fig. 1.2). Since then, many stable and meta-stable quasicrystals have been found. These are often binary or ternary intermetallic alloys with aluminium as one of the constituents.

The icosahedral quasicrystals form one group quasiperiodic in three dimensions with no periodic direction. The polygonal or dihedral quasicrystals are another group quasiperiodic in two dimensions with the third periodic direction perpendicular to the quasiperiodic layers (octagonal, decagonal, dodecagonal, see Tab. 1.1). It can be stated that quasicrystals are materials with a perfect long-range order but with no 3-D translational periodicity[2]. The former is manifested by the occurrence of sharp diffraction spots and the latter by the presence of a non-crystallographic rotational symmetry.

[1] belonging to one of the 11 Laue groups
[2] although they exhibit a translational quasiperiodicity

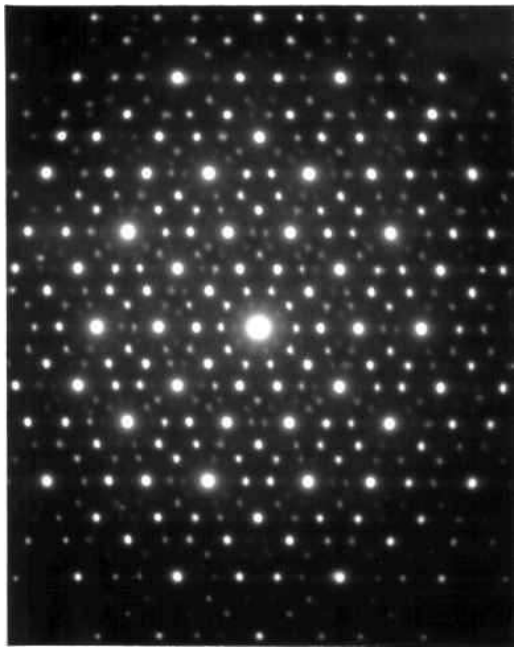

Figure 1.2: Typical transmission electron microscopy diffraction pattern of a quasicrystal, exhibiting a 5-fold or an apparent 10-fold rotational symmetry.

1.2.1 Mathematical description of quasiperiodic systems

Since quasicrystals do not exhibit any periodicity in at least one dimension, it is not possible to describe them in 3-D space as easily as normal crystal structures. It becomes hence more difficult to find mathematical formalisms for the interpretation and analysis of the diffraction data. For normal crystals three integer values (Miller indices) can be assigned to label the observable reflections. This is due to the 3-D translational periodicity of the structure. In order to apply integer indices to the diffraction patterns of quasicrystals, however, at least five linearly independent vectors are necessary. Five indices are thus needed for polygonal quasicrystals and six indices for icosahedral quasicrystals. They are called *generalised Miller indices*. The necessary n vectors span an n-dimensional (n-D) reciprocal space. Therefore, there is also an n-D direct space in which a periodic structure can be built and which gives rise to a diffraction pattern as it is observed for quasicrystals.

To explain it simply, in a higher dimensional space a quasiperiodic structure can be described as a periodic one. The actual quasiperiodic structure in the 3-D physical space can then be obtained by the appropriate projection and section techniques. Consequently, it is enough to define a single unit cell of the n-D structure whose contents

consist of "hyperatoms" (occupation domains) by analogy with the atoms in a normal unit cell. This enables to describe the whole quasicrystal structure with a finite set of parameters. If it was described in 3-D space only, thousands of atoms would be necessary to obtain a representative volume segment of the whole structure as well as all parameters that go with it (e.g. thousands of positions).

Quasiperiodicity in 1-D - Fibonacci's rabbits

Probably the first quasiperiodic ordering was proposed by Fibonacci in 1202. The original problem was to study how fast rabbits could breed in idealised circumstances. Let's admit that there exist pairs of adult rabbits A and pairs of young rabbits Y. In a given period of time, the young pairs become the adult ones and the adults give birth to new young pairs, i.e. the following transformation is done: $Y \rightarrow A$; $A \rightarrow Y + A$. Fig. 1.3 shows a few first stages, starting with one young couple. The progression 0, 1, 1, 2, 3, 5, 8, 13, 21, 34, 55, 89, 144, etc. is called the *Fibonacci series*.

Several examples of growth ruled by Fibonacci sequence can be found in nature, e.g. sunflower seeds, snail shells, cone scales, alligator scales, and human finger bones (see Fig. 1.4).

An example of quasiperiodic lattice in one dimension can be obtained by division of a 1-D line into short S and long L segments in the same order as the A and Y rabbits respectively in Fig. 1.3. The progression of S and L segments is not periodic but fully determined and the ratio L/S tends to the irrational number τ also called "golden mean" or "golden section", satisfying $\tau^2 = \tau + 1$

$$\tau = \frac{1+\sqrt{5}}{2} = 2\cos\left(\frac{\pi}{5}\right) = 1.61803398875\ldots \tag{1.1}$$

Fibonacci series can be described by the recurrent formula

$$Y_{j+1} = Y_j + Y_{j-1}, \tag{1.2}$$

where $j = 1, 2, \ldots$ and Y_0=0, $Y_1 = 1$. It can also be described by the explicit formula

$$Y_j = \frac{\tau^j - (-\tau)^{-j}}{\sqrt{5}}. \tag{1.3}$$

Then for large j the ratio $Y_j/A_j = Y_j/Y_{j-1}$ will be

$$\lim_{j\to\infty} \frac{Y_j}{Y_{j-1}} = \tau. \tag{1.4}$$

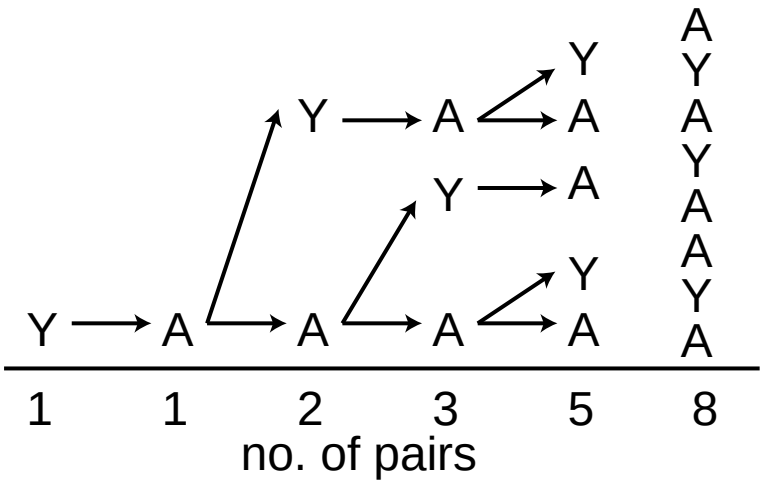

Figure 1.3: Multiplication of immortal rabbits according to Leonardo Pisano (nickname Fibonacci).

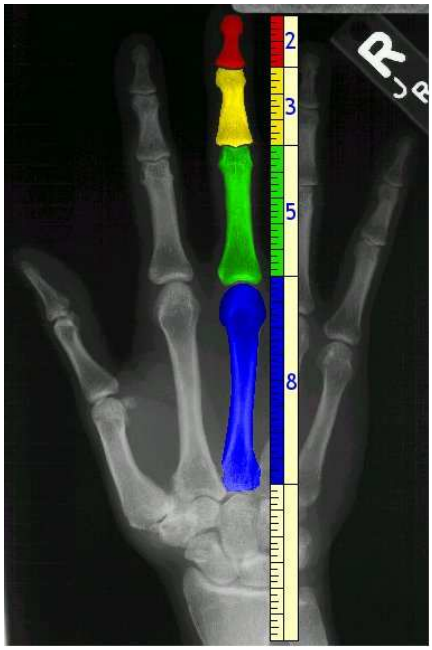

Figure 1.4: X-ray image of a human hand; when we make a fist, the fingertips form a spiral, not a circle because the lengths of the finger bones are related in a way often found in naturally occurring spirals.

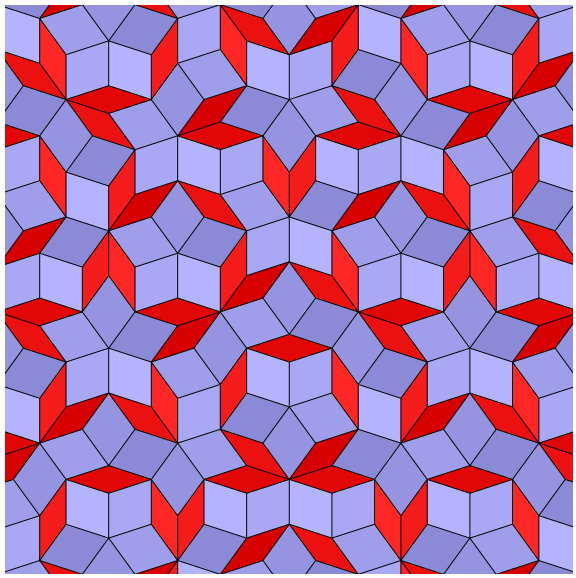

Figure 1.5: Penrose 2-D tiling.

Quasiperiodicity in 2-D

A plane can be fully covered by objects having an axis of rotational symmetry of 2 (rectangles), 3 (equilateral triangles), 4 (squares) or 6 (hexagons). This cannot be done with regular pentagons or polygons that have a number of sides higher than 6. That is why the classical crystallography allows only 2, 3, 4 and 6-fold symmetries.

If a 2-D lattice is constructed using more than one elementary cell, forbidden symmetries can appear as shown first by the British mathematician Roger Penrose [Penrose, 1974]. To construct a non-periodic covering with 5-fold symmetry, two elementary trapezoidal cells (rhombii) as in Fig. 1.5 are repeated in the 2-D space, following the matching rules defined by de Bruijn [de Brujin, 1981]. One peculiar property of such a net is its self-similarity, which means that any part of the tiling occurs again when deflated or inflated by the factor τ.

Quasiperiodicity in 3-D

The icosahedral quasicrystals got their name after the icosahedron, which is one of the five Platon's polyhedrons. It consists of 20 equilateral triangles and it possesses 15 axes of 2-fold symmetry, 10 axes of 3-fold symmetry and 6 axes of 5-fold symmetry. Again, it is not possible to fill completely the 3-D space by using only icosahedrons.

In order to keep the 5-fold symmetry at long distances, it is necessary to use generalised Penrose's trapezoids. The 3-D elementary cells are two rhombohedra [Mackay,

1981, 1982]. The 3-D Penrose tiling formed by these rhombohedra with the matching rules analogical to the 2-D case exhibits a 5-fold symmetry and is sometimes called a *"perfect" quasicrystal*.

By putting atoms at the vertices of a 3-D Penrose pattern, a Fourier transform can be obtained, which fits very well experimental diffraction patterns of icosahedral quasicrystals. In a similar way 2-D Penrose tilings can be used to approximate decagonal quasicrystals, which in a simple case consist of two layers with local 5-fold symmetry, rotated by 18° so that the projection along the rotation axis gives a 10-fold symmetry.

Geometric construction of quasiperiodic lattices

In order to construct a quasicrystalline lattice, mathematicians prefer to use a method of projection of a higher dimensional space onto a lower dimensional space rather than breed rabbits. A perfect periodical lattice in a d-D space ("hyperlattice" and "hyperspace" respectively) is cut by an n-D physical space, $n < d$. The method is illustrated in Fig. 1.6 for $d = 2$ and $n = 1$. The periodic structure in the imaginary 2-D space is cut by the "real" physical space $\mathrm{E}_{\parallel}$. The nodes appear in the physical space only if they are close enough to it[3]. This dimension is schematised as a short line at every position of the atoms in Fig. 1.6. The perpendicular space is labelled $\mathrm{E}_{\perp}$.

The type of lattice, projected onto the physical space, is given by the orientation of $\mathrm{E}_{\parallel}$ with respect to the hyperlattice. In Fig. 1.6, $\mathrm{E}_{\parallel}$ is a vector of the 2-D space and it can be defined by the two basic vectors of the hyperlattice $\vec{e_1}$ and $\vec{e_2}$. The usual notation of $\mathrm{E}_{\parallel}$ would be $\mathrm{E}_{\parallel} = p\vec{e_1} + q\vec{e_2}$, p and q being real numbers. The type of lattice in the physical space depends on the p/q ratio as follows (see Fig. 1.7):

- If the ratio p/q is rational, a periodic structure is built in the physical space. It can be a simple lattice, as in the cases of the $1/0$ and $1/1$ ratios in Fig. 1.7, where only one type of segment is concerned. In the case of the ratio $2/1$, short and long segments alter: $L, S, L, S, L, S, \ldots$. For $3/2$, the L, S, L pattern repeats: $L, S, L, L, S, L, L, S, L, \ldots$. This situation is described as a periodic lattice with the lattice parameter $a = \sqrt{p^2 + q^2}$, i.e. the distance between the nodes that form $\mathrm{E}_{\parallel}$.

- If the ratio p/q is irrational, a quasiperiodic structure is formed in the physical space. In the particular case of $p/q = \tau$, the quasiperiodic progression of L and S follows that of the Fibonacci chain.

[3] i.e. if the distance is smaller than the inter-atomic distance in the 2-D lattice

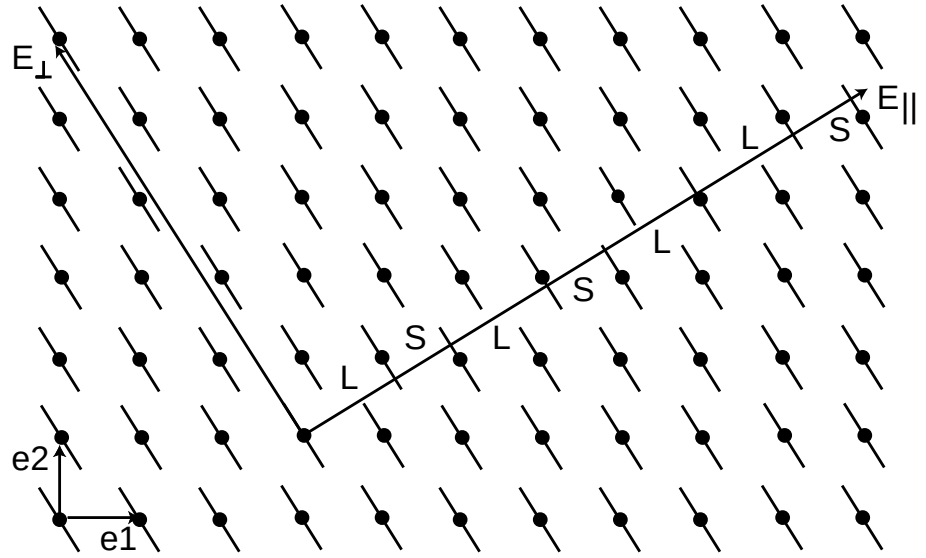

Figure 1.6: Cut and projection technique generating a quasiperiodic sequence of short S and long L line segments in the 1-D space.

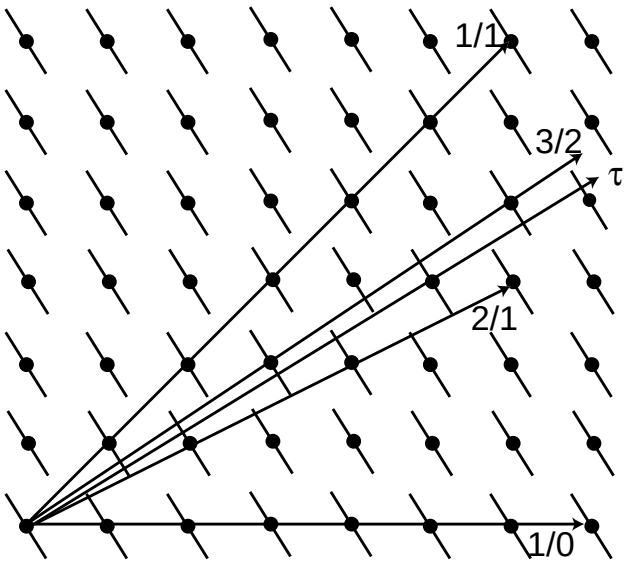

Figure 1.7: Cut and projection technique for different rational ratios of p/q which produce periodic sequences.

Approximants

The physical spaces $E_{\parallel} = 3/2$ or $E_{\parallel} = 2/1$ in Fig. 1.7 are close to the $E_{\parallel} = \tau$ space. Nevertheless, they are periodic. Such phases are referred to as *"approximant"* phases and they are often observed experimentally [Takeuchi et al., 1994]. It is sometimes difficult to prepare a single phase quasicrystalline material; a polyphase block with a quasicrystalline phase and several approximant phases are produced instead. Moreover, an approximant and the pure quasicrystalline phase can be so similar that it is difficult to distinguish between them. As the p/q ratio of the approximant comes closer to τ, the local atomic order of the periodic phase converges to the quasicrystalline one.

Since our physical space is 3-D, it is necessary to extend the method described above to $n = 3$. It was shown that it is possible to obtain a 1-D quasiperiodic arrangement from a 2-D hyperspace. If two dimensions are necessary for each of the three Cartesian axes in our 3-D physical space, the hyperspace has to be 6-D. The simplest possibility is to project a 6-D simple cubic lattice into a 3-D space along a cut with the notation $(p_1/q_1, p_2/q_2, p_3/q_3)$, where at least one p_i/q_i is irrational.

In fact, the information about the structure of the hyperspace, which is not necessarily simple cubic (see Tab. 1.1), can be obtained from 3-D diffraction patterns. 3-D diffraction patterns are the projection of diffraction patterns of the hyperspace and every diffraction peak in the 3-D space is coupled with a diffraction peak in the 6-D hyperspace. Again, only the peaks close to the cut of the 6-D reciprocal space by the 3-D reciprocal space are visible in diffractograms.

There exist several definitions of the approximant phases in 3-D; the simplest one is based on Fig. 1.7. If all p_i/q_i ratios of the $E_{\parallel} = (p_1/q_1, p_2/q_2, p_3/q_3)$ are rational, it is ensured that the vector $E_{\parallel}$ connects two nodes in 6-D. The arrangement of atoms between the two nodes can be understood as a pattern of the periodic lattice. The approximant is then composed of repeated clusters of atoms and a cluster is similar to a part of the associated quasicrystal.

The reciprocal space of an approximant with large distances between the nodes has a small elementary volume. Nevertheless, the diffracted intensity peaks of an approximant are situated at the nodes of the periodic reciprocal space, while they are at irrational positions for the perfect quasicrystal. The closer is the $(p_1/q_1, p_2/q_2, p_3/q_3)$ vector of the approximant to that of the associated quasicrystal, the closer are also the positions of the diffraction peaks.

1.2.2 Defects in quasicrystalline lattice

The arrangement of atoms in a quasicrystalline lattice may exhibit various types of defects. These defects are described in the hyperspace by analogy with the defects in periodic 3-D crystals. A defect in the hyperspace provokes a displacement field $\vec{u}$. The vector $\vec{u}$ can be written as the sum of the component $\vec{u}_{\parallel}$ parallel with $E_{\parallel}$ and the component $\vec{u}_{\perp}$ parallel to $E_{\perp}$. The component in the physical space $\vec{u}_{\parallel}$ is called in analogy with periodic crystals a *"phononic"* displacement field. The $\vec{u}_{\perp}$ is called a *"phasonic"* field, where phasons are defects which are present uniquely in quasicrystals. Dislocations, which engender both phonon and phason fields, and phasons are the two principal types of defects which control substantially the plasticity of quasicrystals.

Phasons

Phasons are defects of the hyperlattice that provoke a displacement of the hyperlattice only in the direction of $E_{\perp}$. If this displacement is uniform, it is not possible to distinguish it in the physical space. It is analogical to the motion of the physical space $E_{\parallel}$ in the direction of $E_{\perp}$ in the Fig. 1.6 - some atoms enter the physical space and others leave it, but since the direction of the $E_{\parallel}$ is not changed ($p/q = \tau$), the quasicrystals before and after the motion are indistinguishable.

When the displacement field $\vec{u}$ varies along the physical space, the quasiperiodic ordering is violated, i.e. some atoms close to $E_{\parallel}$ are translated in the $E_{\perp}$ direction. In Fig. 1.8 the physical space $E_{\parallel}$ is deformed in the perfect hyperlattice, which is more instructive. It is visible that the original pattern L, S, L, S, L, L, S is changed into S, S, L, S, L, S, L. The presence of phasons does not alter the distance between atoms, however, it changes their ordering. If the phasons change the position of only one atom, as in the 1-D example in Fig. 1.9, which results in the exchange of L and S segment[4], it is called a *"phason flip"*. Such isolated flips, as well as collective defects of numerous phasons, can appear anywhere in the quasicrystalline lattice.

The presence of phasons influences the diffraction patterns. If the phasons are randomly distributed and the corresponding $u_{\perp}$ is small, a diffusion contrast can be seen around the Bragg peaks. A strongly phasoned quasicrystal exhibits broadened and displaced Bragg peaks.

[4] or in the exchange of two Penrose trapezoids in 2-D or the exchange of two elementary rhombohedra in 3-D

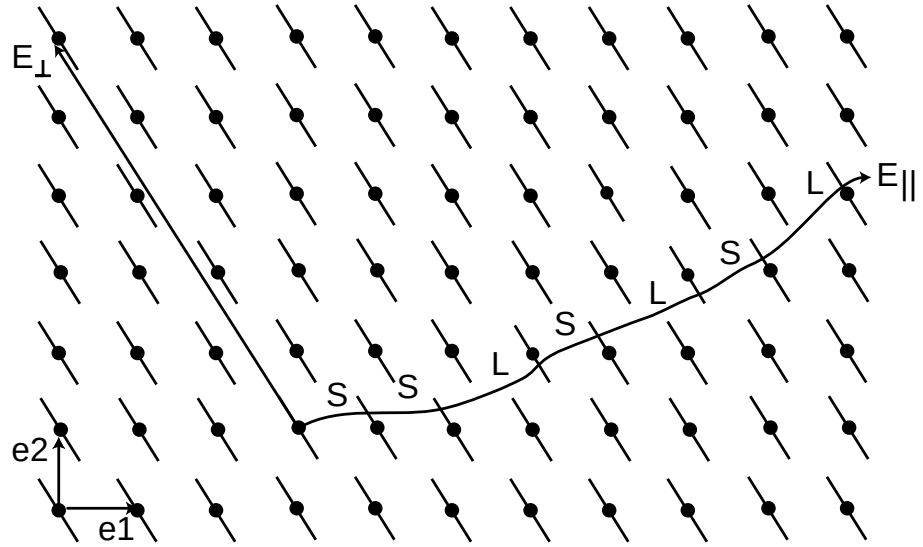

Figure 1.8: Phasonic disorder in the cut and projection technique.

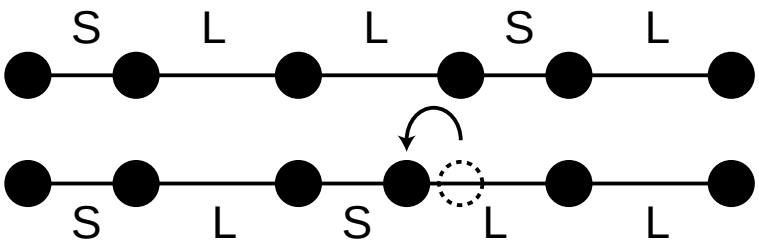

Figure 1.9: Phason flip in 1-D.

Dislocations

As in periodic crystals, dislocations in quasicrystals are characterised by a Burgers vector $\vec{B}$ and a line vector $\vec{D}$. The two vectors and the dislocation itself belong to the hyperspace. It is useful to decompose the Burgers vector into components parallel and perpendicular to the physical space

$$\vec{B} = \vec{b}_{\parallel} + \vec{b}_{\perp}. \tag{1.5}$$

The translation $\vec{b}_{\perp}$ represents a phasonic defect while $\vec{b}_{\parallel}$ represents a translation in the 3-D quasicrystal. Therefore, the dislocations in quasicrystals are generally associated with a phasonic deformation field, in addition to the usual phononic one, with no possibility to separate the two kinds of quasicrystalline defects.

Dislocations are in principle visible in the transmission electron microscope. The Burgers vector of dislocations can be found either by searching for the invisibility condition or in the convergent beam diffraction mode. The usual extinction condition[5] $\vec{g}.\vec{b} = 0$, i.e. the diffraction condition in which dislocations are invisible, is valid also in the case of quasicrystals, on condition that it is applied in the hyperspace to the 6-D diffraction vector $\vec{G}$ and the 6-D Burgers vector $\vec{B}$

$$\vec{G}.\vec{B} = \vec{g}_{\parallel}.\vec{b}_{\parallel} + \vec{g}_{\perp}.\vec{b}_{\perp} = 0. \tag{1.6}$$

In practice, dislocations are very difficult to observe in Al-Cu-Fe because their contrast is overshadowed by other strong "tweed-like" contrasts originating from various sources. On the other hand, they are easily visible in the icosahedral Al-Pd-Mn and that is why this material is so popular among researchers.

1.2.3 Indexation of icosahedral and decagonal quasicrystals

This work will follow the method proposed by [Cahn et al., 1986] which uses a system of cubic coordinates in the physical space. The choice of the coordinates is made in order to respect the symmetry of the crystal and to simplify the crystallographic formulation. Cahn *et al.* benefited from the fact that in the icosahedral point group there exist mutually perpendicular axes of 2-fold symmetry. The three cubic coordinates are chosen parallel to these axes. One disadvantage of this description is the irrationality of Miller indices. The 5-fold symmetry axes have Miller indices of the $<1, \tau, 0>$ type.

[5] $\vec{g}$ is the diffraction vector

Moreover, some axes can have both rational and irrational indices: four 3-fold symmetry axes are labelled as <1, 1, 1>, while other 6 axes of this type are referred to as $< \tau^2$, 1, 0>. Therefore, another notation with 6 indices was introduced. The irrational numbers are always in the form $n + n'\tau$, n and n' being integer numbers. Every vector $\vec{Q}$ in the reciprocal 3-D space is described by three couples of indices

$$\vec{Q} = (h + h'\tau, k + k'\tau, l + l'\tau) = (h/h', k/k', l/l'). \tag{1.7}$$

As an example, the vector $[1, \tau, 0]$ is written as $[1/0, 0/1, 0/0]$.

An alternate description uses the 6 base vectors of the elementary cube in the reciprocal 6-D hyperspace with simple cubic hyperlattice. The projections of the six vectors into the 3-D reciprocal space are the reciprocal vectors of the 6 planes with 5-fold symmetry.

The Cahn's notation $(h/h', k/k', l/l')$ will be used in the following. An example of a stereographic projection of the icosahedral structure is shown in Fig. 1.10.

The inter-planar distance d for the icosahedral Miller indices [Cahn et al., 1986] $(h/h', k/k', l/l')$ is given by

$$d(h/h', k/k', l/l') = \frac{d_0}{\sqrt{N + \tau M}}, \tag{1.8}$$

where d_0 is the 3-D quasilattice constant, which for the icosahedral Al-Cu-Fe equals to $d_0 = (17.00 \pm 0.02)$ Å [Calvayrac et al., 1990; Cornier-Quiquandon et al., 1991], N and M are the so-called "principal indices" used to index the Bragg's peaks which are related to Miller indices $h/h', k/k', l/l'$ by the equations

$$N = h^2 + k^2 + l^2 + h'^2 + k'^2 + l'^2, \tag{1.9}$$

$$M = h'^2 + k'^2 + l'^2 + 2\left(hh' + kk' + ll'\right). \tag{1.10}$$

For decagonal quasicrystals only five indices a_1, a_2, a_3, a_4, a_5 are needed as one direction is periodic[6] [Yamamoto and Ishihara, 1988]. The decagonal quasicrystals have two lattice parameters a and c corresponding to the quasiperiodic and periodic dimensions. The inter-planar distance d is then given by

$$d = \frac{1}{\sqrt{p_1^2 + p_2^2 + p_5^2}}, \tag{1.11}$$

$$p_1 = \frac{1}{a\sqrt{5}} \sum_{i=1}^{4} c_i a_i, \tag{1.12}$$

[6] corresponds to the last index a_5

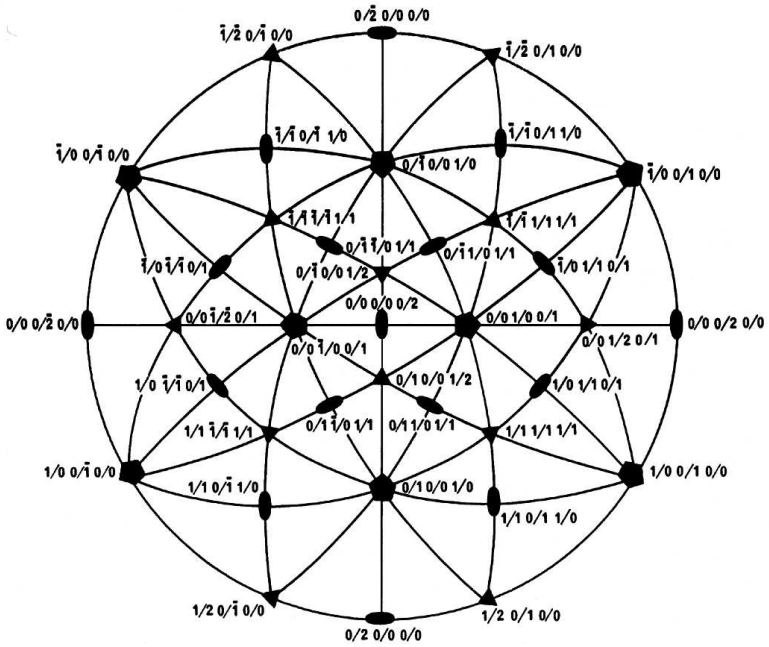

Figure 1.10: Icosahedral stereographic projection in the direction of a 2-fold axis.

$$p_2 = \frac{1}{a\sqrt{5}} \sum_{i=1}^{4} s_i a_i, \tag{1.13}$$

$$p_5 = \frac{a_5}{c}, \tag{1.14}$$

where $c_j = \cos(2\pi j/5)$ and $s_j = \sin(2\pi j/5)$ for $j = 1, 2, 3, 4$.

1.2.4 Systems with quasicrystals

Surely not complete but quite an extensive list of 1-D, 2-D and 3-D quasicrystalline phases is provided in Tabs. 1.2–1.6 [Steurer, 1990]. In most cases, the references do not refer to the discovery of the respective quasicrystals but to the papers with the most extensive experimental information. It is interesting to note that the prevailing element in the Fibonacci, decagonal and icosahedral phases is aluminium contrary to the findings for the octagonal and dodecagonal phases.

1.2.5 Properties of quasicrystals

While a large amount of theoretical and experimental research has been dedicated to the atomic structure of quasicrystals, few studies related to their physical or mechanical properties have been reported [Semadeni et al., 1997; Giacometti et al., 1999].

Material	Reference
GaAs-AlAs	[Todd et al., 1986]
Mo-V	[Karkut et al., 1986]
Al-Pd	[Chattopadhyay et al., 1987]
$Al_{80}Ni_{14}Si_6$	[He et al., 1988a]
$Al_{65}Cu_{20}Mn_{15}$	[He et al., 1988a]
$Al_{65}Cu_{20}Co_{15}$	[He et al., 1988a]

Table 1.2: Systems with 1-D quasicrystalline Fibonacci phases.

Material	Reference
$Al_{86}Mn_{14}$	[Shechtman et al., 1984]
$Al_{73}Mn_{21}Si_6$	[Gratias et al., 1988]
$Al_{65}Cu_{20}Fe_{15}$	[Tsai et al., 1988]
Al_6CuLi_3	[Mai et al., 1987]
$Al_{70}Pd_{20}Mn_{10}$	[Tsai et al., 1990]
Ti_2Fe	[Dong et al., 1986]
Ti_2Mn	[Kelton et al., 1988]
Ti_2Co	[Kelton et al., 1988]
Ti_2Ni	[Zhang et al., 1985]
Nb-Fe	[Kuo, 1987]
$V_{41}Ni_{36}Si_{23}$	[Kuo et al., 1987]
$Pd_{58.8}U_{20.6}Si_{20.6}$	[Poon et al., 1985]

Table 1.3: Systems with 3-D icosahedral phases.

Material	Reference
V_{15}-Ni_{10}-Si	[Wang et al., 1987]
Cr_5-Ni_3Si_2	[Wang et al., 1987]
Mn_4Si	[Cao et al., 1988]
$Mn_{82}Si_{15}Al_3$	[Wang et al., 1988]
Mn-Fe-Si	[Wang and Kuo, 1988]

Table 1.4: Systems with 2-D octagonal phases.

Material	Reference
Al_5Os	[Kuo, 1987]
Al_5Ru	[Bancel and Heiney, 1986]
Al_5Rh	[Wang and Kuo, 1988]
Al_4Mn	[Bendersky, 1985]
Al_4Fe	[Fung et al., 1986]
V-Ni-Si	[Fung et al., 1986]
$Al_{65}Cu_{20}Mn_{15}$	[He et al., 1988b]
$Al_{65}Cu_{20}Fe_{15}$	[He et al., 1988b]
$Al_{65}Cu_{20}Co_{15}$	[He et al., 1988b]
$Al_{75}Cu_{10}Ni_{15}$	[Zhang and Kuo, 1989]

Table 1.5: Systems with 2-D decagonal phases.

Material	Reference
$Cr_{70.6}Ni_{29.4}$-Si	[Ishimasa et al., 1985]
V_3Ni_2	[Chen et al., 1988]
$V_{15}Ni_{10}Si$	[Chen et al., 1988]

Table 1.6: Systems with 2-D dodecagonal phases.

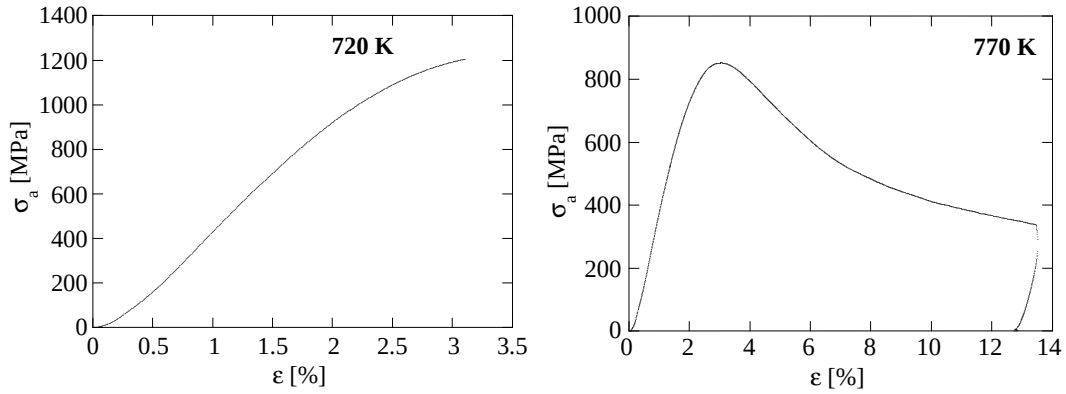

Figure 1.11: Compression stress-strain curves of icosahedral Al-Cu-Fe, brittle deformation at 720 K and ductile deformation with work hardening and yield point followed by strain softening at 770 K [Giacometti, 1999].

Quasicrystals exhibit extraordinary properties compared to common metals. Some of these properties (high hardness, low electronic and thermal conductivity - quasicrystals behave as insulators at very low temperature when their structure is perfect -, low surface energy, low fracture toughness, low friction coefficient, good oxidation and corrosion resistance, unusual optical properties) could be useful in technological applications. As far as the applications are concerned, quasicrystals suffer from a serious drawback: they are brittle materials up to a brittle-to-ductile transition temperature.

The mechanical properties of icosahedral Al-Cu-Fe have been studied in detail [Giacometti, 1999; Giacometti et al., 2000]. These quasicrystals are brittle at room temperature and they fracture before reaching the yield point by propagation of cracks or micro-cracks. A brittle-to-ductile transition was observed via compression testing between 700 K and 750 K (see Fig. 1.11). Above the transition temperature, quasicrystals become plastic and lose their hardness. Giacometti also evidenced that the plasticity at high temperature is controlled by a thermally activated mechanism of dislocation motion.

The mobility of dislocations is supposed to be inherently limited by the particular quasiperiodic structure [Guyot and Canova, 1999; Giacometti et al., 2001]. The first dislocations which pass within a slip plane have difficulties to move due to the formation of a high energy phasonic displacement field behind them. The further dislocations are moving in planes already faulted exhibiting a lower resistance to their movement. The size of the disordered region extends by diffusion at high temperatures (see Fig. 1.12). This explains the brittle behaviour at low temperatures and the ductile behaviour at

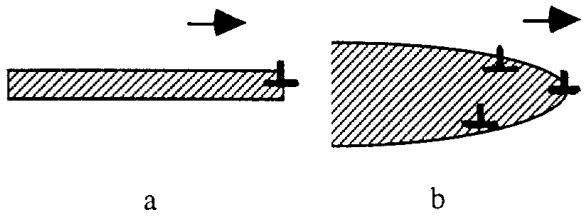

Figure 1.12: Disordered region promoting further slip activity in the wake of a leading dislocation: (a) localised disorder at low temperatures; (b) diffusion-induced extended disorder at high temperatures [Guyot and Canova, 1999].

high temperatures.

The stress strain curves exhibit an elastic stage, a work hardening stage, an upper yield point and then a softening stage (see Fig. 1.11). The upper yield point is therefore associated with a low dislocation mobility and not with a low mobile dislocation density, as for example in semiconductors. The dislocation mobility is limited by the presence of localised obstacles, intrinsic to the quasicrystalline structure. Both the density of the obstacles and the energetic barrier decrease with the increasing number of dislocations which have already overcome the barrier.

1.2.6 Possible applications

The intrinsic low-temperature brittleness of quasicrystals has confined the field of their potential applications to three main areas

- bulk materials destined to hydrogen storage [Zhang et al., 1994; Kelton and Gibbons, 1997] (see Tab. 1.7)
- thin or thick films for thermal-barrier or oxidation protection surface coatings [Besser and Eisenhammer, 1997; Kong et al., 2002]
- micro- or nano-sized particles destined to reinforcement of composites [Tsai et al., 1993; Lee et al., 2000; Fleury et al., 2001]

1.3 Mechanical spectroscopy

When the applied stress is lower than the yield stress of the particular material, it does not deform plastically. In these conditions, the deformation is composed of elastic and

Material	H/M	wt.% H	Comments
$LaNi_5$	1.1	1.5	negative electrodes in Ni metal-hydride rechargeable batteries
TiFe	0.9	1.6	best material developed for stationary applications; requires high pressure or surface activation
Mg	2.0	7.7	light, inexpensive; unloading temperature higher than typical exhaust gas from internal combustion engine
V	2.0	3.8	Expensive
$Ti_{45}Zr_{38}Ni_{17}$	1.7	2.5	initial investigations promising

Table 1.7: Comparison of hydrogen-storage properties of icosahedral Ti-Zr-Ni with metal hydrides of technological interest.

anelastic parts. The elastic part is the instant deformation response to the stress. The anelastic part, which is usually much smaller in amplitude, is time-dependent and the deformation is retarded with respect to the applied stress. Both deformations can be totally recovered. However, the anelastic part, associated with the motion of defects, results in energy dissipation.

The value of mechanical loss, also called internal friction IF, is a measure of this energy dissipation when a cyclic stress is applied. It is defined as

$$IF = \frac{1}{2\pi}\frac{\Delta W}{W}, \tag{1.15}$$

where ΔW is the energy dissipated during one cycle and W is the total stored elastic energy during one cycle.

The energy dissipation is often caused by microscopic mechanisms related to defect motion. The dynamics of the motion may depend on various parameters (amplitude, frequency of the excitation, and temperature).

The measured sample is submitted to a cyclic stress of amplitude σ_0 and angular frequency ω

$$\sigma = \sigma_0 e^{i\omega t}. \tag{1.16}$$

The mechanical response of the sample is in the form of elastic and anelastic strains

$$\varepsilon = \varepsilon_{el} + \varepsilon_{anel}, \tag{1.17}$$

where ε_{el} is the instant elastic response to the stress and is independent of the angular frequency ω, while ε_{anel} is frequency dependent. Assuming a linear relationship between the stress σ and the strain ε we obtain

$$\varepsilon = J\sigma, \tag{1.18}$$

where J is a complex dynamic compliance related to the modulus by $G = 1/J$. Then

$$\varepsilon = \varepsilon_0 e^{i(\omega t - \delta)}, \tag{1.19}$$

where the strain amplitude is $\varepsilon_0 = \sigma_0|J|$ and δ is called the mechanical loss angle. It can be easily shown that the imaginary $\Im$ and real $\Re$ parts of the modulus and compliance are related to mechanical loss angle

$$\tan\delta = -\frac{\Im J}{\Re J} = \frac{\Im G}{\Re G}. \tag{1.20}$$

The compliance and modulus are

$$J = \frac{\varepsilon_0}{\sigma_0} e^{-i\delta}, \tag{1.21}$$

$$G = \frac{\sigma_0}{\varepsilon_0} e^{i\delta}. \tag{1.22}$$

Then the dissipated energy during one cycle in a unit volume is given by

$$\Delta W = \oint \Re\sigma \, d\left(\Re\varepsilon\right) = -\pi\sigma_0^2 \Im J, \tag{1.23}$$

while the total stored elastic energy in a unit volume is

$$W = \int_0^{\sigma_0} \Re\sigma \, d\left(\Re\varepsilon_{el}\right) = \frac{1}{2}\sigma_0^2 \Re J. \tag{1.24}$$

From the equation (1.15) it follows that the internal friction equals to the tangent of the mechanical loss angle

$$\tan\delta = IF. \tag{1.25}$$

Finally, by comparison with the equation (2.31) one obtains that the tangent of the mechanical loss angle equals also to the inverse of the quality factor Q of an oscillator

$$\tan\delta = IF = Q^{-1}. \tag{1.26}$$

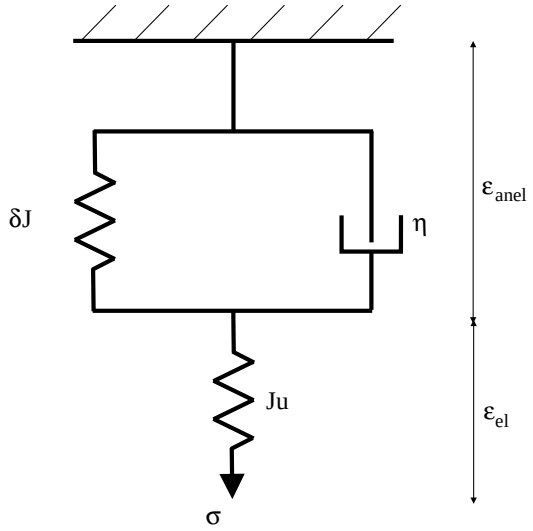

Figure 1.13: Three-parameter rheological model of a Debye standard anelastic solid.

1.3.1 Debye standard anelastic solid

The Debye standard anelastic solid is represented in Fig. 1.13 by a simple three-parameter rheological model. J_u and δJ are the compliances of the elastic springs and the dash-pot has a viscosity $\eta = \tau/\delta J$, where τ is the characteristic relaxation time. The behaviour is described by the standard anelastic solid equation [Nowick and Berry, 1972]

$$\varepsilon + \tau\dot{\varepsilon} = \sigma\left(\delta J + J_u\right) + J_u\tau\dot{\sigma}, \tag{1.27}$$

Applying a cyclic stress and using strain equations (1.16) and (1.19) one gets

$$\varepsilon = \sigma\left(J_u + \delta J\frac{1 - i\omega\tau}{1 + \omega^2\tau^2}\right). \tag{1.28}$$

With the assumption that $\delta J << J_u$, the mechanical loss is given in the following form

$$\tan\delta = \frac{\delta J}{J_u}\frac{\omega\tau}{1 + \omega^2\tau^2}. \tag{1.29}$$

The ratio $\delta J/J_u$ is often called the *relaxation strength* and noted as Δ. This equation provides a description of the so-called Debye relaxation peak. The internal friction is maximal for $\omega\tau = 1$ and reaches the value $\Delta/2$.

For thermally activated relaxation phenomena, the relaxation time follows the Arrhenius law

$$\tau = \tau_0 e^{\frac{H}{kT}}, \tag{1.30}$$

where H is the activation enthalpy of the process, k is the Boltzmann constant and τ_0 is the limit relaxation time, inverse of the attempt frequency of a defect to overcome an obstacle by thermal activation. The relaxation parameters H and τ_0 are usually calculated using an Arrhenius plot where the logarithm of the peak frequency is plotted as a function of the inverse of the peak frequency. Then the slope gives H and the intercept with the y-axis gives τ_0.

1.3.2 Internal friction of quasicrystals

Mechanical spectroscopy measurements of icosahedral Al-Pd-Mn single quasicrystals have been reported [Damson et al., 2000a]. They exhibit two mechanical loss peaks at 370 K (A) and 870 K (B) for a frequency of 3 Hz (see Fig. 1.14). The first peak A has an activation enthalpy $H = 0.98$ eV and an attempt frequency $\tau_0^{-1} = 2 \times 10^{15}\,\mathrm{s}^{-1}$ and was interpreted as due to atomic jumps enabled by isolated phason flips (see Fig. 1.15) or vacancies. The second peak B has an activation enthalpy $H = 4.0$ eV and an attempt frequency $\tau_0^{-1} = 3 \times 10^{24}\,\mathrm{s}^{-1}$ and shows a non-linear Arrhenius behaviour for higher frequencies ($f > 1$ kHz). It was attributed to a relaxation process in which the dislocation movement is controlled by the creation and movement of phason defects.

Mechanical spectroscopy of a decagonal Al-Ni-Co alloy [Damson et al., 2000b] showed a mechanical loss maximum at 870 K for a frequency of 2 kHz (see Fig. 1.16) with an activation enthalpy $H = (1.4 \pm 0.5)$ eV and an attempt frequency $\tau_0^{-1} = 10^{12}\,\mathrm{s}^{-1}$ indicative of a reorientation of atomic defects (see Fig. 1.15). A high temperature background with an activation enthalpy $H = (2.3 \pm 0.7)$ eV was assigned to a diffusion-controlled viscoelastic relaxation.

A hydrogen-induced damping peak, generally attributed to a Snoek type reorientation mechanism, was evidenced in icosahedral $Zr_{69.5}Cu_{12}Ni_{11}Al_{7.5}$ and $Ti_{53}Zr_{27}Ni_{20}$ [Sinning et al., 2002]. The hydrogen peak in Zr-Cu-Ni-Al (at 250 K for 1.1 kHz) has an activation enthalpy $H = 0.48$ eV and an attempt frequency $\tau_0^{-1} = 10^{13}\,\mathrm{s}^{-1}$. An increase of the internal friction with temperature around 600 K at 500 Hz in the form of an exponential background was evidenced in $Zr_{69.5}Cu_{12}Ni_{11}Al_{7.5}$ and it was assumed to be a sign of enhanced dynamics in the quasicrystalline phase.

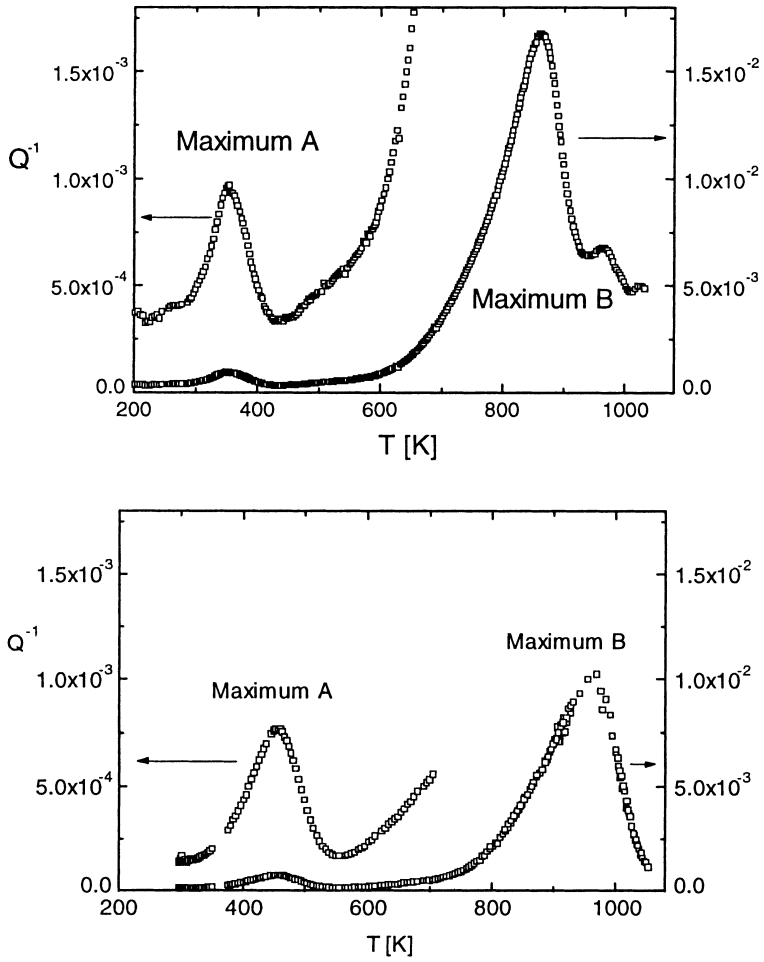

Figure 1.14: Internal friction isochronal spectra of icosahedral Al-Pd-Mn alloy for frequencies of 3 Hz (top) and 2 kHz (bottom), the left-hand side scale is 10 times larger than the right-hand one [Damson et al., 2000a,b].

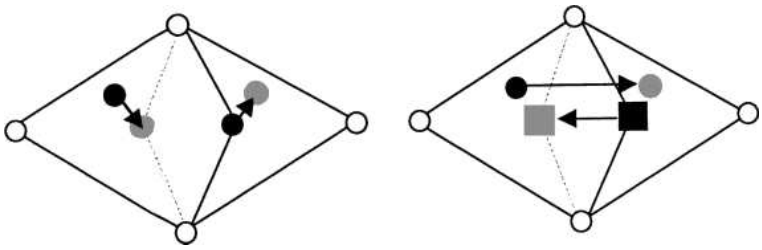

Figure 1.15: Phason flips with atomic movements as indicated by arrows without chemical order (left, two equal atoms represented by two full circles, the energy is lower than vacancy diffusion) and with chemical order (right, two different atoms represented by a full square and circle, the energy is comparable with vacancy diffusion) [Damson et al., 2000a,b].

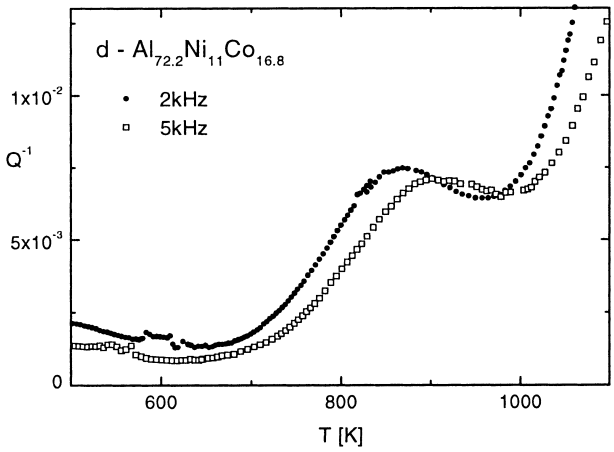

Figure 1.16: Internal friction isochronal spectra of decagonal Al-Ni-Co alloy for frequencies of 2 kHz and 5 kHz [Damson et al., 2000b].

Chapitre 2

Experimental techniques

2.1 Materials

2.1.1 Quasicrystalline coatings

Icosahedral quasicrystals of the Al-Cu-Fe system have been widely studied as coating materials on account of their stability at temperatures near the melting point, favourable cost, availability, and lack of toxicity. However, this quasicrystalline phase exists within a small range of composition [Gayle et al., 1992], which strongly affects the ability to obtain the icosahedral phase as a result of the deposition process.

Quasicrystalline coatings on steel substrates have been obtained from Sulzer Innotec AG, Switzerland. They were produced by thermal spraying and are about 500 µm thick. The substrate is a 8 mm thick mild steel plate. The deposited quasicrystalline material had the nominal composition $Al_{50.5}Cu_{22.0}Fe_{12.5}Cr_{14.5}B_{0.5}$, although according to [Gratias et al., 1993] the most stable icosahedral composition covered by patent is $Al_{62.3}Cu_{24.9}Fe_{12.8}$. The Al-Cu-Fe-Cr quasicrystals are often used as a coating material [Kong et al., 2002], they were also used in the cookware surface coating Cybernox produced by Sitram, France which became the first commercial application of quasicrystals [Sordelet et al., 2000].

Samples for mechanical spectroscopy were cut by spark machining and so the thickness of the mild steel substrate was decreased to (593 ± 10) µm.

2.1.2 Composites reinforced with quasicrystalline particles

Bulk quasicrystalline materials are extremely brittle at room temperature. At high temperature they become ductile enough to accommodate the plastic deformation. An alternative way to overcome the brittleness of quasicrystals is to disperse them into a ductile matrix in the shape of small particles.

The strong demand for aluminium alloys with improved properties has led to the development of composites, such as Al/SiC and Al/Al_2O_3 composites, used in the automotive and aerospace industries. However, the integrity of the composites depends critically on the wettability between the reinforcement material and the matrix. Furthermore, a degraded service performance at elevated temperatures and a low fracture toughness remain weak points of these composites as well as the extreme difficulty of their recycling.

Hence, the use of Al-Cu-Fe quasicrystals as a discontinuous reinforcement to produce aluminium-based composites is reasonable because of its low cost, relatively low density, high thermal stability, high hardness, and compatibility of Al-Cu-Fe with the aluminium matrix.

The Al-Cu-Fe ternary phase diagram [Gayle et al., 1992] indicates that the Al-Cu-Fe icosahedral phase never coexists with aluminium. Consequently, it is impossible to disperse Al-Cu-Fe icosahedral particles into an aluminium matrix through the usual solidification process or through a heat treatment. Nevertheless, the preparation of Al-base composite alloys reinforced with quasicrystalline particles was reported [Tsai et al., 1993]. Icosahedral Al-Cu-Fe quasicrystalline particles were homogeneously dispersed in a crystalline aluminium matrix using an innovative process which combines mechanical alloying and hot pressing techniques. They showed an improvement of the micro hardness with increasing volume fraction of the icosahedral phase in the range of 10–25%.

On the other hand, a high-strength steel with a good ductility has been produced commercially by precipitation of an icosahedral quasicrystalline phase within maraging steels [Nilsson et al., 1994].

Aluminium based composites reinforced with Al-Cu-Fe quasicrystalline powder and prepared by conventional casting or hot extrusion were produced [Lee et al., 2000; Fleury et al., 2001]. The powder was coated with a 5 µm thick Ni layer deposited by means of a non-electrolytic method to preserve the quasicrystalline structure during casting. A significant increase in the yield stress was observed via compression and indentation experiments. A much lower increase of the yield stress was obtained for

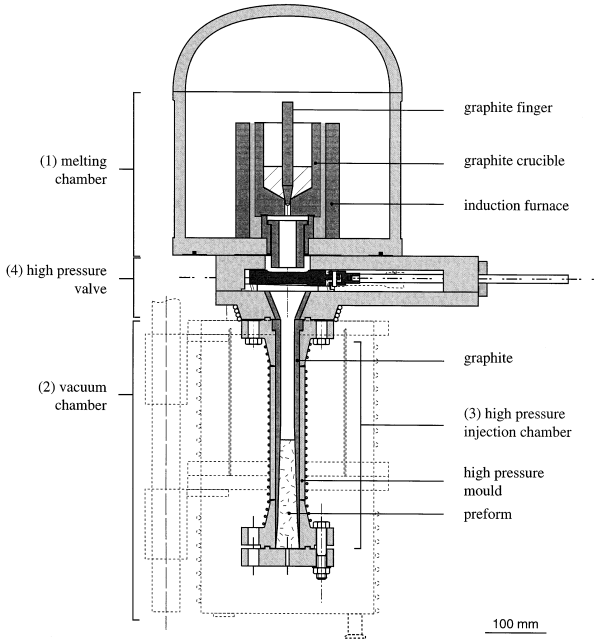

Figure 2.1: Unidirectional low pressure infiltration apparatus.

the hot extruded composites. The volume fraction of reinforcement material was in the range of 5–20%.

In our study, polycrystalline bulk specimens elaborated by Giacometti [Giacometti, 1999] were used as the reinforcement material. They had the nominal composition $Al_{63.5}Cu_{24.0}Fe_{12.5}$ and the icosahedral structure. They were ball-milled to an average particle size of 50 µm using a fast planetary milling machine Retsch PM 4000 with two stainless steel 250 ml containers and 2×12 stainless steel balls with a diameter of 20 mm. The milling speed was 100 RPM and the milling time was 10 minutes. The particles larger than 500 µm were removed by sieving. A spherical shape of particles would be more convenient because angular particles in discontinuous reinforced composites were found to be responsible for a premature crack initiation resulting from a high stress concentration at sharp corners [Christman et al., 1989; Clyne and Withers, 1993].

The resulting powder was infiltrated with a melted aluminium- or magnesium-based alloy using a gas pressure infiltration technique [Carreño-Morelli et al., 1998]. The low pressure unidirectional infiltration device (see Fig. 2.1 and 2.2) consists of four parts: the melting chamber, the vacuum chamber, the injection chamber and the high pressure valve.

The aluminium or magnesium alloy is melted under vacuum or in a controlled atmosphere within a graphite crucible using an induction furnace. The bottom of the

Figure 2.2: Infiltration apparatus with supporting electronic, heating and pressure parts.

crucible is closed by an actuator-controlled graphite finger.

The vacuum chamber provides an isolation of the injection chamber during preform pre-heating, casting and solidification.

The injection chamber is composed of a cylindrical high pressure vessel made of a Ni-Cr-W alloy and of an inner graphite mould in which the preform is located. The preform is rod-shaped with a slightly conical geometry in order to facilitate its extraction through the bottom of the mould. The preform can be pre-heated up to 800°C by means of a wire heater wound around the injection chamber. Five thermocouples installed at different heights within the wall of the injection chamber allow to monitor the temperature evolution during the processing.

The high-pressure valve which separates the injection chamber from the melting chamber is a vacuum gate valve specially reinforced to work up to 5 MPa.

The principle of the operation is shown schematically in Fig. 2.3. In a first step, the melting and injection chambers are evacuated. The alloy is melted in the graphite crucible by means of a high frequency heater (a). Simultaneously, in the injection chamber the preform is pre-heated and degassed. When the desired temperatures of the metal and the preform are reached, the graphite finger is opened, allowing the molten metal

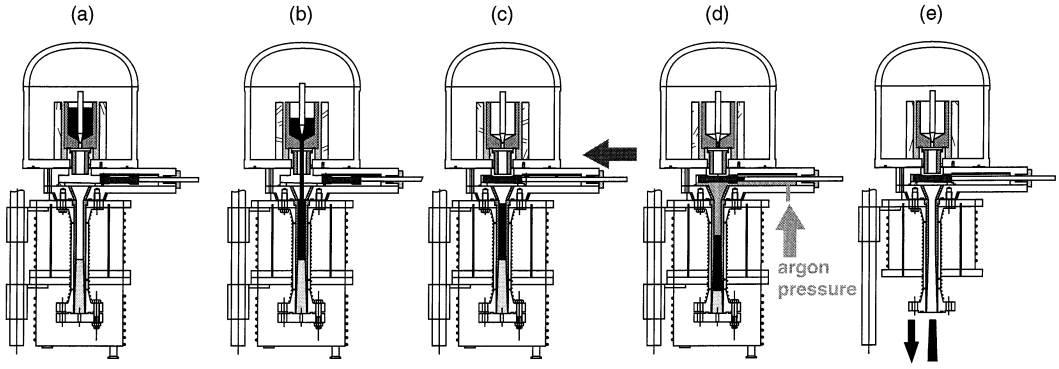

Figure 2.3: Operation of the gas pressure infiltration device: (a) melting, (b) casting, (c) gate valve closing, (d) injection, (e) un-moulding.

to flow from the upper to the lower chamber (b). Then, the gate valve is closed (c) and argon is rapidly introduced until the desired pressure is reached in order to push the metal into the preform (d). Immediately thereafter, the melt cast is cooled down by the activation of a forced air stream. After solidification, the gas pressure is released. When the room temperature is reached, the resulting composite is extracted by opening the bottom parts of both the vacuum and injection chambers (e).

A special attention is paid to the minimisation of the contact time between the molten metal and the reinforcement material in order to reduce inter-phase reactions. From the monitored temperatures an upper limit of 120 s was estimated for the contact time.

2.2 Scanning electron microscopy

The samples have been analysed by scanning electron microscopy (SEM) using a Philips XL 30 FEG microscope (see Fig. 2.4) at the CIME, EPFL. This microscope which can be operated under 1–30 kV is equipped with a field emission gun, a secondary electron detector with a nominal resolution of 2.0 nm at high voltage, an electron backscattering pattern detector (EBSP) and an EDAX Energy Dispersive X-ray Spectrometer (EDS). The energy dispersive X-ray detector can detect all elements with atomic numbers down to carbon.

Figure 2.4: Philips XL 30 FEG scanning electron microscope.

2.3 X-ray diffractometry

The quasicrystalline structure of the samples has been checked by X-ray diffractometry (XRD). The Rigaku, Geigerflex diffractometer (see Fig. 2.5) uses a CuK_α monochromatic radiation with the wavelength of λ=1.542 Å and operates at 40 kV and 30 mA.

A typical X-ray diffraction pattern of icosahedral Al-Cu-Fe quasicrystal is shown in Fig. 2.6. In order to confirm the icosahedral structure of the sample, it is necessary to compare measured and theoretical positions of the diffraction peaks. The positions of the diffraction maxima are given by the Bragg's law

$$n\,\lambda = 2d\sin\Theta, \tag{2.1}$$

where n is the order number, which is equal to one for the strongest "first order" maximum, d is the inter-planar distance and Θ is the semi-diffraction Bragg angle.

The difference between theoretical and measured 2Θ values is always better than 0.1° (see Tab. 2.1), which is the spatial resolution of the used diffractometer.

Figure 2.5: Rigaku X-ray diffractometer.

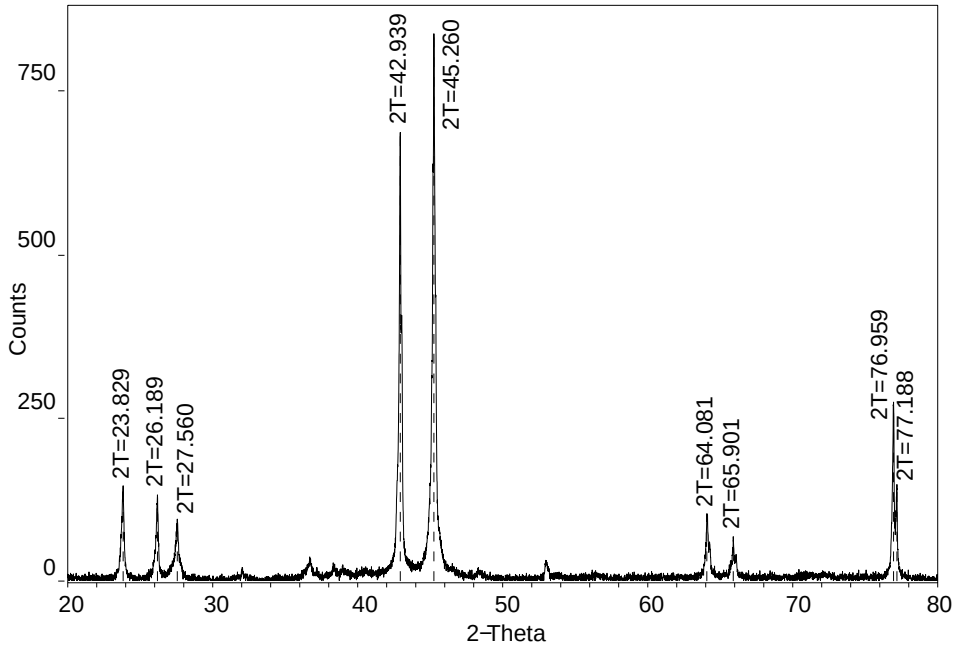

Figure 2.6: X-ray diffractogram of icosahedral Al-Cu-Fe quasicrystal, CuK_α radiation, 0.1°/min scan speed.

Reflection (N,M)	$2\Theta_{theor.}$ [°]	$2\Theta_{meas.}$ [°]	$2\Theta_{theor.} - 2\Theta_{meas.}$ [°]	$2\Theta_{Calvayrac}$ [°]
(6,9)	23.735	23.829	-0.094	-
(7,11)	26.106	26.189	-0.083	26.191
(8,12)	27.475	27.560	-0.085	27.382
(11,16)	31.978	32.0	-0.0	31.904
(14,21)	36.618	36.690	-0.072	36.698
(15,23)	38.261	38.2	0.1	38.322
(18,29)	42.868	42.939	-0.071	42.822
(20,32)	45.193	45.260	-0.067	45.208
(23,36)	48.259	48.2	0.1	-
(27,43)	52.936	52.970	-0.034	-
(31,48)	56.429	56.3	0.1	56.471
(38,61)	64.046	64.081	-0.035	64.053
(40,64)	65.830	65.901	-0.071	65.810
(52,84)	76.882	76.959	-0.077	76.844

Table 2.1: Theoretical (for $d_0 = 17.00$ Å [Calvayrac et al., 1990; Cornier-Quiquandon et al., 1991]) and measured peak positions using XRD CuK$_\alpha$ for Al-Cu-Fe icosahedral quasicrystal. For comparison, the values measured by [Calvayrac et al., 1990] are included.

2.4 Mechanical tests

The deformation tests were performed in compression at constant strain rate using a servo-mechanic computer-controlled machine Schenck RMC 100 and an inverted load-frame (see Fig. 2.7) made of TZM[1]. The sample is isolated inside a quartz tube which enables the compression test to be carried out under vacuum or in a controlled partial atmosphere of argon or helium. A PID controlled image furnace is placed around the quartz tube allowing the choice of temperatures ranging between room temperature and 1300 K with a thermal stability better than ± 0.5 K. Continuous changes in the length of the sample are measured by a couple of inductive extensometers with a resolution of 10^{-4} mm. The applied force is measured by a load cell with a nominal maximum charge of 25 kN.

The machine is controlled and data acquisition is performed using a dedicated computer program. The measured quantities, i.e. the force F and the change in length Δl, are continuously transformed into true stress σ and true strain ε, assuming the incompressibility criterion, as follows

$$\varepsilon = \ln\left(1 + \frac{\Delta l}{l_0}\right), \tag{2.2}$$

$$\sigma = \frac{F}{S_0}\frac{l}{l_0} = \frac{F}{S_0}e^{\varepsilon}, \tag{2.3}$$

where l_0 is the initial length of the specimen, S_0 is its initial cross-section and $l = l_0 + \Delta l$ is the instantaneous length.

The slope of the elastic part of the compression curve (σ, ε) gives the apparent Young's modulus E_{app}, which is lower than the real Young's modulus of the sample E. It can be corrected supposing that a small part of the machine (see Fig. 2.7) with a pseudo Young's modulus[2] E_m is serially deformed with the sample. Then

$$\frac{1}{E_{app}} = \frac{1}{E_m} + \frac{1}{E}, \tag{2.4}$$

where $E_m = 82$ GPa for the Schenck machine and for the common sample size $4 \times 4 \times 9$ mm.

[1] heat resistant Ti-Zr-Mo alloy
[2] depending on the sample size

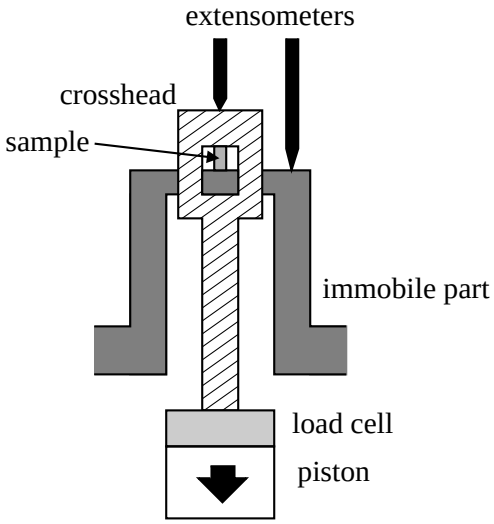

Figure 2.7: Schematic of the compression deformation machine.

2.5 Mechanical spectroscopy

2.5.1 Forced torsion pendulum

The inverted forced torsion pendulum (see Figs. 2.8 and 2.9) uses the sub-resonant method. The specimen is submitted to a forced vibration with an angular frequency ω which is much lower than the angular resonance frequency ω_r of the system pendulum-sample. The plate shape specimen with dimensions $4 \times 1 \times 50$ mm is firmly fixed at both extremities. The upper grip is attached to a connecting rod which also transmits the torsion. The rod is suspended using a tungsten wire which is given a suitable tension by a counterweight. The excitation is done by means of a magneto-electric system of two coils and permanent magnets connected to the rod, and the deformation is measured by an optical system and a linear photo-cell. A resistivity furnace with a Eurotherm PID controller permits to change the temperature of the sample in the range of 70–800 K. A partial pressure of 5 mbar of He or vacuum were used. The whole installation lies on an anti-vibration table.

The electrical excitation signal for the magnetic coils is provided by a signal generator with a sinusoidal shape of a given frequency and amplitude. The phase lag between the excitation signal and the response signal, as well as the amplitude of the response signal, are measured using an analyser. Both the analyser and the generator are parts of a Solartron-Schlumberger frequency response analyser 1250.

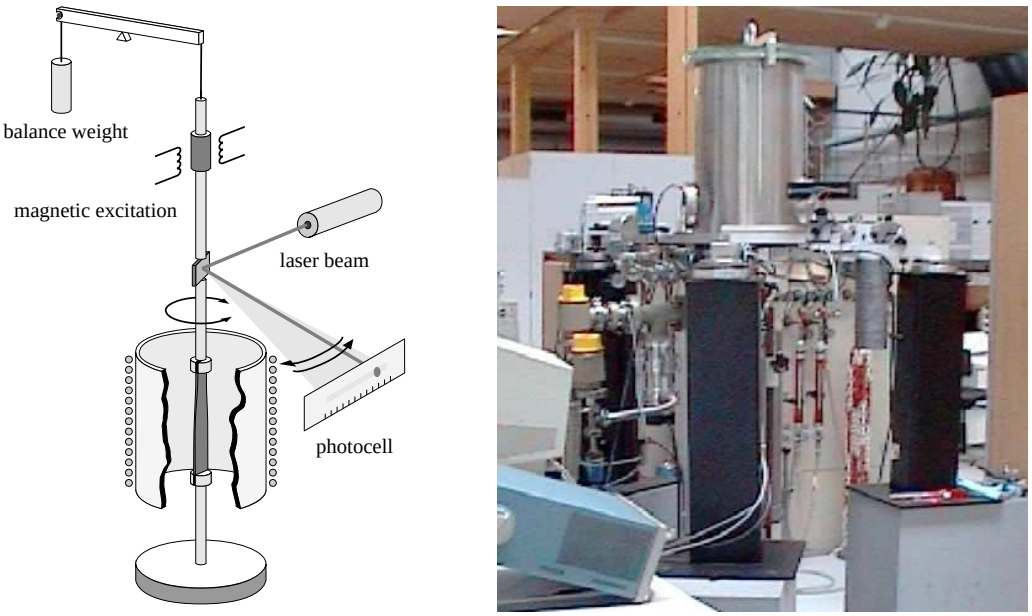

(a) schematic (b) Guzla

Figure 2.8: Inverted forced torsion pendulum.

Figure 2.9: Electronic part of the Guzla forced pendulum.

The equation of motion for small mechanical losses is

$$I\ddot{\Theta} + \frac{C}{l}\left(1 + i\tan\delta\right)\Theta = M_{ext}, \tag{2.5}$$

where I is the moment of inertia of the pendulum, Θ is the torsion angle, C is the torsional rigidity of the sample described in next chapter, $\tan\delta$ is the mechanical loss of the sample, M_{ext} is the applied periodical external excitation torque and l is the sample length.

In the case without external excitation $M_{ext} = 0$ the pendulum behaves like a free pendulum and it oscillates with the angular resonance frequency ω_r

$$\omega_r^2 = \frac{C}{l\,I}. \tag{2.6}$$

The moment of inertia I is given by a volume integration of the rotating parts

$$I = \iiint \rho\, r^2\, dV, \tag{2.7}$$

where r is the distance from the rotation axis and ρ is the density. The moment of inertia of a pendulum can be easily determined by measuring the angular resonance frequency ω_r and the changed angular resonance frequency ω_r' when the moment of inertia is increased to I' by adding two small masses m at a distance r from the axis, then

$$I' = I + 2mr^2. \tag{2.8}$$

Consequently, the initial moment of inertia I can be calculated as

$$I = 2mr^2\,\frac{\omega_r^2 - \omega_r'^2}{\omega_r'^2}. \tag{2.9}$$

The torsional rigidity C gives the restoring moment M when a specimen is deformed in torsion with a torsion angle Θ (see Fig. 2.10)

$$M = \frac{C\Theta}{l}. \tag{2.10}$$

Hence, the stored elastic energy W is

$$W = \frac{1}{2}C\frac{\Theta^2}{l}. \tag{2.11}$$

The exact form of the torsional rigidity C depends on the specimen geometry and for a thin rectilinear bar with an arbitrary cross-section, it is given by [Landau and Lifchitz, 1967]

$$C = 4G\iint \chi\, dS, \tag{2.12}$$

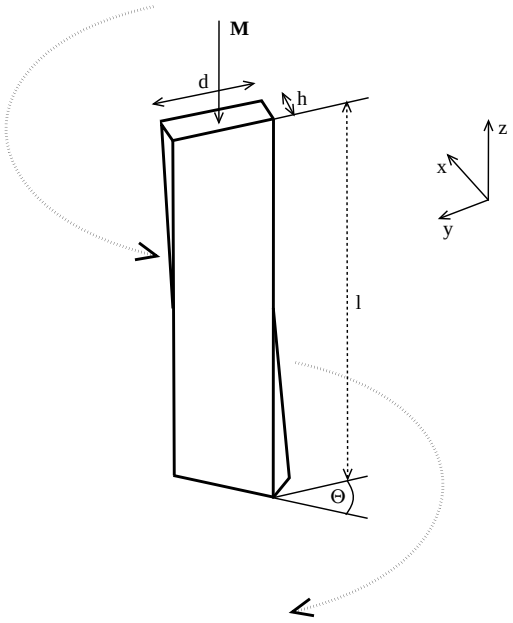

Figure 2.10: Torsion of a rectangular bar.

where we integrate over the cross-section and χ is the torsional function vanishing at the surface of the bar and satisfying the two dimensional Laplace equation

$$\nabla^2 \chi = -1. \tag{2.13}$$

The solution for a circular bar is

$$C_{circular} = \frac{\pi G r^4}{2}, \tag{2.14}$$

$$\chi_{circular} = \frac{1}{4}\left(r^2 - x^2 - y^2\right), \tag{2.15}$$

where r is the radius of the bar. The torsional rigidity of a rectangular bar is more complicated

$$C_{rectangular} = \beta G d h^3, \tag{2.16}$$

where $d \geq h$ are the dimensions of the cross-section of the bar and β is a numerical coefficient depending on d/h. The maximal tangential shear stress during a torsional deformation is reached in the middle of the longer side d and it is

$$\tau_{max} = \frac{M}{\alpha d h^2}, \tag{2.17}$$

where α is a second numerical coefficient also depending on d/h. Then the formula for maximal shear deformation is

$$\gamma_{max} = \frac{\Theta}{l}\frac{\beta}{\alpha}h, \tag{2.18}$$

Ratio d/h	α	β
1.00	0. 217 566 55	0. 140 577 01
1.50	0. 231 723 94	0. 195 760 71
1.75	0. 239 190 43	0. 214 260 89
2.00	0. 245 947 53	0. 228 681 68
2.50	0. 257 596 54	0. 249 365 07
3.00	0. 267 208 68	0. 263 316 93
4.00	0. 281 665 67	0. 280 812 96
6.00	0. 298 358 54	0. 298 319 51
8.00	0. 307 074 70	0. 307 072 96
10.00	0. 312 325 11	0. 312 325 04
∞	1/3	1/3

Table 2.2: Numerical coefficients α and β for torsion of a rectangular bar.

which is the formula used for shear deformation in the forced and free pendulums. The numerical coefficients α and β can be calculated using infinite series [Rékatch, 1980]

$$\beta = \frac{1}{3} - \frac{64}{\pi^5}\frac{h}{d}\sum_{k=0}^{\infty}\frac{\tanh\frac{\pi d(2k+1)}{2h}}{(2k+1)^5}, \tag{2.19}$$

$$\frac{\beta}{\alpha} = 1 - \frac{8}{\pi^2}\sum_{k=0}^{\infty}\frac{1}{(2k+1)^2\sinh\frac{\pi d(2k+1)}{2h}}. \tag{2.20}$$

For some ratios d/h the values α and β are listed in Tab. 2.2 and plotted in Fig. 2.11.

The external excitation M_{ext} and the response torsion angle Θ can be written in the following complex exponential forms

$$M_{ext} = M_0\, e^{i\omega t}, \tag{2.21}$$

$$\Theta = \Theta_0\, e^{i(\omega t-\phi)}, \tag{2.22}$$

where ω is the angular frequency of excitation, ϕ is the measured phase lag between the excitation and response signals, M_0 and Θ_0 are their amplitudes. Then the equation (2.5) becomes

$$-\omega^2\Theta_0 + \omega_r^2\,(1 + i\tan\delta)\,\Theta_0 = \frac{M_0}{I}e^{i\phi} \tag{2.23}$$

and the measured phase lag ϕ is related to the specimen damping $\tan\delta$ by

$$\tan\phi = \frac{\omega_r^2}{\omega_r^2-\omega^2}\tan\delta. \tag{2.24}$$

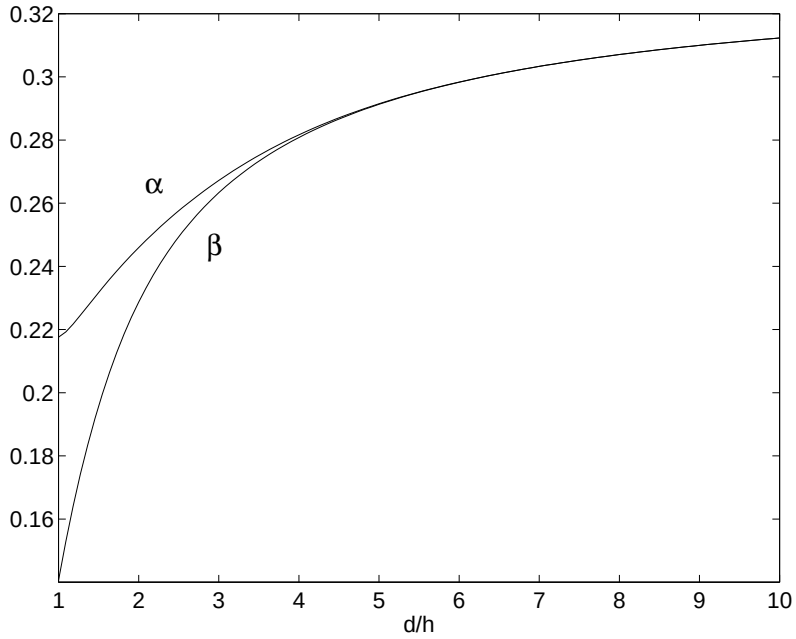

Figure 2.11: Numerical coefficients α and β for torsion of a rectangular bar.

This equation is used to subtract the so-called "resonance background" from the internal friction spectra obtained in the forced pendulum. The advantage of the sub-resonant method is that for angular excitation frequencies much smaller than the angular resonance frequency $\omega \ll \omega_r$ the measured phase lag corresponds directly to the specimen damping $\tan\delta \simeq \tan\phi$.

It has been observed by Carreño-Morelli and Schaller [Schaller, 2001] that the measured phase-lag in the isothermal condition increases linearly with the frequency. This effect does not depend on the specimen and is probably caused by the electronic part of the pendulum. It is also much more important in the interesting frequency range of 0–10 Hz than the correction (2.24) due to the resonance-background (see Fig. 2.12). The slope is $d\left(Q^{-1}\right)/df = (0.70 \pm 0.05) \times 10^{-3}\,\mathrm{Hz}^{-1}$ and it is independent of the sample.

Next, the measured phase-lag is corrected by subtracting the linear dependency and a constant forced pendulum background $Q^{-1}_{back} = 0.8 \times 10^{-3}$ which was determined by comparing the internal friction spectra with the ones obtained for an identical specimen using a free pendulum

$$Q^{-1}_{corrected} = Q^{-1}_{measured} - \frac{d\left(Q^{-1}\right)}{df} f - Q^{-1}_{back}. \tag{2.25}$$

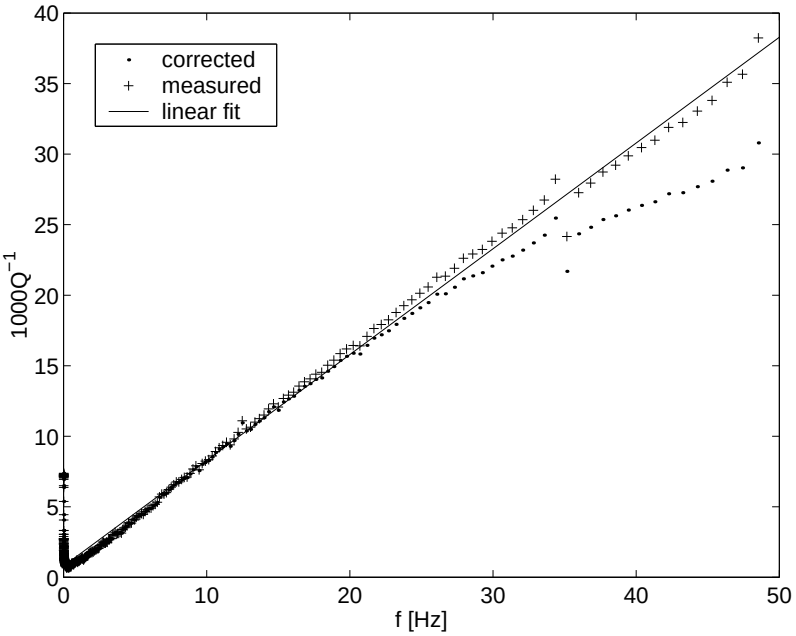

Figure 2.12: Isothermal 300 K spectrum of mild steel as measured in the forced pendulum Guzla, the resonance-background corrected spectrum (resonance frequency 110 Hz) and the linear fit.

The relation between the amplitudes M_0 and Θ_0 can be derived from the equation (2.23)

$$\Theta_0^2 = \left(\frac{M_0}{I}\right)^2 \frac{1}{\left(\omega_r^2 - \omega^2\right)^2 + \omega^4 \tan^2 \delta}. \tag{2.26}$$

For small mechanical losses $\tan \delta \ll 1$ the amplitude of deformation Θ_0 is maximal for the angular resonance frequency $\omega = \omega_r$ and is equal to

$$\Theta_0^{max} = \frac{M_0}{I \tan \delta \omega_r^2}. \tag{2.27}$$

The quality factor Q of an oscillator is usually given by

$$Q = \frac{\omega_r}{\Delta\omega}, \tag{2.28}$$

where $\Delta\omega$ is the width of the resonance peak in frequency at the height $\Theta_0^{max}/\sqrt{2}$ (see Fig. 2.13). From equation (2.26) $\Delta\omega$ equals to

$$\Delta\omega = \omega_r \left(\sqrt{1 + \tan \delta} - \sqrt{1 - \tan \delta} \right). \tag{2.29}$$

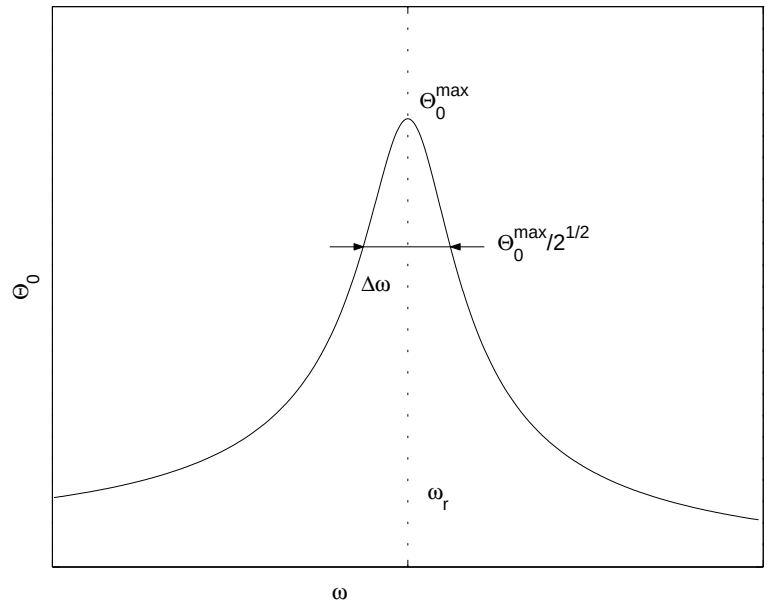

Figure 2.13: Amplitude of torsional deformation Θ_0 as a function of angular frequency ω near the resonance ω_r.

For small mechanical losses $\tan\delta \ll 1$ it becomes

$$\Delta\omega = \omega_r \tan\delta. \tag{2.30}$$

Then the internal friction Q^{-1} is equal to the mechanical loss

$$Q^{-1} = \frac{\Delta\omega}{\omega_r} = \tan\delta. \tag{2.31}$$

2.5.2 Free torsion pendulum

The inverted free torsion pendulum uses the resonant method. The apparatus is similar to the forced torsion pendulum, the only difference is that there is no permanent excitation. The oscillations are achieved by means of several pulses to get the desired amplitude, then the pendulum is left free and the free decay of a chosen number of periods is recorded.

The equation of motion for the free pendulum for small mechanical losses is similar to the equation for the forced pendulum (2.5)

$$I\ddot{\Theta} + \frac{C}{l}\left(1 + i\tan\delta\right)\Theta = 0, \tag{2.32}$$

where I is the moment of inertia of the pendulum, Θ is the torsion angle, C is the torsional rigidity of the sample, $\tan\delta$ is the mechanical loss of the sample and l is the sample length.

The pendulum oscillates with the resonance frequency ω_r given by the equation (2.6). This equation is used to determine the torsional rigidity C (see equations (2.14) and (2.16)) and further the shear modulus G of the sample

$$G_{circular} = \frac{2I\,l\,\omega_r^2}{\pi\,r^4}, \tag{2.33}$$

$$G_{rectangular} = \frac{I\,l\,\omega_r^2}{\beta\,a\,b^3}. \tag{2.34}$$

The solution of the equation of motion (2.32) is

$$\Theta = \Theta_0 e^{i\omega_r t} e^{-\frac{1}{2}\omega_r t\,\tan\delta}. \tag{2.35}$$

Then the internal friction is calculated as

$$Q^{-1} = \frac{1}{n\pi}\ln\frac{\Theta_i}{\Theta_{i+n}}, \tag{2.36}$$

where Θ_i and Θ_{i+n} are the amplitudes of oscillation of the i-th and $(i+n)$-th periods.

The accuracy of the internal friction measurement can be greatly increased by using a discrete Fourier transformation of the waveform of damped oscillations. The disturbing components of the parasitic motion, such as the flexural or processional ones, are separated[3] from the genuine torsional motion and eliminated by calculating the decay constant [Yoshida et al., 1981].

The discrete Fourier transform (DFT) of the deformation $\Theta(t)$ given by the equation (2.35) over the finite time interval Δt is

$$F(s) = \sum_{r=0}^{2n-1} \Theta(t_r)\, e^{-\frac{2\pi i r s}{2^n}}, \tag{2.37}$$

where $t_r = 2^{-n}\Delta t\, r$, r and $s = 0, 1, 2, 3, \ldots, 2^n - 1$. Around the main peak $s_p = \omega_r \Delta t/2\pi$ the function $F(s)$ becomes

$$F(s) = 2^{n-2}\,\frac{A\,i}{\pi}\,\frac{1 - e^{2\pi i s_p}}{s_p - s} + B + Cs + D(s), \tag{2.38}$$

where A is equal to the deformation amplitude Θ_0, B and C represent the influences of other parasitic frequencies which are fairly distant from ω_r and D represents the influence of random noise. $D(s)$ is in most cases negligible. Using four values of $F(s)$

[3] supposing that the parasitic frequencies are different from the torsional resonance frequency

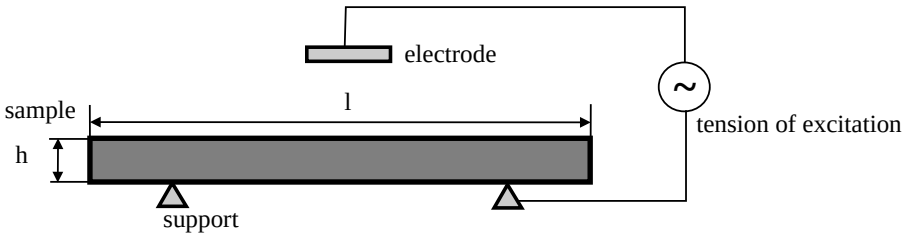

Figure 2.14: Free-free vibrating bar apparatus.

around the peak s_p the unknown parameters can be determined, which gives the internal friction

$$Q^{-1} = 2\frac{-\Im\left(\frac{3}{R-1}\right)}{\Re\left(s_1 - \frac{3}{R-1}\right)}, \tag{2.39}$$

where

$$R = \frac{F(s_1) - 2F(s_2) + F(s_3)}{F(s_2) - 2F(s_3) + F(s_4)} \tag{2.40}$$

and $s_2 = s_1 + 1$, $s_3 = s_2 + 1$, $s_4 = s_3 + 1$ and $s_2 \leq s_p < s_3$.

2.5.3 Free-free vibrating bar apparatus

The free-free vibrating bar apparatus (see Figs. 2.14–2.16) uses the resonant method in flexion. The "free-free" term refers to the two free ends of the sample whose usual dimensions are $1\times4\times40$ mm. The sample is excited by means of an electro-static force created by an oscillating high tension between the electrode and the sample. The frequency is kept close to the resonance frequency of the sample by the electronic part. When the excitation is stopped, the free decay is registered by measuring the capacity between the sample and the electrode. Then the internal friction of the sample is directly given by the free decay equation similar to the equation (2.36)

$$Q^{-1} = \frac{1}{n\pi} \ln \frac{A_i}{A_{i+n}}, \tag{2.41}$$

where A_i and A_{i+n} are the chosen amplitude thresholds, n is the number of periods needed to decrease the amplitude from A_i to A_{i+n}. The Young's modulus can be calculated from the resonance frequency of vibration f of the sample [Vittoz et al., 1963]

$$E = \frac{3\pi^2 f^2 \rho l^4}{h^2 x^4}, \tag{2.42}$$

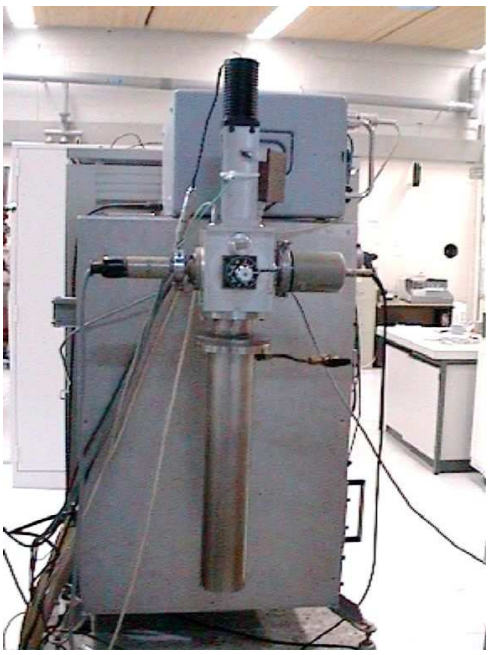

Figure 2.15: Free-free vibrating bar apparatus Xylophone II.

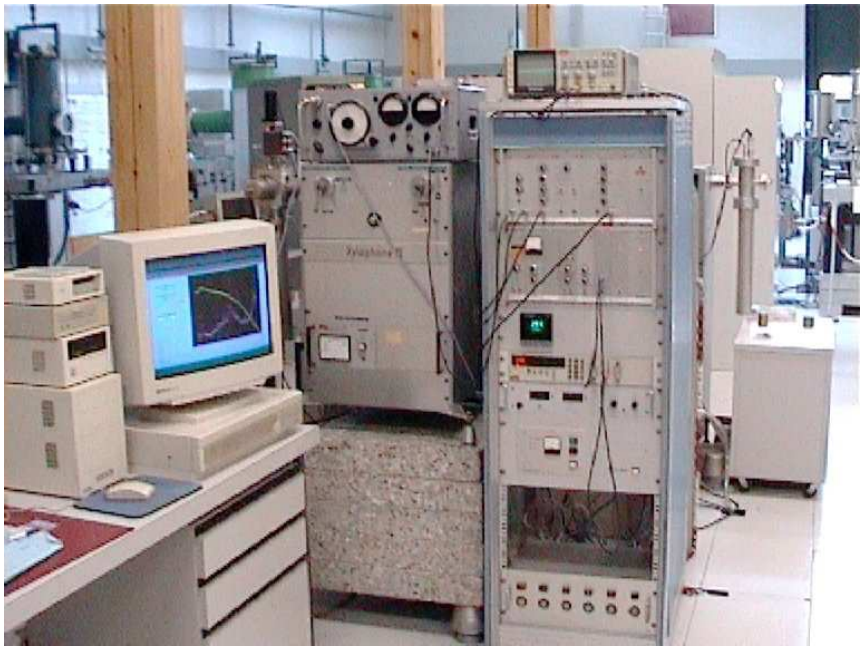

Figure 2.16: Electronic part of the Xylophone II vibrating bar apparatus.

Mode number i	Eigenvalue x_i
1	2. 365 020 37
2	4. 712 388 98
3	5. 497 803 92
4	7. 853 981 63
5	8. 639 379 83

Table 2.3: Eigenvalues for the free-free boundary problem.

where l and h are the sample dimensions, ρ is the sample density and x is the solution of the free-free boundary problem

$$\tan x + \tanh x = 0. \tag{2.43}$$

For the basic mode $x_1 = 2.36502037$, some of the eigenvalues for higher modes are given in Tab. 2.3. Usually only the basic mode is supposed to be excited.

Chapitre 3

Experimental results - Coatings

At first the mechanical properties of the mild steel substrate are presented, next the structure and the mechanical properties of the quasicrystalline coating are studied and finally, the mechanical spectroscopy measurements are presented.

3.1 Substrate

The internal friction and the Young's modulus of the mild steel substrate were measured in the free-free vibrating bar apparatus using a frequency of 3.3 kHz. The mechanical loss spectrum (see Fig. 3.1) consists of an exponential background and of a relaxation peak which is more easily seen when the background is subtracted. The temperature range of the peak corresponds to the carbon Snoek peak in α-iron [Weller, 1996].

From the carbon peak height, i.e. the relaxation strength, the concentration of interstitial carbon atoms in solution can be calculated. The carbon concentrations are 3.2 ppm and 0.7 ppm for heating and cooling stages, respectively. The difference in the carbon concentrations means probably that a certain amount of the carbon interstitials precipitate at high temperature.

The corresponding Young's modulus as a function of temperature can be seen in Fig. 3.2. The Young's modulus at 300 K is $E = (205 \pm 4)$ GPa, which is in the range of usual values for steel, i.e. (200–220) GPa. The decrease of the Young's modulus with increasing temperature can be approximated linearly with a relative slope of $3.4 \times 10^{-4}\,\mathrm{K}^{-1}$.

Next, the mild steel substrate samples of dimensions $4 \times 4 \times 7$ mm were deformed at constant strain rate in a compression machine. The resulting stress-strain compression curves are reported in Fig. 3.3. The yield stress was found to depend strongly on the temperature, as for instance $\sigma_y = 415$ MPa at 300 K and $\sigma_y = 225$ MPa at 700 K.

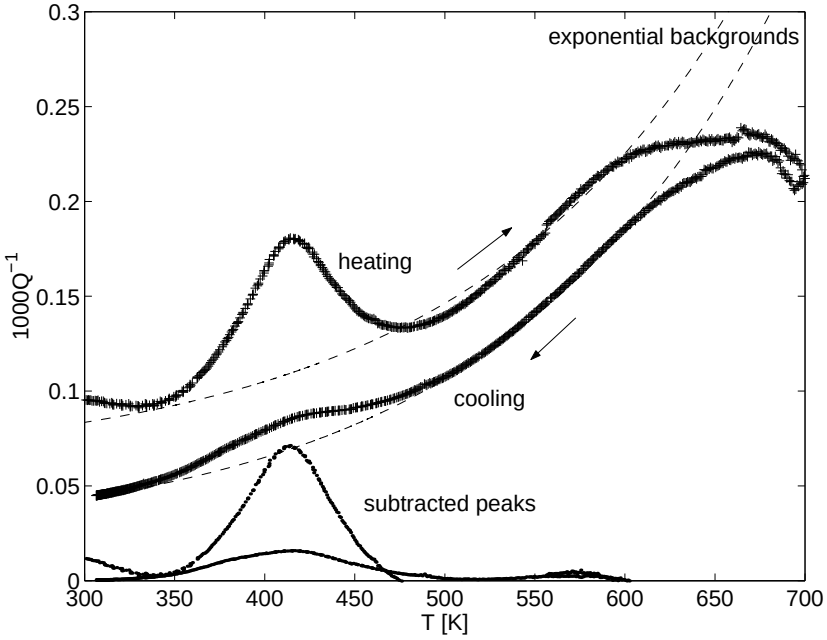

Figure 3.1: Internal friction spectra of the mild steel substrate as measured in the free-free vibrating bar apparatus using a frequency of 3.3 kHz. The curves with subtracted exponential background show the carbon Snoek peaks corresponding to carbon concentrations of 3.2 ppm and 0.7 ppm.

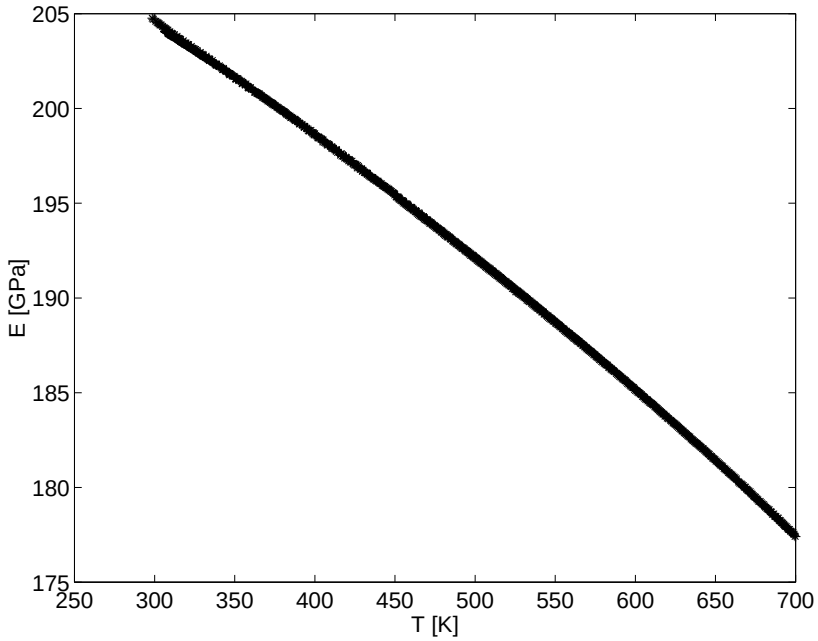

Figure 3.2: Young's modulus E of the mild steel substrate as measured in the free-free vibrating bar apparatus.

The slope of the elastic part of the compression curves gives an apparent Young's modulus of $E_{app} = 57\,\text{GPa}$. Using the equation (2.4) it gives the corrected value $E = 186\,\text{GPa}$, which is close to the value of 205 GPa measured in the free-free vibrating bar apparatus.

Finally, the shear modulus G of the mild steel substrate was measured in the free torsional pendulum. The shear modulus was found to be $G = (70 \pm 1)\,\text{GPa}$ at 300 K (see Fig. 3.4), which is slightly lower than the usual value for mild steel of (78–86) GPa. The decrease of the shear modulus with increasing temperature can be approximated linearly with a relative slope of $2.8 \times 10^{-4}\,\text{K}^{-1}$, which is close to the decrease of the Young's modulus of $3.4 \times 10^{-4}\,\text{K}^{-1}$.

The mechanical properties of the steel substrate are summarised in Tab. 3.1. The values of thermal expansion α and Poisson's ration ν are the usual values for mild steel.

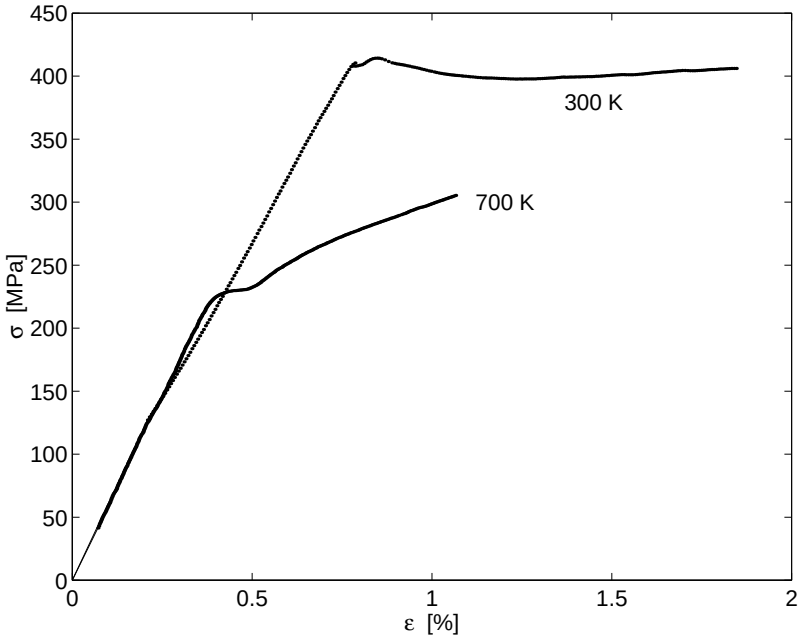

Figure 3.3: True stress-strain compression curves of the mild steel substrate showing a yield point at 415 MPa and 225 MPa for temperatures of 300 K and 700 K, respectively.

Parameter	Value	Unit
E	205	GPa
$(dE/dT)/E$	-3.4×10^{-4}	K^{-1}
G	69.8	GPa
$(dG/dT)/G$	-2.8×10^{-4}	K^{-1}
α	11.8×10^{-6}	K^{-1}
ν	0.29	1

Table 3.1: Summary of the mechanical parameters values for the steel substrate.

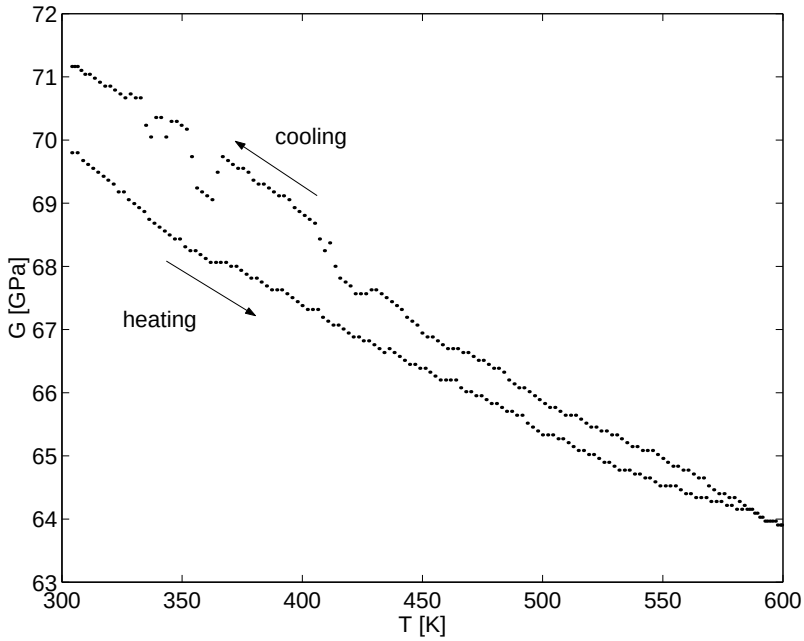

Figure 3.4: Shear modulus G of the mild steel substrate as measured in the forced torsion pendulum. The curve was calibrated using the shear modulus value $G = 69.8\,\text{GPa}$ measured at 300 K value in the free torsional pendulum.

3.2 Coating

3.2.1 Structure

Optical and scanning electron micrographs (see Figs. 3.5, 3.6, and 3.7) reveal the heterogeneous structure of the quasicrystalline coating that contains a large density of cracks and pores (black). The thickness of the coating is irregular due to the damage of the brittle layer resulting from the preparation of the cross-sectional specimen. Pores having a typical size of 1 µm and an irregular shape are detailed in Fig. 3.7. A second population of smaller, sub-micron pores is also visible. The pores sometimes exhibit sharp edges that are able to concentrate stresses and become thus ideal crack nucleation sites.

As the composition of the coating $Al_{50.5}Cu_{22.0}Fe_{12.5}Cr_{14.5}B_{0.5}$ is close to the one of the decagonal $Al_{64}Cu_{18}Fe_8Cr_8$ alloy [Dubois et al., 1991], the presence of the decagonal phase can be expected. This was confirmed by performing X-ray diffractometry (see Fig. 3.8 and Tab. 3.2). The other peaks correspond to other phases in low concentrations. Indeed, a fine net of bright islands and bridges of a second phase in the uniformly grey matrix of the decagonal phase can be seen in Fig. 3.7.

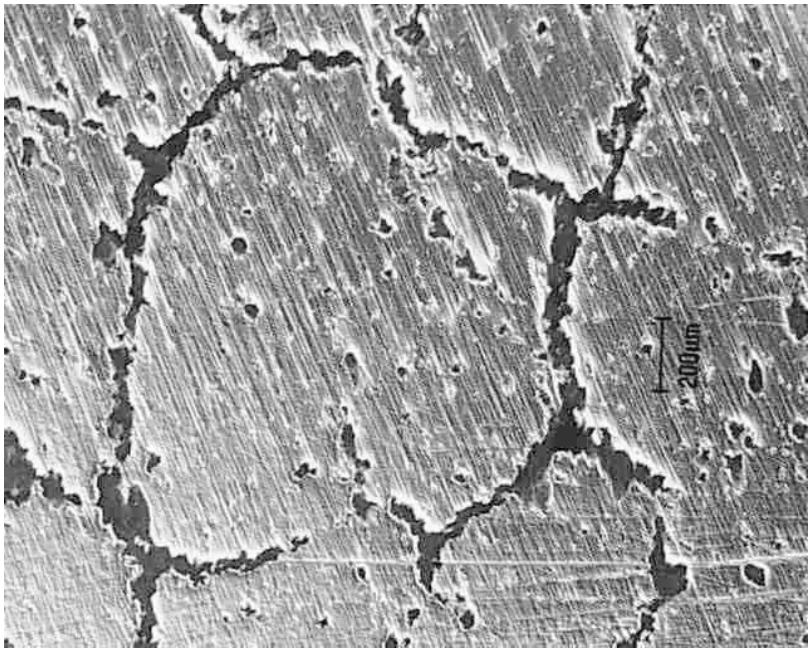

Figure 3.5: Optical micrograph of a thermal sprayed Al-Cu-Fe-Cr coating showing a network of cracks in black.

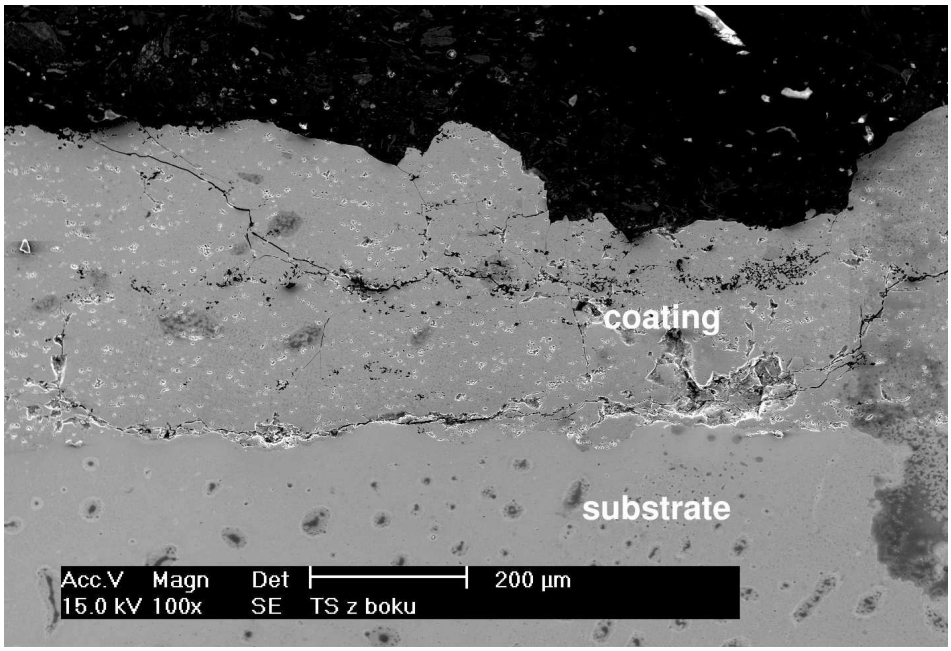

Figure 3.6: Cross-sectional SEM of a thermal sprayed Al-Cu-Fe-Cr coating on a steel substrate showing a high density of cracks and pores (black) inside the coating.

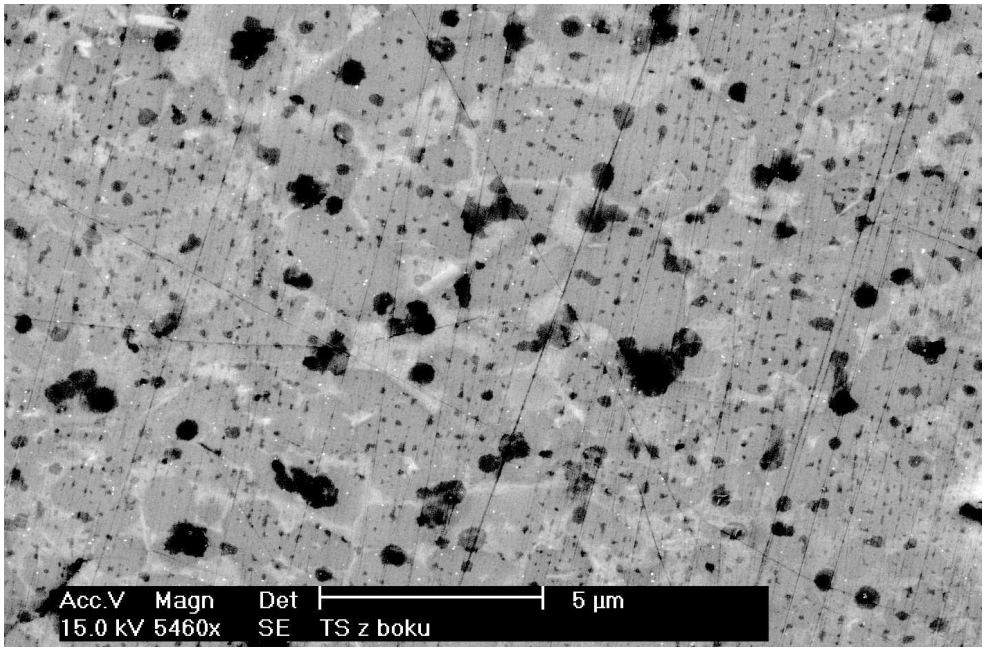

Figure 3.7: SEM detail of the Al-Cu-Fe-Cr coating.

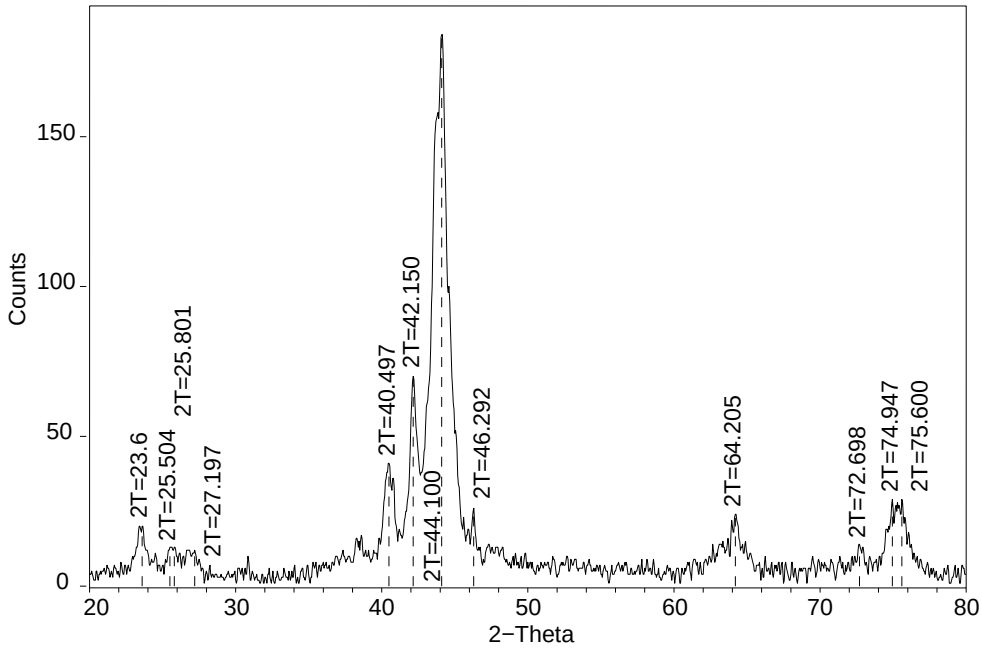

Figure 3.8: XRD of the Al-Cu-Fe-Cr coating, CuK_α radiation, 0.5°/min scan speed.

Index	$2\Theta_{theor.}$ [°]	$2\Theta_{meas.}$ [°]	$2\Theta_{theor.} - 2\Theta_{meas.}$ [°]
01103	25.947	25.801	0.146
12212	27.212	27.197	0.015
13312	40.454	40.497	-0.043
00006	44.109	44.100	0.009
14523	64.235	64.205	0.030
25525	74.911	74.947	-0.036
15630	75.617	75.600	0.017

Table 3.2: Theoretical [Dong and Dubois, 1991] and measured peak positions for the Al-Cu-Fe-Cr decagonal quasicrystal with calculated quasilattice constants $a = 4.532$ Å and $c = 12.320$ Å, XRD CuK$_\alpha$.

Transmission electron microscopy (TEM) observations were performed on a Philips CM 20 microscope operating at 200 kV, which corresponds to a wave length of electrons of 0.0251 Å. The typical TEM micrograph in Fig. 3.9 shows a complex "tweed-like" image contrast similar to the one usually observed for icosahedral Al-Cu-Fe [Giacometti, 1999]. The origin of this contrast is not clear. Unfortunately, it can mask an eventual presence of dislocations. Moreover, even individual grains are not easily distinguishable. The diffraction pattern in Fig. 3.10, which was taken with a large selection aperture, is composed of diffraction rings. This is an indication of the small size of the individual grains (about 200 nm). The presence of a quasicrystalline phase is clearly confirmed by the diffraction pattern in Fig. 3.11 showing five or ten-fold symmetry. The distances R of the diffraction spots from the transmitted beam, as measured from diffraction patterns, correspond well to the decagonal structure with a quasiperiodic lattice parameter $a = 4.00$ Å(see Tab. 3.3). The diffraction equation for the transmission electron microscope has the form

$$\lambda L = d R, \tag{3.1}$$

where λ is the electron wavelength, L is the camera length and d is the inter-planar distance. The inter-planar distances calculated theoretically and those determined experimentally from the diffraction pattern in Fig. 3.11 are compared in Tab. 3.3. The difference in the lattice parameter values measured by XRD (see Tab. 3.2) and TEM may be caused by the fact that XRD shows the average structure and TEM the local one, important are also the uncertainties on the camera length L and the measured distances R.

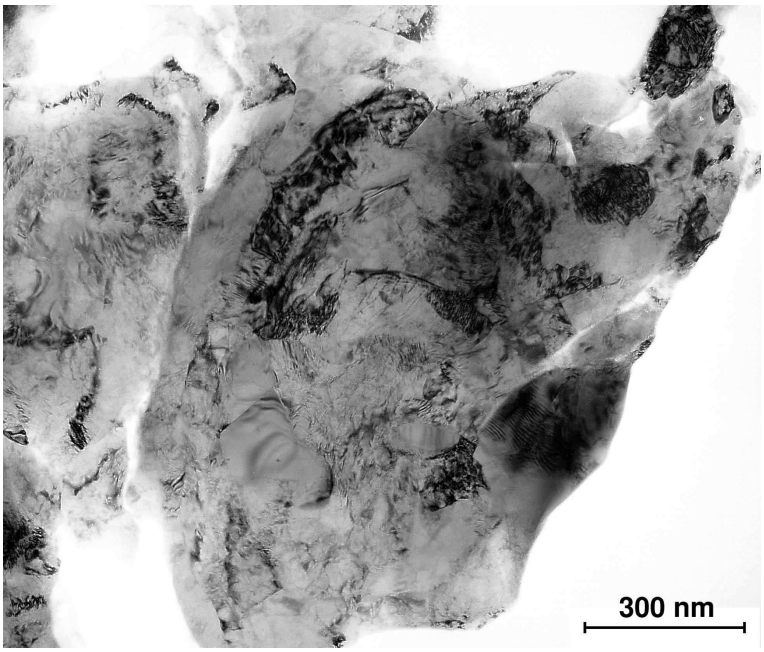

Figure 3.9: TEM of the Al-Cu-Fe-Cr coating showing a complex image contrast and small grains.

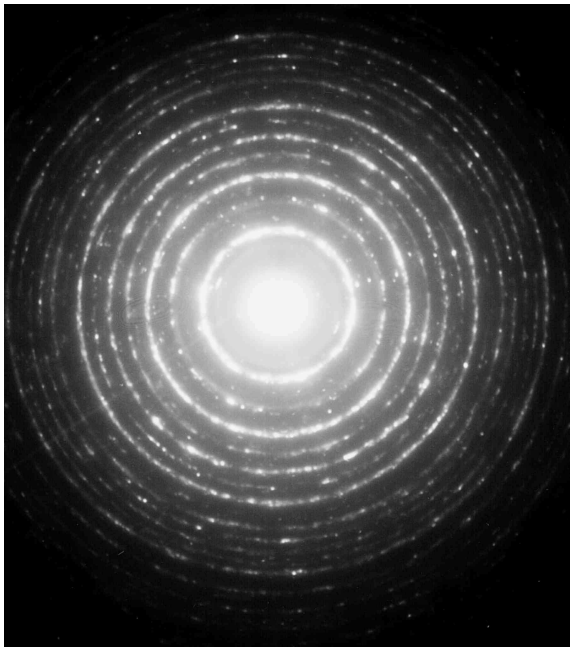

Figure 3.10: TEM diffraction rings caused by small grains of the Al-Cu-Fe coating, 200 kV, camera length 0.653 m, large selection aperture (diffraction from many grains).

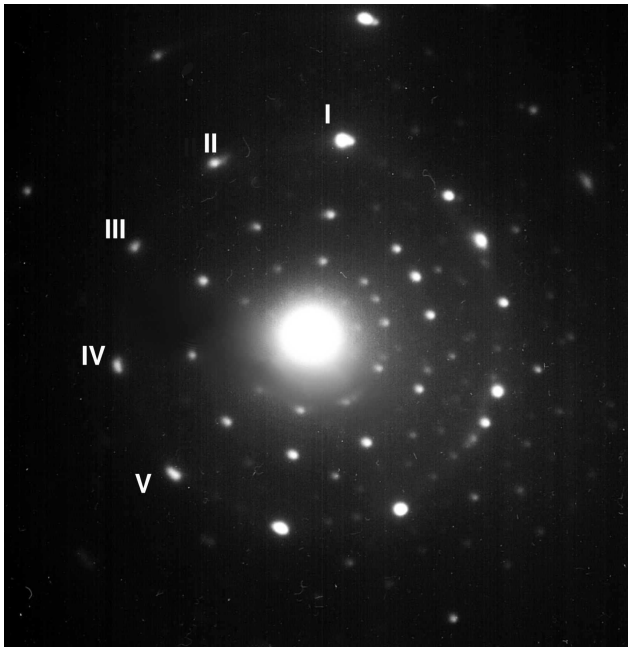

Figure 3.11: TEM diffraction pattern of the Al-Cu-Fe coating showing five or ten-fold symmetry, 200 kV, camera length 1.92 m, small selection aperture (diffraction from a few grains, one of them dominating).

Index	R [mm]	$d_{theor.}$ [Å]	$d_{meas.}$ [Å]
11110	5.35	8.875	9.007
01100	8.80	5.485	5.476
12210	14.21	3.390	3.391
13310	22.90	2.095	2.104
25520	37.88	1.295	1.272

Table 3.3: Distances R of TEM diffraction spots from the transmitted beam and comparison of theoretical inter-planar distances with experimental ones in Fig. 3.11 (calculated with the quasilattice constant $a = 4.00$ Å).

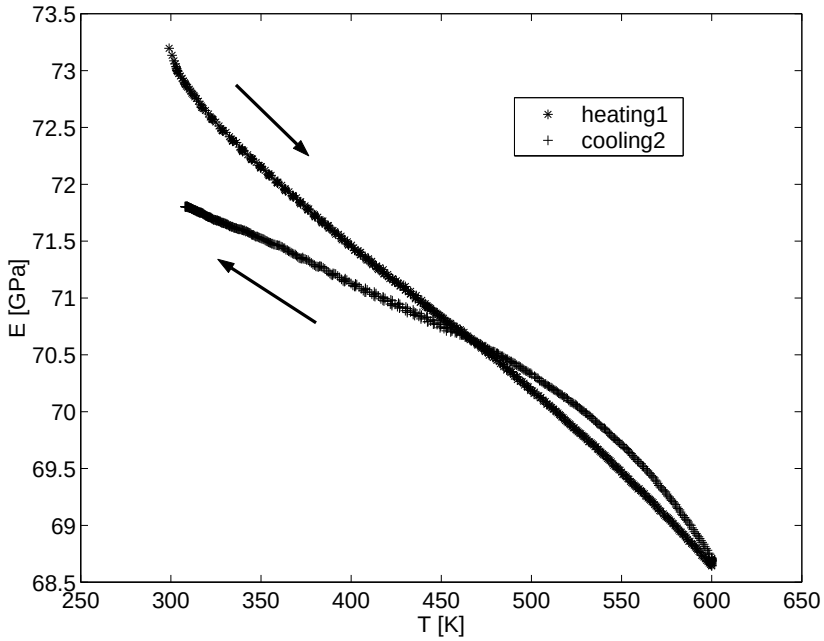

Figure 3.12: Young's modulus E of the composite as measured in the free-free vibrating bar apparatus.

Since there are almost no reports on the mechanical and thermodynamical properties of decagonal Al-Cu-Fe-Cr, we have used the values for icosahedral Al-Cu-Fe, supposing they are similar because the composition and the structure of both phases are also similar.

3.2.2 Mechanical properties

The Young's modulus of the composite was measured in the free-free vibrating bar apparatus (see Fig. 3.12). It is not possible to measure the coating alone. Nevertheless, from the values of modulus of the composite E_c and the substrate E_2, the value of the coating modulus E_1 can be calculated using the formula (5.28) which is developed in section 5.2.

In our particular case, as $h_1 = 454\,\mu m$, $h_2 = 593\,\mu m$, $E_c = (73 \pm 1)\,GPa$, $E_2 = 205\,GPa$ the Young's modulus[1] of the quasicrystalline coating is $E_1 = 28\,GPa$. This value is quite low compared with the one of icosahedral Al-Cu-Fe of 250 GPa

[1] substantial decrease of modulus during successive measurements was observed probably due to coating or interface damage

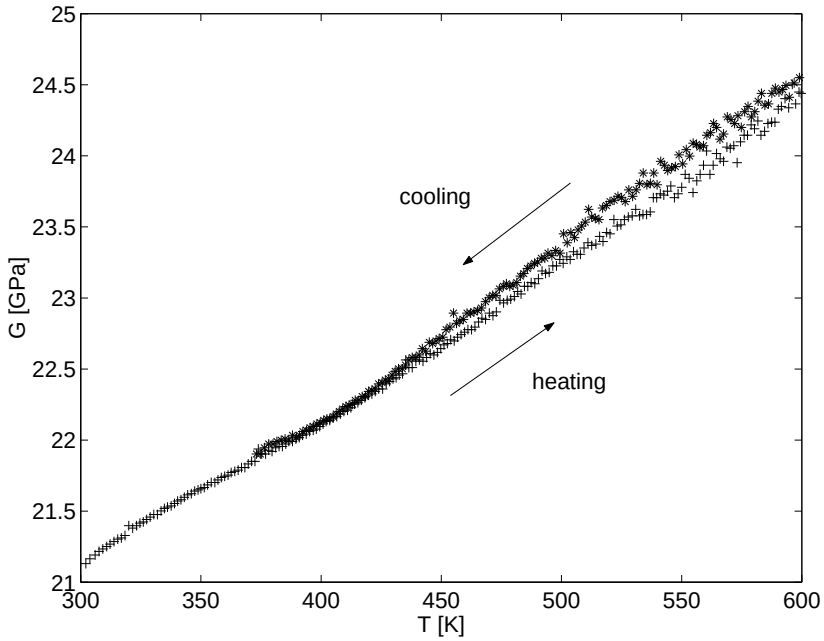

Figure 3.13: Shear modulus G anomaly of the composite as measured in the free torsion pendulum.

[Giacometti, 1999] and can be explained by the presence of cracks, pores and by the irregular thickness of the coating.

The relative decrease of the Young's modulus with increasing temperature 0.2×10^{-4} K^{-1} is much smaller than in the case of the substrate. This is probably due to the fact that some cracks are closing with increasing temperature.

Next, the shear modulus G_c of the composite was measured in the free torsional pendulum. The value was found to be $G_c = (20.7 \pm 0.6)$ GPa. Although the mathematical analysis of torsion is much more complicated than the one of flexion, we tried to use the same formula (5.28) for the shear modulus of the composite. Then the shear modulus of the quasicrystalline coating alone was found to be only $G_1 = 6.2$ GPa. This result can be explained again by the presence of cracks and pores.

Moreover, the shear modulus of the composite increases with temperature (see Fig. 3.13). This shear modulus anomaly will be discussed in section 5.3.

The coefficient of thermal expansion of icosahedral Al-Cu-Fe was reported to be in the range of $(8.5\text{–}26.0)\times10^{-6}\,\mathrm{K}^{-1}$ [Korsunsky et al., 2001]. We have chosen the value $20\times10^{-6}\,\mathrm{K}^{-1}$ because the thermal expansion of the coating appears to be higher than the one of the steel substrate as can be seen from the specimen bending with increasing

Parameter	Value	Unit
E	28	GPa
$(dE/dT)/E$	-0.2×10^{-4}	K^{-1}
G	6.2	GPa
$(dG/dT)/G$	?	K^{-1}
α	20×10^{-6}	K^{-1}
ν	0.34	1

Table 3.4: Summary of the mechanical parameters values for the decagonal Al-Cu-Fe-Cr coating.

temperature.

3.3 Mechanical spectroscopy

3.3.1 Different thicknesses of the quasicrystalline coating

The internal friction spectra of the steel substrate with three different thicknesses of the coating for temperatures between 300 K and 600 K together with the internal friction spectrum of the steel substrate alone are shown in Fig. 3.14. The thickness of the steel substrate is always h_2=593 µm. However, the thickness of the quasicrystalline coating h_1 varies between 236 and 434 µm. It can be seen that the internal friction of the composite increases with the thickness of the quasicrystalline coating, while the internal friction of the steel substrate alone is much smaller.

If the elastic energy dissipation at the interface is neglected, it is possible to calculate the internal friction of the quasicrystalline coating alone Q_1^{-1} from the measured internal frictions of the composite Q_c^{-1} and the substrate Q_2^{-1}, using the "rule of mixture" [Nishino and Asano, 1993; Weller, 2001]

$$Q_c^{-1} = \frac{W_1\, Q_1^{-1} + W_2\, Q_2^{-1}}{W_1 + W_2}, \tag{3.2}$$

where W_1 and W_2 are the elastic strain energies of the quasicrystalline coating and the steel substrate, respectively. They can be determined by a volume integration

$$W = \frac{G}{2} \iiint \varepsilon_0^2\,(x, y, z)\; dx\, dy\, dz, \tag{3.3}$$

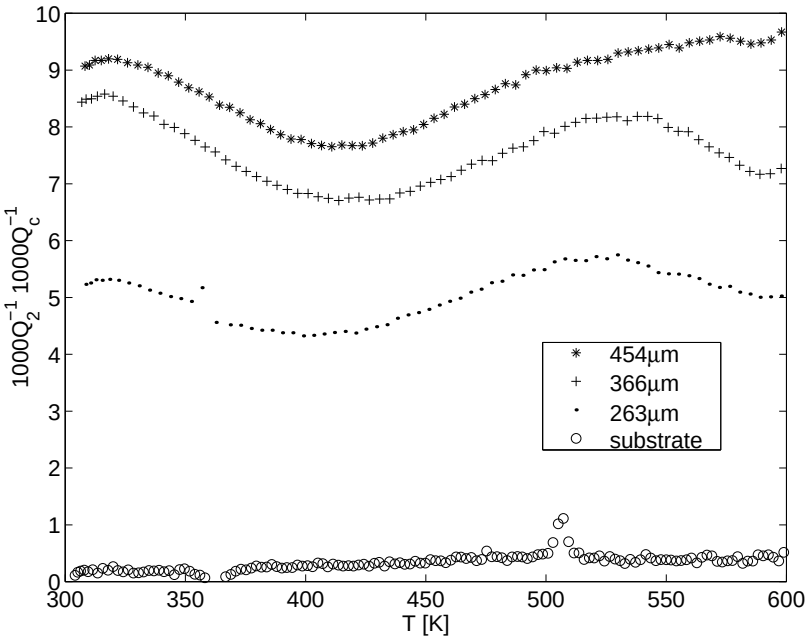

Figure 3.14: Measured internal friction spectra of the composite with different thicknesses of the coating on a 593 µm steel substrate and of the substrate alone, 1 Hz, 1 K/min.

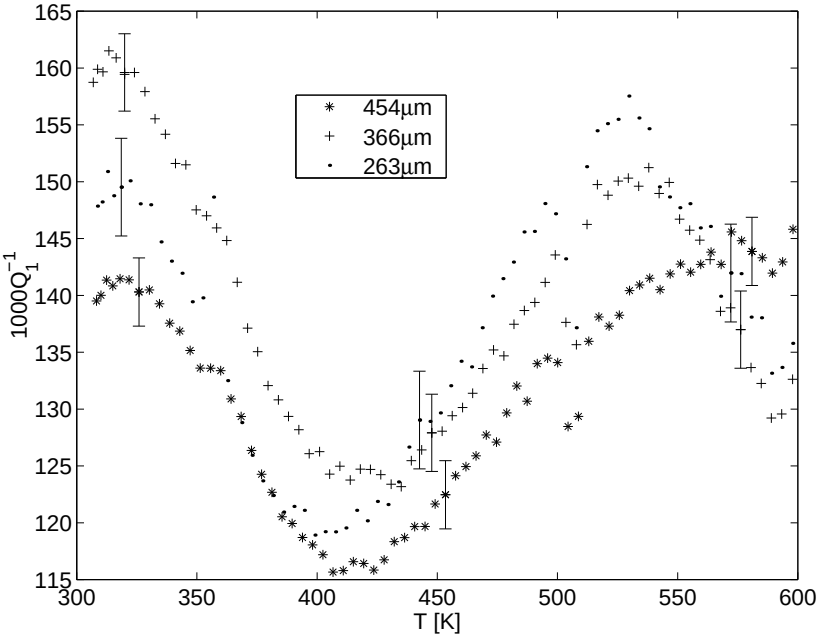

Figure 3.15: Calculated internal friction spectra of the quasicrystalline coating without the substrate for three different coating thicknesses, 1 Hz, 1 K/min.

where G is the appropriate shear elastic modulus and ε_0 is the strain amplitude. For the torsional deformation of a plate shaped composite specimen, the strain energies are given by the equations (2.11) and (2.16)

$$W_1 = \frac{1}{2\,l} G_1\,\beta\,\Theta^2\,h^2\,h_1\,d, \tag{3.4}$$

$$W_2 = \frac{1}{2\,l} G_2\,\beta\,\Theta^2\,h^2\,h_2\,d, \tag{3.5}$$

where l, h, d are the sample dimensions, β is a numerical coefficient for torsion of a rectangular bar[2] and Θ is the twist angle. Then the equation (3.2) reduces to

$$Q_c^{-1} = \frac{G_1\,h_1\,Q_1^{-1} + G_2\,h_2\,Q_2^{-1}}{G_1\,h_1 + G_2\,h_2}. \tag{3.6}$$

The resulting calculated internal friction of the quasicrystalline coating Q_1^{-1} is shown in Fig. 3.15. The error bars are calculated from estimated errors of $\pm 10\,\mu m$ on the thicknesses h_1 and h_2. The mechanical losses for the three different thicknesses concur within the error bars, which indicates that the internal friction of the composite is mostly caused by the quasicrystalline coating and that the contributions of the steel substrate and the interface are small.

The following parts of this work will deal with two different thicknesses h_1 of the coating. One is $h_1 = 454\,\mu m$ (the initial thickness) and the other is $h_1 = 271\,\mu m$, while the thicknesses of the substrate are $h_2 = 593\,\mu m$ and $h_2 = 560\,\mu m$, respectively.

3.3.2 Athermal internal friction maximum

When isochronal measurements are carried out between 300 K and 700 K using a frequency of 1 Hz, an internal friction maximum is observed around 600 K (see Fig. 3.16). Three associated unexpected phenomena are observed. Firstly, this maximum is not frequency-dependent; secondly, it depends on the thermal history of the sample and thirdly, the maximum does not exist in isothermal measurements (see 500 and 600 K spectra in Fig. 3.17).

It can be concluded that the maximum is not thermally activated. The possibility of a phase transformation was excluded by differential calorimetric (DSC) tests (see Fig. 3.18), although the first DCS curve shows a small artifact peak at 625 K, which is common in the first DSC heating cycle and which is not related to any phase transformation. Moreover, the maximum in internal friction measurements is stable with

[2] for d/h=4 β=0.28166567, other values can be found in Tab. 2.2

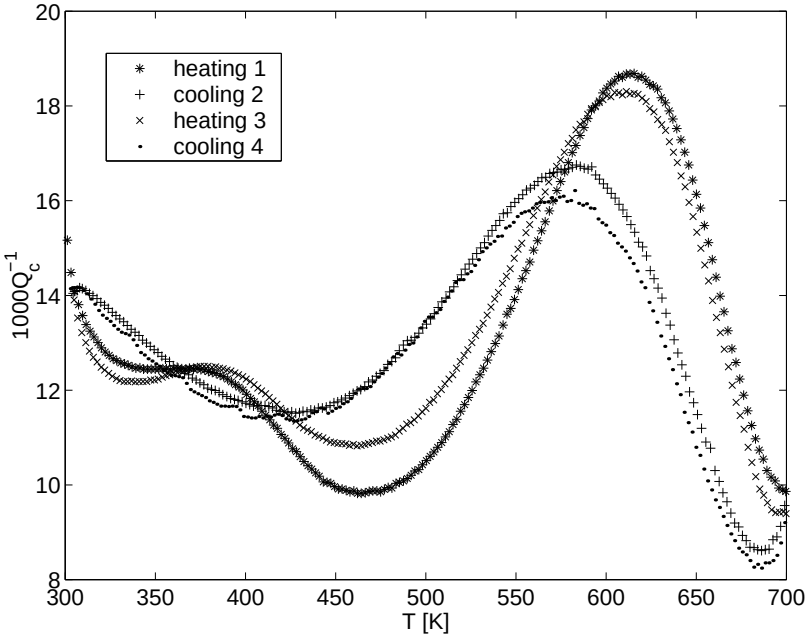

Figure 3.16: Isochronal internal friction spectra at 1 Hz showing a maximum around 611 K during heating and 577 K during cooling, 0.5 K/min, $h_1 = 454\,\mu m$, $h_2 = 593\,\mu m$.

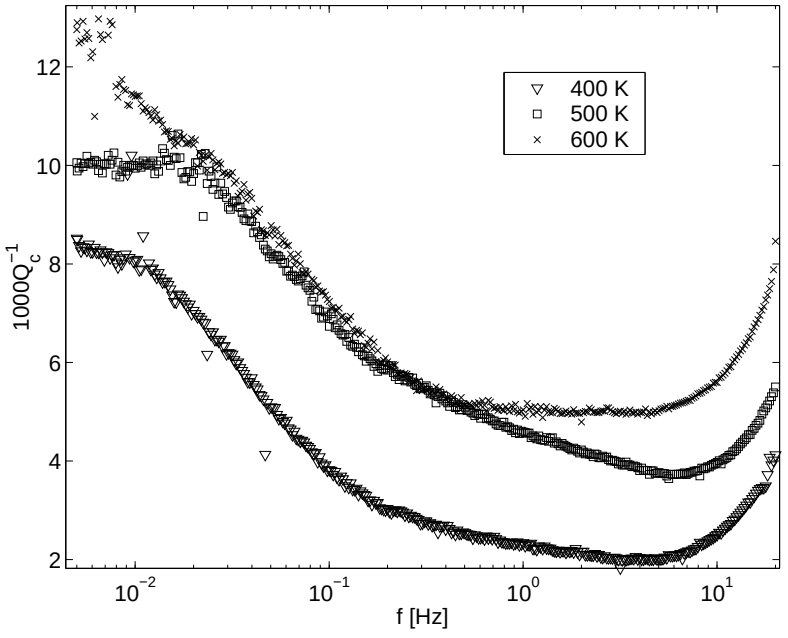

Figure 3.17: Isothermal internal friction spectra without any maximum, $h_1 = 454\,\mu m$, $h_2 = 593\,\mu m$.

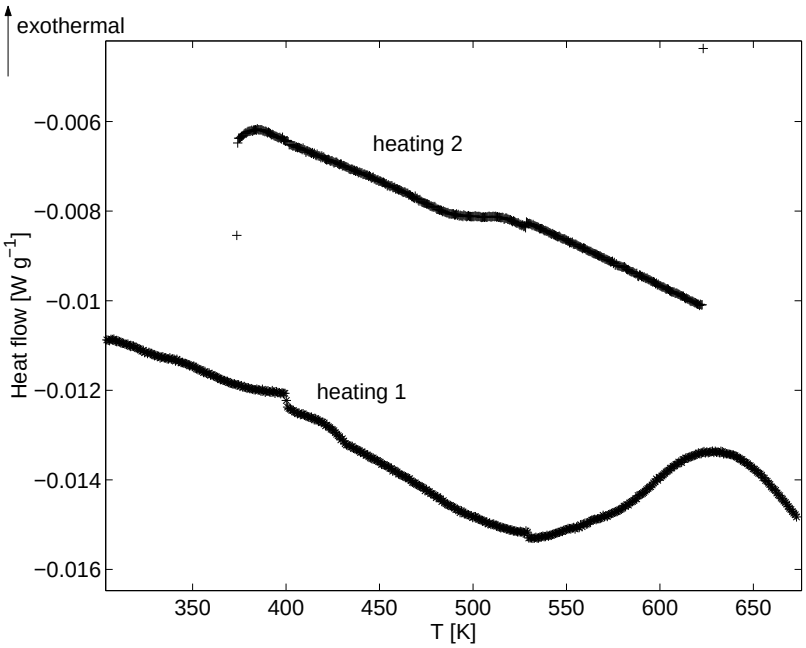

Figure 3.18: DSC of the quasicrystalline coating at 1 K/min.

respect to repeated measurements and consequently, it cannot be explained by a phase transformation.

The internal friction substantially decreases as a result of a 40-hour long thermal cycling between 450 K and 570 K (see Fig. 3.19). Therefore, this mechanical loss is probably induced by thermal stresses within the substrate or the coating and a stress relaxation is observed.

In order to determine if the maximum is related to thermal stresses inside the coating or inside the substrate, same measurements were performed with another thickness of the coating $h_1 = 271\,\mu m$ and with similar thickness of the substrate $h_2 = 560\,\mu m$ (see Fig. 3.20). The peaks are shifted toward a lower temperature by 33 K and 18 K for heating and cooling stages, respectively, which will be interpreted in section 5.4 as a solid friction occurring inside the quasicrystalline coating.

3.3.3 High temperature exponential background

A high-temperature reversible background is observed at temperatures higher than 700 K (see Fig. 3.21). It has an exponential shape and it can be interpreted as the onset of the brittle-to-ductile transition in the quasicrystalline coating.

The thermally activated high temperature exponential background can be treated as

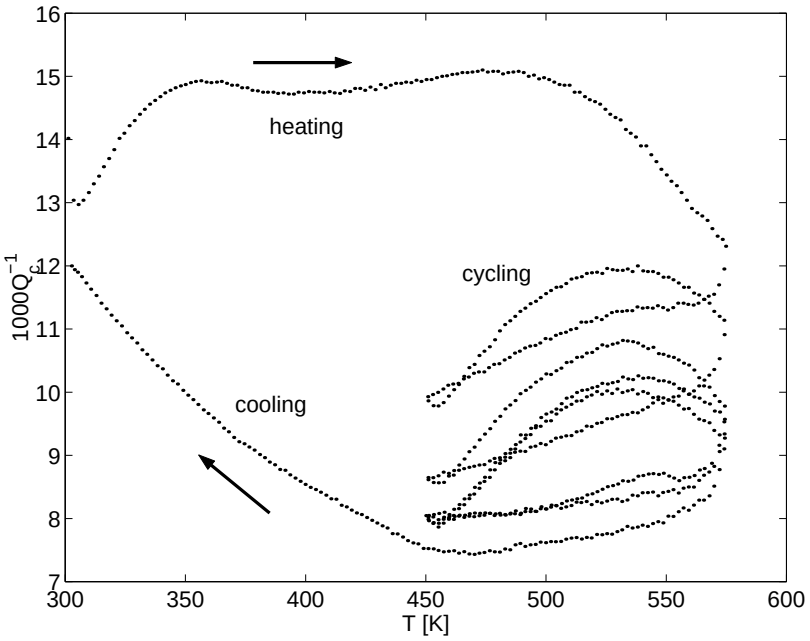

Figure 3.19: Thermal cycling showing a decrease of damping with increasing time, 1 Hz, 0.5 K/min, $h_1 = 454\,\mu m$, $h_2 = 593\,\mu m$.

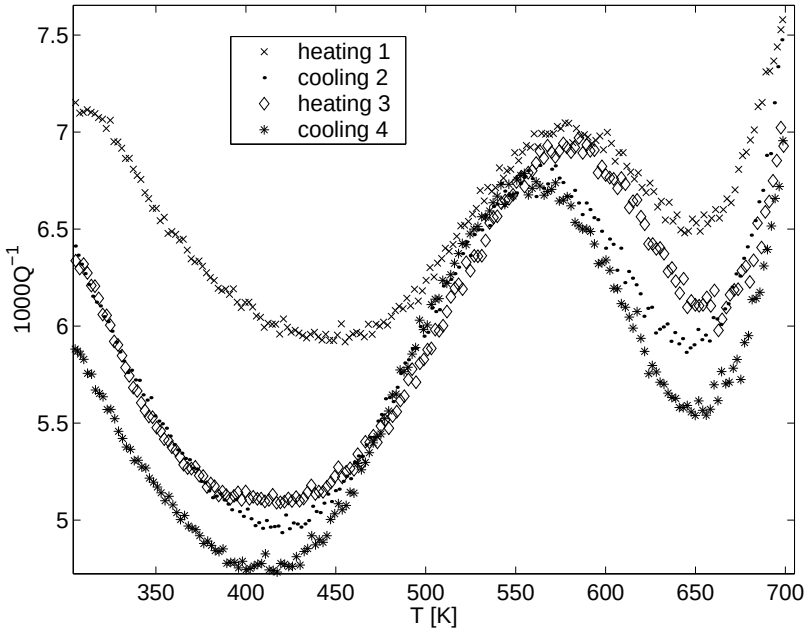

Figure 3.20: Isochronal internal friction spectra at 1 Hz showing maximum around 578 K during heating and 560 K during cooling, 0.5 K/min, $h_1 = 271\,\mu m$, $h_2 = 560\,\mu m$.

the onset of a relaxation Debye peak occurring at higher temperatures. On the basis of the Debye peak equation (1.29) and the equation of thermal activation (1.30) with the condition $\tau\omega \gg 1$, the internal friction can be calculated

$$Q^{-1} = \frac{\Delta}{\omega\tau_0} e^{-\frac{H}{kT}}. \tag{3.7}$$

It has an exponential shape and can also be used to determine the activation enthalpy H. The limit relaxation time τ_0 cannot be determined as the relaxation strength Δ is not known.

From Fig. 3.21 an "apparent" value of the activation enthalpy $H' = (0.45 \pm 0.01)$ eV was determined. The apparent activation enthalpy value can be corrected by considering a distribution of relaxation times [Schoeck et al., 1964]

$$Q^{-1} = \frac{C}{\omega^{\alpha}} e^{-\frac{\alpha H}{kT}}, \tag{3.8}$$

where C is a constant, ω is the angular frequency and $1/\alpha$ is the broadening factor. The activation enthalpy value obtained from several isochronal measurements of the exponential background with different frequencies does not need to be corrected, as from the equation (3.8) the slope of an Arrhenius plot of points with Q^{-1}=const. equals directly to the true enthalpy H.

The value α can be obtained from the slope of an isothermal log-log plot (see Fig. 3.22). The fit gives a broadening factor $1/\alpha = 4.45 \pm 0.07$. Thus, the true activation enthalpy is $H = (2.00 \pm 0.05)$ eV.

Measurements in the free-free vibrating bar apparatus (see Fig. 3.23) also show a high-temperature exponential background with an apparent activation enthalpy of $H' = (0.425 \pm 0.003)$ eV. The correction by the broadening factor (see Fig. 3.22) gives a true enthalpy $H = (1.89 \pm 0.03)$ eV which agrees with the value found using the forced torsion pendulum.

The same measurement was repeated for the sample with smaller thickness of the coating $h_1 = 271$ µm and similar thickness of the substrate $h_2 = 560$ µm (see Fig. 3.24). The apparent activation enthalpy value in this case is $H' = (0.414 \pm 0.006)$ eV and the broadening factor $1/\alpha = 4.24 \pm 0.08$ (see Fig. 3.25). Hence, the true activation enthalpy is $H = (1.76 \pm 0.04)$ eV which is still close to the values found for the thicker coating.

To exclude the possibility that this high-temperature exponential background is related to the steel substrate, the same measurement was carried out on the mild steel substrate alone. Fig. 3.26 shows no increase of the internal friction at high temperature.

The observed high-temperature exponential background will be interpreted in section 5.5 as the onset of the brittle-to-ductile transition in the quasicrystalline coating.

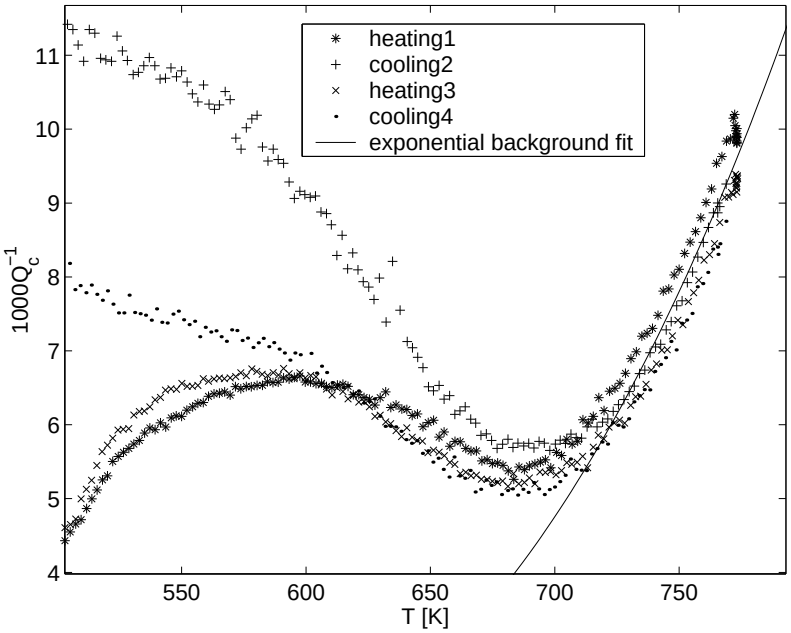

Figure 3.21: Exponential background as measured in the forced torsion pendulum, 1 Hz, 0.5 K/min, $h_1 = 454\,\mu m$, $h_2 = 593\,\mu m$.

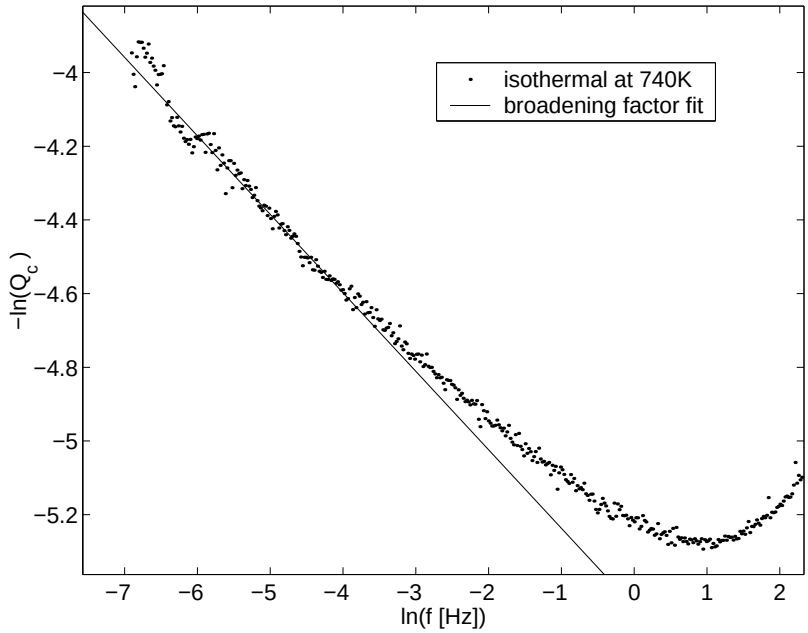

Figure 3.22: Fit providing the broadening factor $1/\alpha$, $h_1 = 454\,\mu m$, $h_2 = 593\,\mu m$.

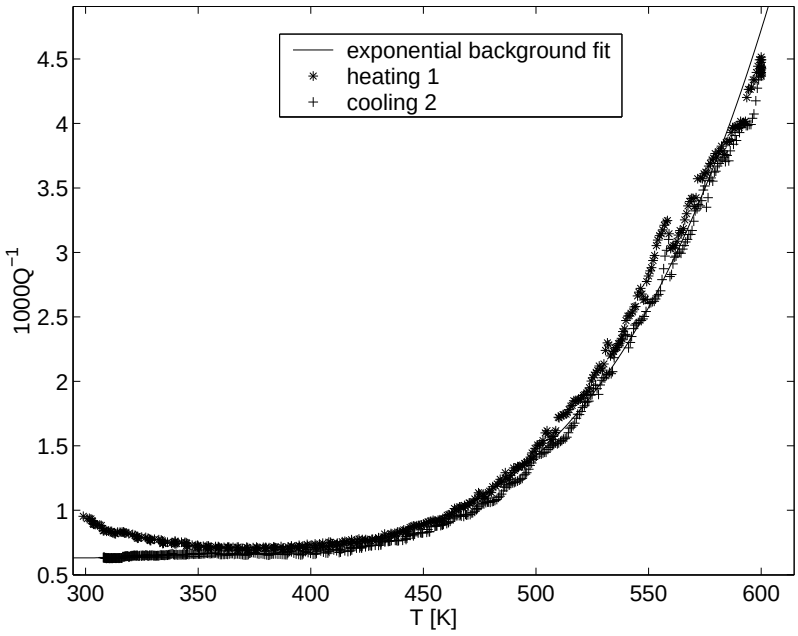

Figure 3.23: Exponential background as measured in the free-free vibrating bar apparatus, 2.3 kHz, 0.5 K/min, $h_1 = 454$ µm, $h_2 = 593$ µm.

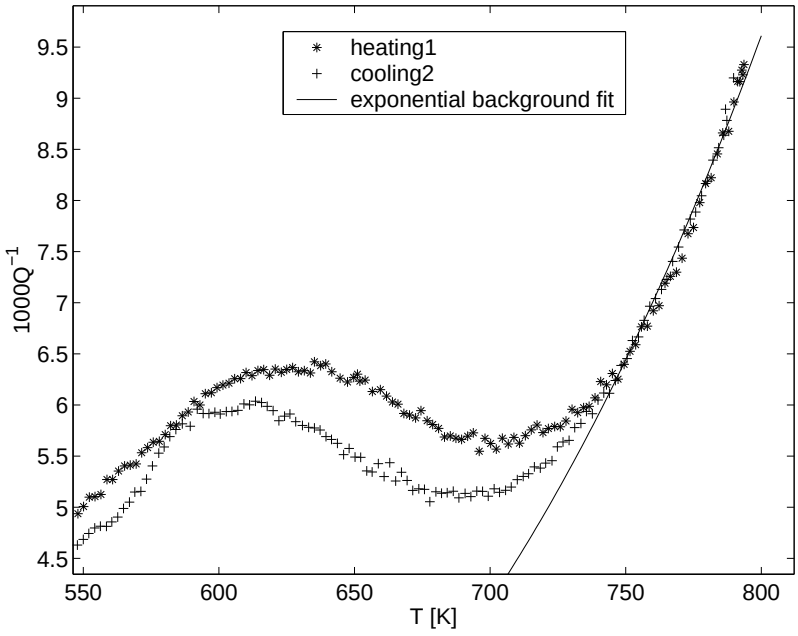

Figure 3.24: Exponential background as measured in the forced torsion pendulum, 1 Hz, 0.5 K/min, $h_1 = 271$ µm, $h_2 = 560$ µm.

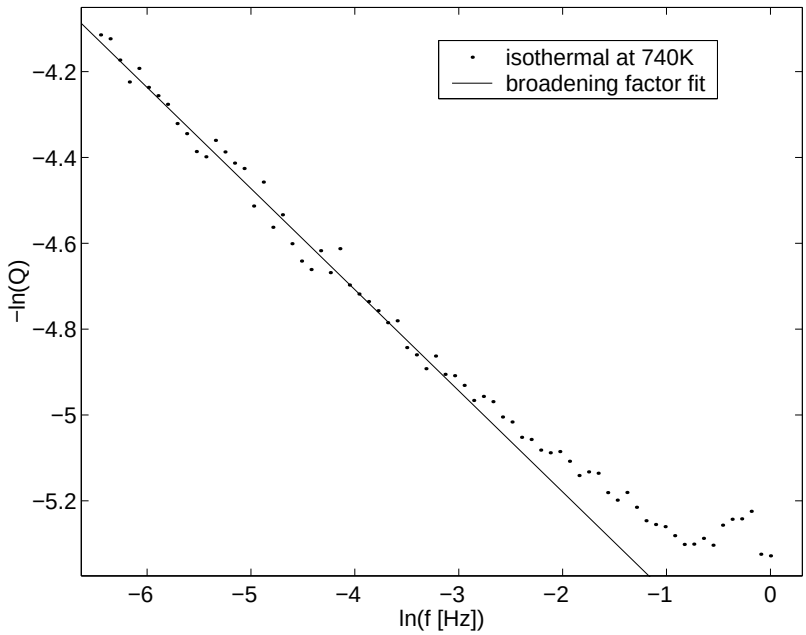

Figure 3.25: Fit providing the broadening factor $1/\alpha$, $h_1 = 271\,\mu m$, $h_2 = 560\,\mu m$.

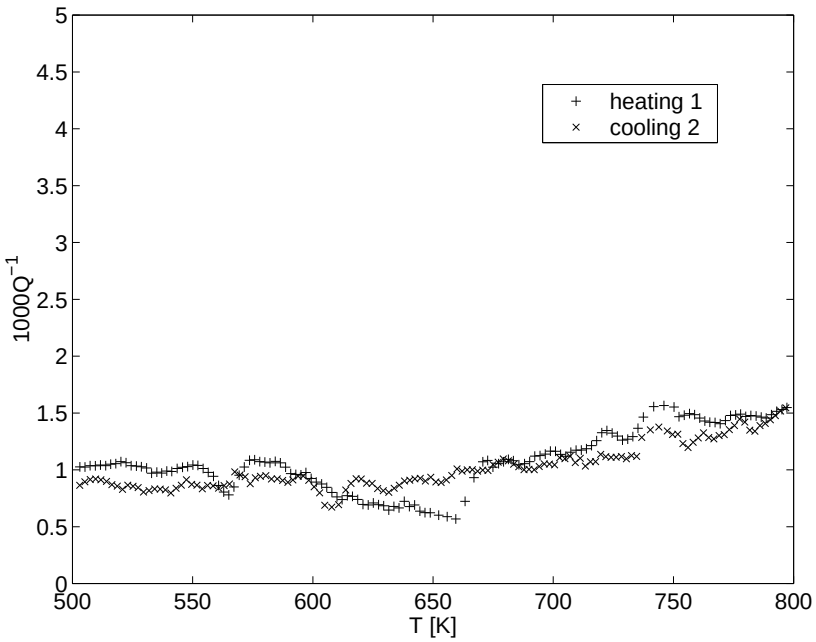

Figure 3.26: Isochronal measurements of the mild steel substrate, 1 Hz, 0.5 K/min.

Chapitre 4

Experimental results - Composites

4.1 Elaboration

Composites reinforced with icosahedral Al-Cu-Fe quasicrystalline particles with the average grain size of 50 µm (see Figs. 4.1 and 4.2) were prepared by the gas pressure infiltration technique described in section 2.1.2. Altogether, seven infiltrations were carried out; all the processing conditions are summarised in Tab. 4.1.

The processing temperature was chosen in order to obtain the lowest liquid metal viscosity while preventing any major phase transformation of the quasicrystalline powder.

Unfortunately, the used processing method does not allow an easy control of the volume fraction of the reinforcement material. The volume fraction of the Al-Cu-Fe powder was always close to 80%.

4.2 X-ray diffractometry

The structure of the quasicrystalline powder was checked by XRD after ball-milling in order to verify that no phase transformation occurred. The powder was also once heated in vacuum to 750°C and then checked by XRD. The structure of the powder was still quasicrystalline and the possibility of a phase transformation occurring during heating inside the infiltration apparatus was therefore excluded. Nevertheless, a phase transformation can occur when the powder comes in contact with molten aluminium or magnesium.

Infiltration number	Matrix	T_{alloy} [°C]	$T_{preform}$ [°C]	p_{Ar} [bar]
1	Al-3wt.%Mg	770	770	20
2	Al-3wt.%Mg	730	700	30
3	Al_3Mg_2	600	550	30
4	Al_3Mg_2	600	550	30
5	Al_3Mg_2	550	500	30
6	AZ63	700	780	30
7	WFA	750	750	32

Table 4.1: Summary of the infiltration processing conditions. The composition of AZ63 is Mg-6wt.%Al-2wt.%Zn-0.25wt.%Mn and the one of WFA is Al-4wt.%Cu-1wt.%Mg-0.5wt.%Ag.

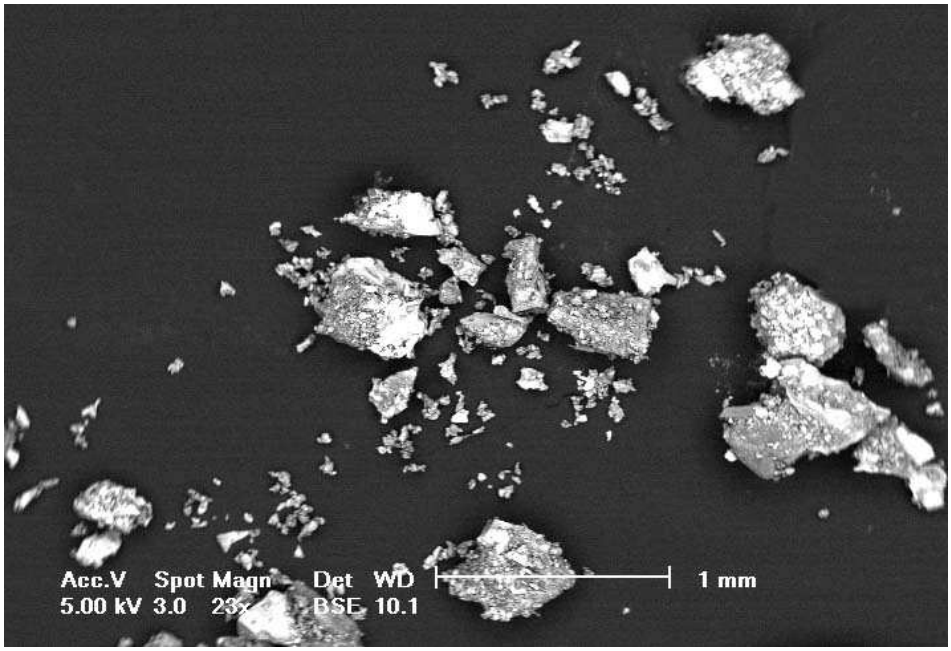

Figure 4.1: SEM of the Al-Cu-Fe quasicrystalline powder with a heterogeneous distribution of the grain size.

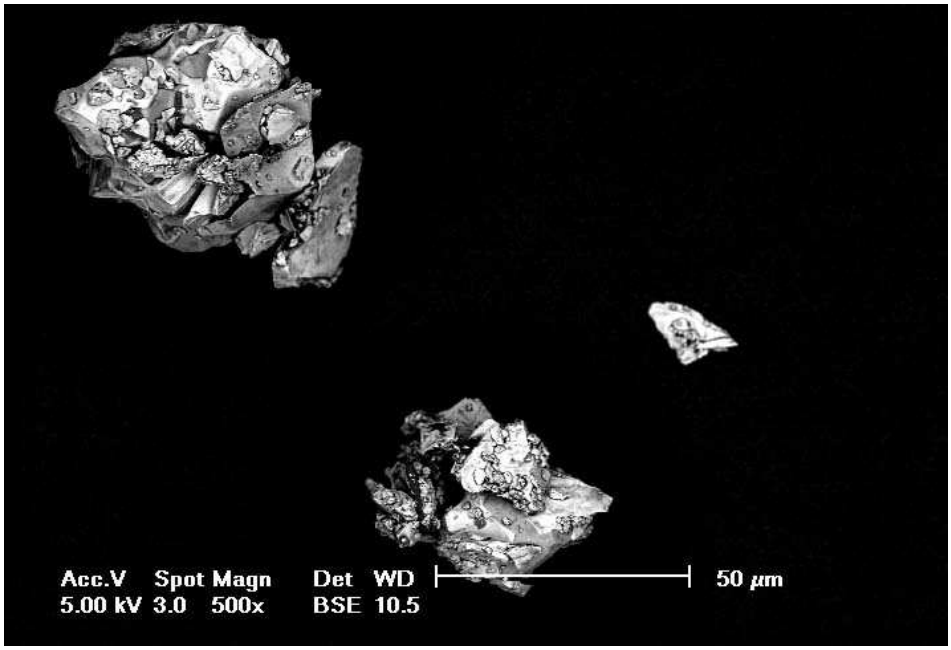

Figure 4.2: SEM of a mid size Al-Cu-Fe quasicrystalline grain. Note the particle agglomeration.

XRDs of the composites with different matrices are shown in Figs. 4.3–4.6. The presence of the two strongest peaks at the positions $2\Theta = 42.939°$ and $2\Theta = 45.260°$ (see Fig. 2.6) is a sign of the presence of the icosahedral phase. They can be clearly seen in the case of an Al_3Mg_2 matrix (see Fig. 4.4) and also in the case of an Al-3wt.%Mg matrix (see Fig. 4.3) but with much smaller intensity. For the AZ63 (Mg-6wt.%Al-2wt.%Zn-0.25wt.%Mn) and WFA (Al-4wt.%Cu-1wt.%Mg-0.5wt.%Ag) matrices (see Figs. 4.5 and 4.6) the icosahedral peaks are not visible; either their intensity is too small or they are masked by other peaks.

In summary the XRD measurements evidenced a strong phase transformation of the icosahedral Al-Cu-Fe reinforcement in the case of the AZ63 and WFA matrices, i.e. no quasicrystalline phase was detected. Some quasicrystalline phase was found in the case of the Al-3wt.%Mg matrix and a lot of quasicrystalline phase was found in the case of the Al_3Mg_2 matrix.

The most important infiltration parameter seems to be the processing temperature. If it is low, the viscosity of the melted alloy is high and prevents the infiltration of the quasicrystalline powder. On the other hand, if the processing temperature is too high, a phase transformation of the quasicrystalline particles by diffusion of liquid aluminium

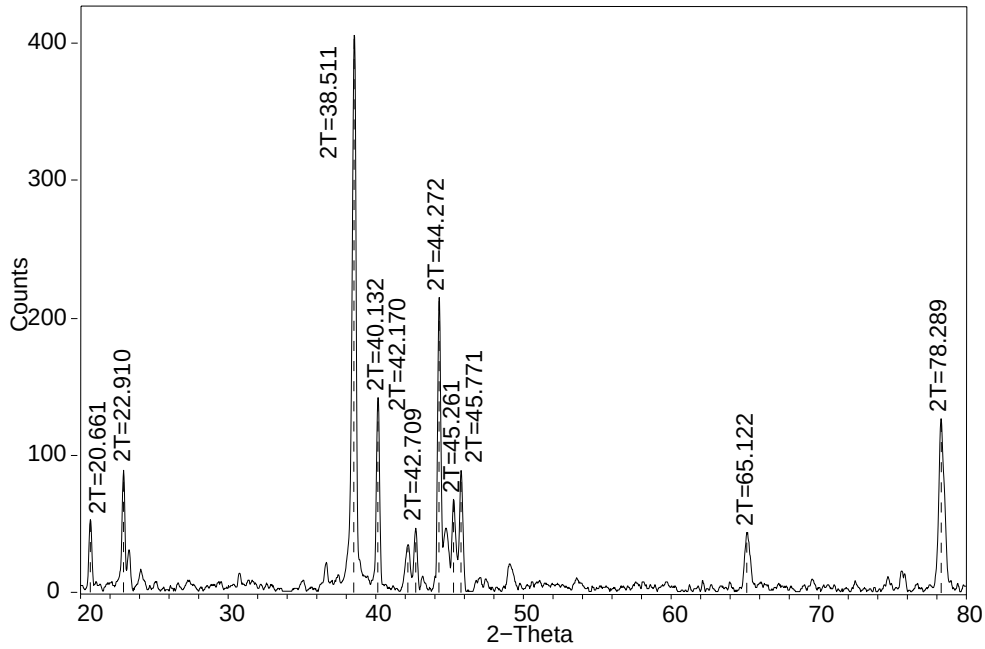

Figure 4.3: X-ray diffractogram of a composite; matrix Al-3wt.%Mg reinforced with the icosahedral Al-Cu-Fe powder, CuK_α radiation, 0.5°/min scan speed.

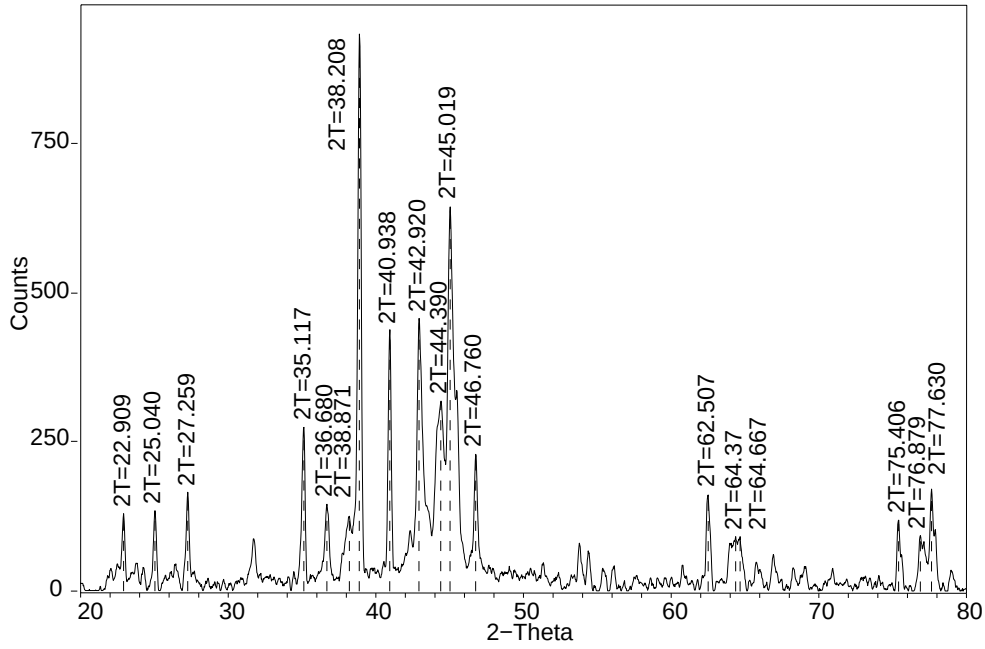

Figure 4.4: X-ray diffractogram of a composite; matrix Al_3Mg_2 reinforced with the icosahedral Al-Cu-Fe powder, CuK_α radiation, 0.5°/min scan speed.

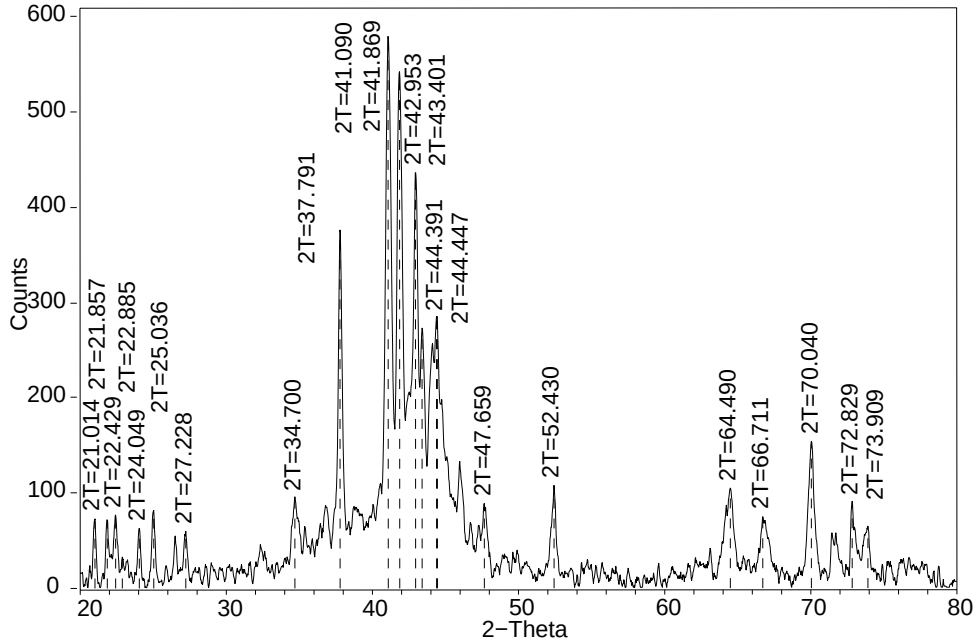

Figure 4.5: X-ray diffractogram of a composite; matrix AZ63 reinforced with the icosahedral Al-Cu-Fe powder, CuK$_\alpha$ radiation, 0.5°/min scan speed.

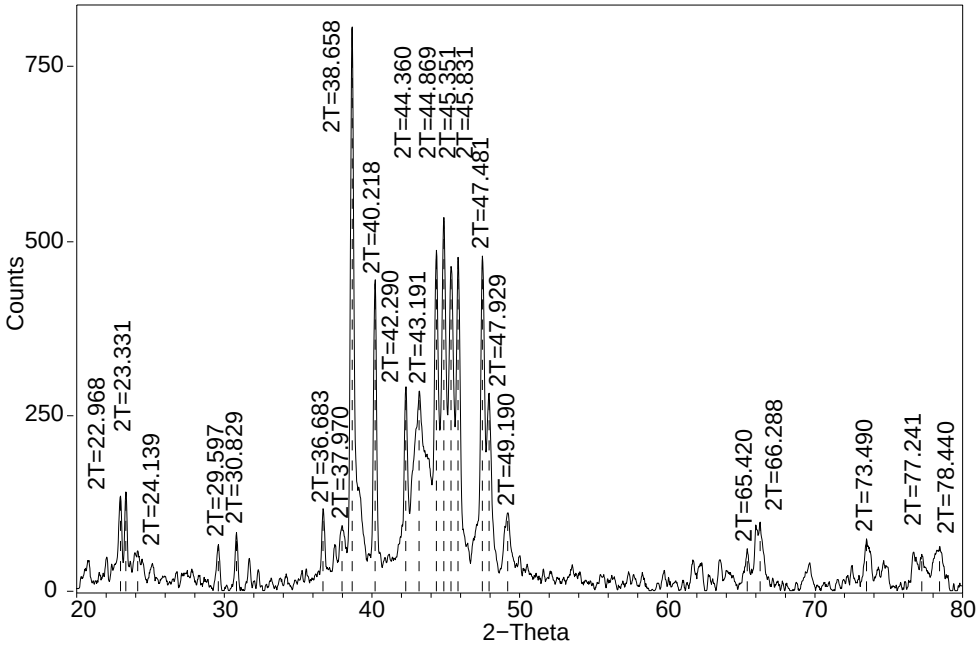

Figure 4.6: X-ray diffractogram of a composite; matrix WFA reinforced with the icosahedral Al-Cu-Fe powder, CuK$_\alpha$ radiation, 0.5°/min scan speed.

or magnesium occurs.

In order to prevent any massive phase transformation of the quasicrystalline powder, it is necessary to choose a metal matrix with a low melting temperature, as e.g. the eutectic Al_3Mg_2.

4.3 Microscopy

The obtained composites are brittle and contain numerous pores and cracks. The scanning electron micrographs of the composites, which can be seen in Figs. 4.7–4.12, confirm the results of XRD measurements by showing that a massive phase transformation destroyed the icosahedral phase, and resulted in a dendritic precipitation in the case of the AZ63 and WFA matrices. A less important phase transformation also with dendritic precipitation was detected in the case of the Al-3wt.%Mg matrix, and in the case of the Al_3Mg_2 matrix only a slight phase transformation around the grain surfaces was observed.

The contact of the quasicrystalline particles with the melted *Al-3wt.%Mg matrix* led to a partial transformation of their structure. In general, the grains with large dimensions did not transform, however, the shape, chemical composition and lattice type of small and average-size grains changed (see Fig. 4.7). The detail of a transformed grain in Fig. 4.8 shows the dendritic growth of transformed phases, but even in such regions a non-negligible occurrence of the icosahedral phase can be observed. The material can thus profit from the high strength of the quasicrystalline phase, while the complicated dendritic shape of the particles guarantees a good cohesion with the matrix.

In the composite with the *Al_3Mg_2 eutectic matrix* the quasicrystalline grains are well conserved (see Fig. 4.9). The transformed zones surround the particles and form the transition between the particles and the matrix (see Fig. 4.10). The thickness of the transformed layers is of the order of magnitude of tens microns. This composite has the highest content of the icosahedral phase. Unfortunately, it is very brittle as the eutectic matrix itself is also brittle.

During the preparation of the *AZ63 matrix* composite, the whole icosahedral phase transformed into crystalline phases. The micro-structure consists of a complicated dendritic arrangement (see Fig. 4.11).

As in the previous case, the quasicrystalline phase is destroyed by the contact with the molten *WFA matrix*. The particles were again transformed by the dendritic growth of secondary phases, as documented in Fig. 4.12.

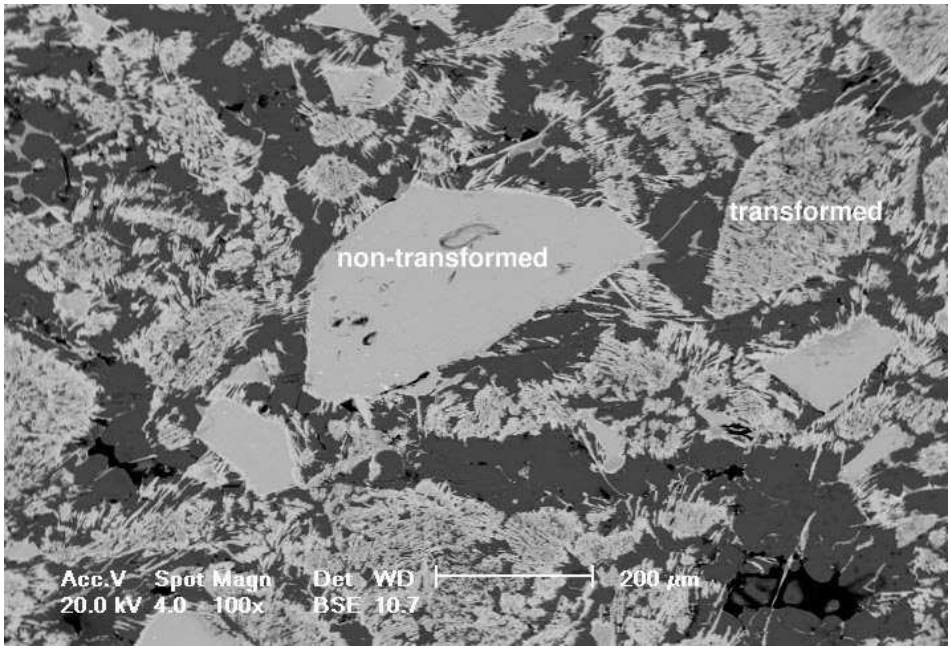

Figure 4.7: SEM of a composite; matrix Al-3wt.%Mg reinforced with the icosahedral Al-Cu-Fe powder, showing some transformed and some non-transformed grains.

The following parts of this work will focus on the investigation of the composites with either the Al-3wt.%Mg or the Al_3Mg_2 matrix because they contain quasicrystalline particles.

4.4 Mechanical tests

The mechanical properties of some of the obtained composites were compared to composites reinforced with 25 vol.% Al_2O_3 short fibres (saffil), which are a commonly used as high strength ceramic-base reinforcement material. It is obvious that the comparison is not very objective because in our case the volume fraction of the Al-Cu-Fe quasicrystalline particles is 80%.

Vickers micro-hardness measurements of the composites and the reinforcement materials alone were carried out by using a Durimet Leitz Wetzlar indenter. At least ten indentations at room temperature were performed for each material. The average values of the micro-hardness are summarised in Tab. 4.2. The hardness of the composites

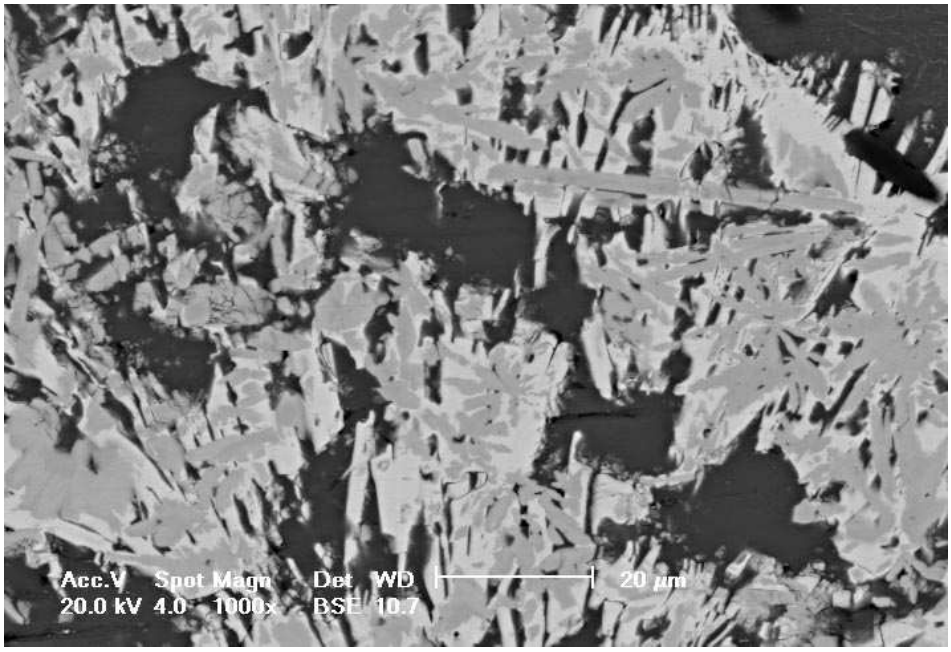

Figure 4.8: SEM of a composite; matrix Al-3wt.%Mg reinforced with the icosahedral Al-Cu-Fe powder. Detail of a transformed grain; white areas have the icosahedral structure while grey regions have the composition $Al_{70.3}Cu_{5.5}Fe_{22.7}$.

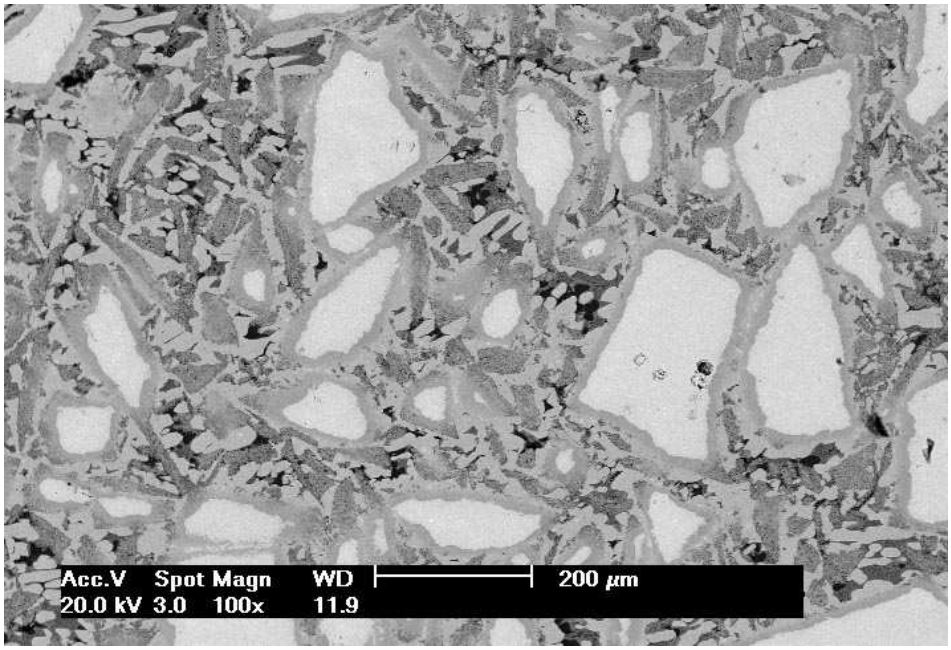

Figure 4.9: SEM of a composite; matrix Al_3Mg_2 reinforced with the icosahedral Al-Cu-Fe powder. Quasicrystalline grains (white) surrounded by a transformed layer can be seen.

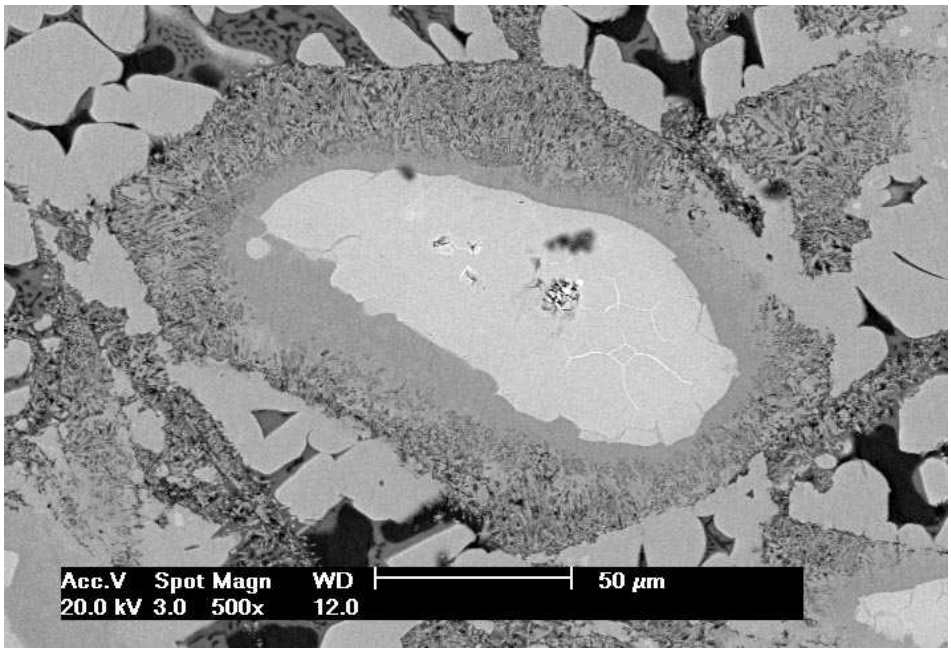

Figure 4.10: SEM of a composite; matrix Al_3Mg_2 reinforced with the icosahedral Al-Cu-Fe powder. Detail of a quasicrystalline grain.

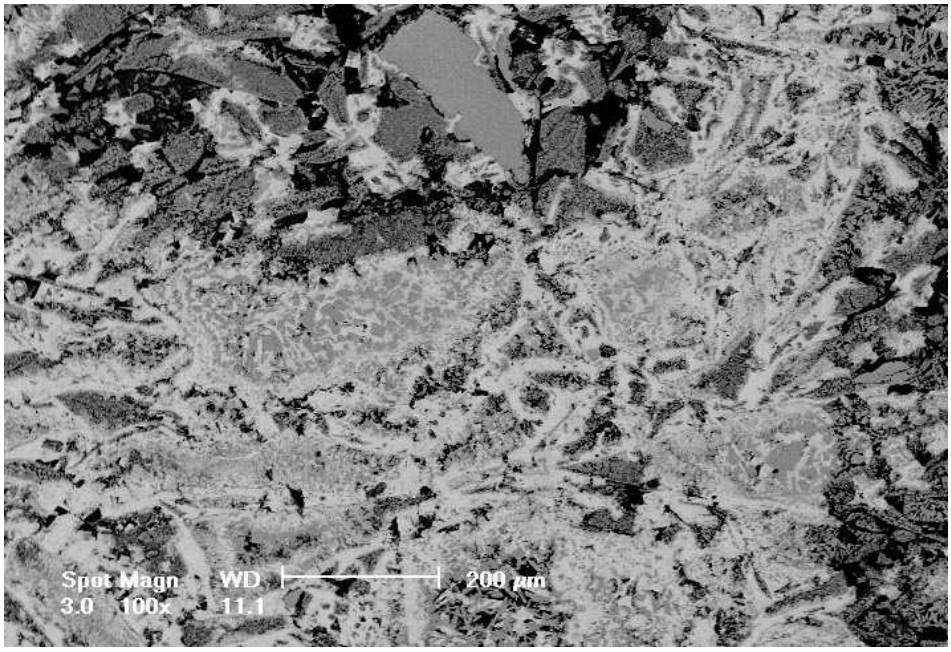

Figure 4.11: SEM of a composite; matrix AZ63 reinforced with the icosahedral Al-Cu-Fe powder. Transformed grains.

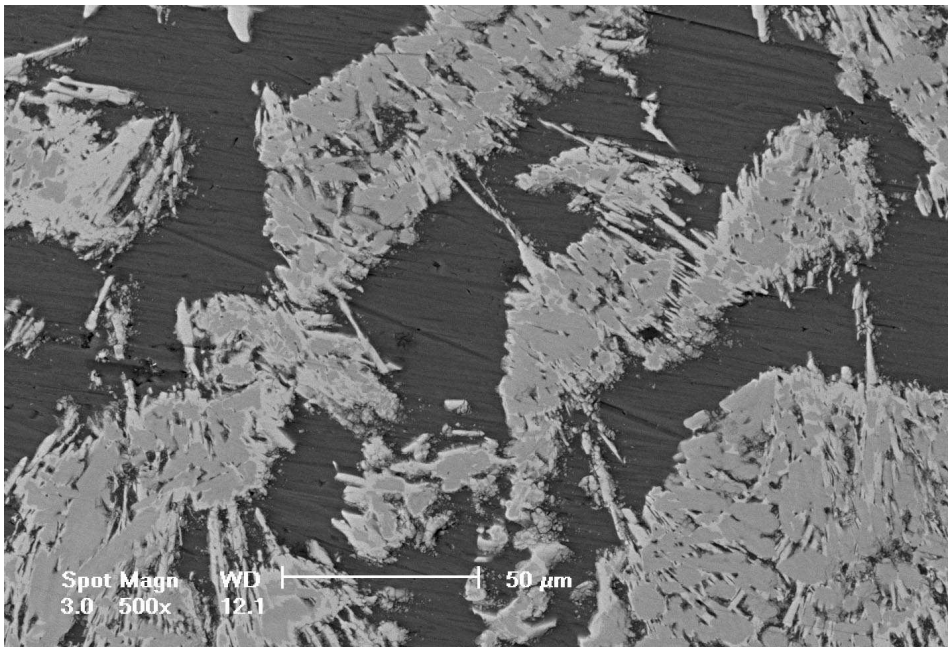

Figure 4.12: SEM of a composite; matrix WFA reinforced with the icosahedral Al-Cu-Fe powder. Transformed grains.

Material	H_v [GPa]
Al-3wt.%Mg+Al-Cu-Fe	7.0
Al-3wt.%Mg+Al_2O_3	4.0
Al_3Mg_2+Al-Cu-Fe	8.2
Al_3Mg_2+Al_2O_3	8.4
Al-Cu-Fe	10.0
Al_2O_3	19.0

Table 4.2: Vickers micro-hardness measurements of the composites and the reinforcement materials.

Material	Young's modulus E [GPa]	Ultimate stress σ_u [MPa]
Al_3Mg_2+Al-Cu-Fe	276	765
Al_3Mg_2+Al_2O_3	98	670
Al-Cu-Fe	238	900
Al_2O_3	300	-

Table 4.3: Mechanical properties of the composites and the reinforcement materials.

reinforced with Al-Cu-Fe particles is close to the hardness of the quasicrystalline Al-Cu-Fe bulk material itself. The Al_3Mg_2 matrix appears to be harder than Al-3wt.%Mg but it is also more brittle.

Next, compression tests were performed at room temperature on the composite with the Al_3Mg_2 matrix reinforced with either Al-Cu-Fe particles or with Al_2O_3 short fibres. The samples had dimensions of $4\times4\times10$ mm. Typical stress-strain curves can be seen in Fig. 4.13. The slope of the elastic part, as corrected by the equation (2.4), gives the Young's modulus E. The Young's modulus and the ultimate compression stress σ_u are compared in Tab. 4.3 for two composites and two reinforcements. The values obtained for the composite reinforced with Al-Cu-Fe particles are again close to the values exhibited by bulk Al-Cu-Fe quasicrystals [Giacometti, 1999].

4.5 Mechanical spectroscopy

Mechanical spectroscopy measurements were performed using the forced torsion pendulum and the free-free vibrating bar apparatus in the temperature range 300–600 K.

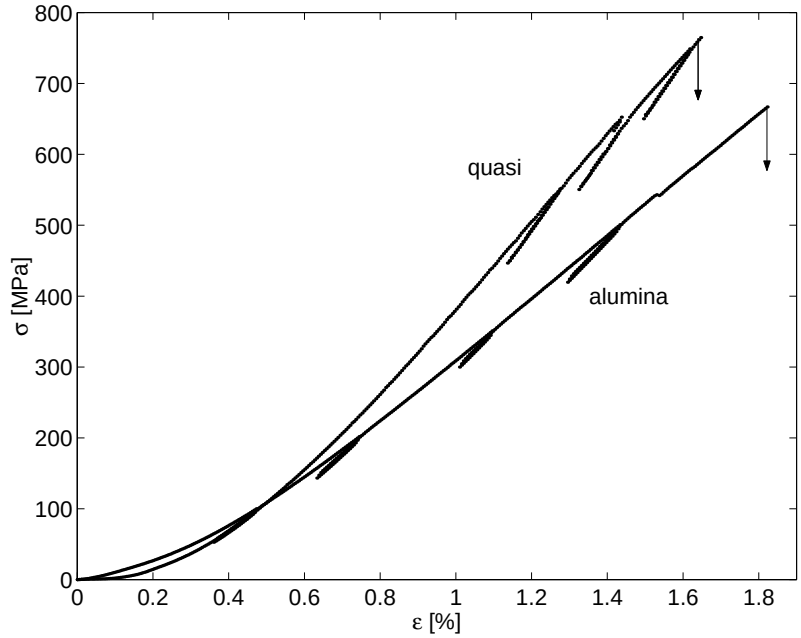

Figure 4.13: True stress-strain compression curves at room temperature of Al_3Mg_2 matrix composites reinforced with either quasicrystalline Al-Cu-Fe particles or with Al_2O_3 short fibres (alumina). The imposed deformation speed is $\dot{\varepsilon} = 11.2 \times 10^{-5}\,\mathrm{s}^{-1}$.

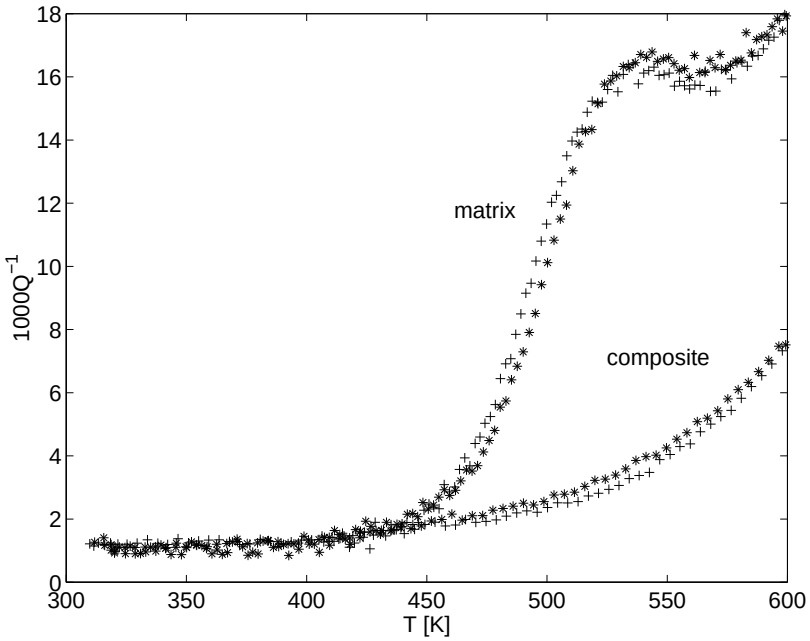

Figure 4.14: Isochronal internal friction spectra of the Al-3wt.%Mg matrix composite reinforced with Al-Cu-Fe particles and of the matrix alone, as measured in the inverted forced torsion pendulum, 1 Hz, 0.5 K/min.

4.5.1 Al-3wt.%Mg matrix composite

It was found that the internal friction spectra of the Al-3wt.%Mg matrix composite exhibit a simple exponential increase with temperature (see Fig. 4.14) while the internal friction of the matrix alone shows a maximum of the mechanical loss around 520 K. This phenomenon was already observed in Al-Mg alloys [Belson et al., 1970] and could be related to the dragging of magnesium solute atoms by dislocations. This effect is not present in the composite probably because of a change in the matrix composition occuring during the partial transformation of the quasicrystalline particles.

The shear modulus of the composite and of the matrix alone decreases with increasing temperature (see Fig. 4.15), which is typical for metals.

The shift of the high temperature exponential background with the applied frequency in isochronal measurements, as described by the equation (3.7), allows the drawing of an Arrhenius plot (see Fig. 4.16). The measured activation enthalpy is $H = (0.56 \pm 0.04)$ eV.

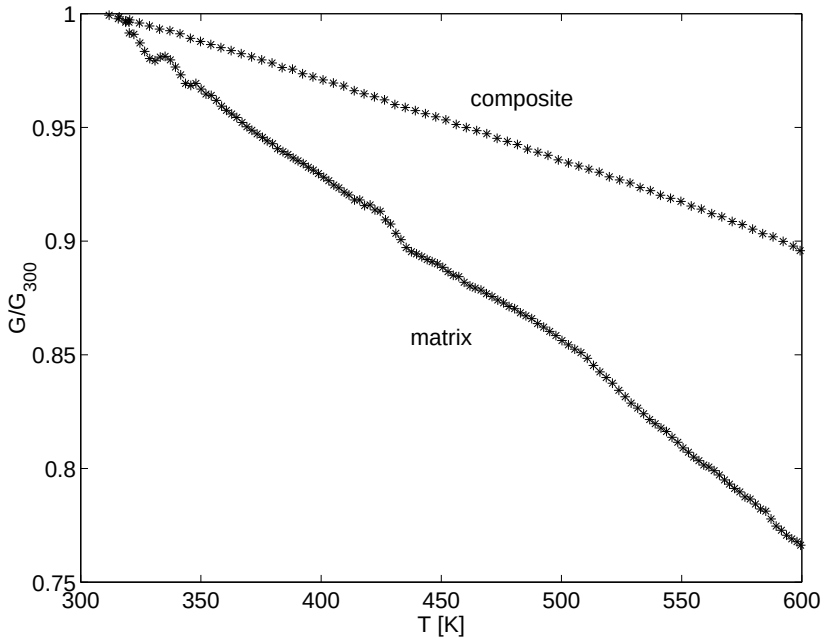

Figure 4.15: Relative shear modulus of the Al-3wt.%Mg matrix composite reinforced with Al-Cu-Fe particles and of the matrix itself, as measured in the inverted forced torsion pendulum.

4.5.2 Al_3Mg_2 matrix composite

The internal friction spectrum of the Al_3Mg_2 matrix composite material was found to exhibit also a simple exponential increase with temperature. It is interesting to note that the level of the internal friction is a little higher than the one obtained for the Al-3wt.%Mg composite. Internal friction measurements could not be performed on the Al_3Mg_2 matrix alone as it is too brittle. For comparison, the Al_3Mg_2 matrix composite reinforced with short Al_2O_3 fibres was tested. A relaxation peak was evidenced around 520 K (see Fig. 4.17) which is probably related to the matrix as nothing similar was observed in other composites reinforced with Al_2O_3 fibres.

This peak may be interpreted as a point defect relaxation peak due to the reordering into an ordered Al_3Mg_2 intermetallic alloy. A similar phenomenon was observed in a Ni_3Al alloy [Mourisco et al., 1997]. Assuming a Debye limit relaxation time of $\tau_0 = 10^{-13}$ s, the peak position corresponds to an activation enthalpy of $H = 1.35$ eV which is close to the aluminium and magnesium diffusion energies [Abedl-Rahman et al., 2002]. This peak is not present in the case of the Al-Cu-Fe reinforcement probably due to the

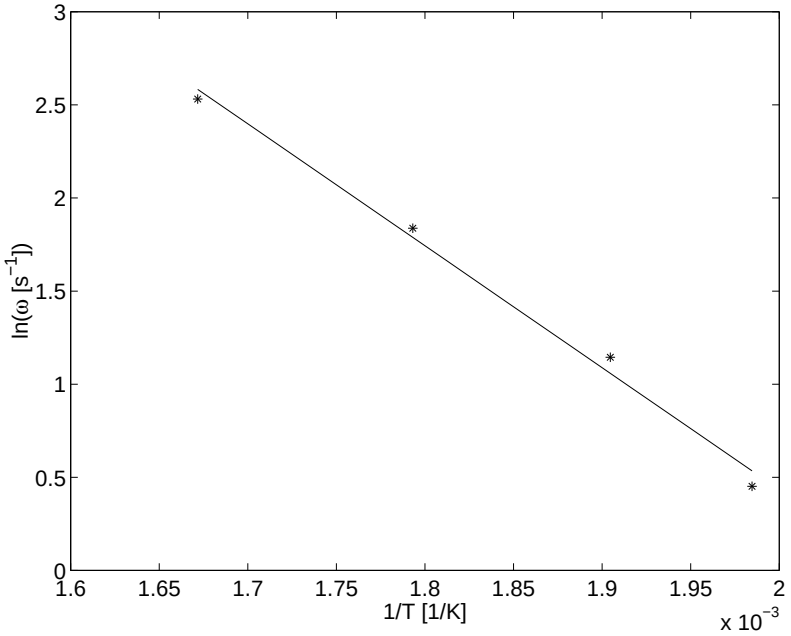

Figure 4.16: Arrhenius plot of the exponential background of the Al-3wt.%Mg matrix composite with Al-Cu-Fe particles for frequencies of 0.25, 0.5, 1, and 2 Hz. The determined activation enthalpy of the exponential background is $H = (0.56 \pm 0.04)$ eV.

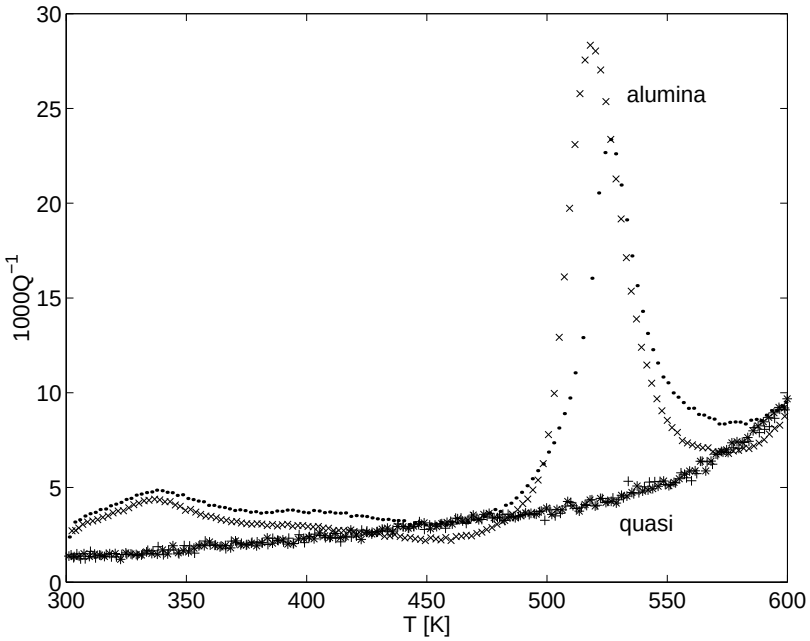

Figure 4.17: Isochronal internal friction spectra of the Al_3Mg_2 matrix composite reinforced either with Al-Cu-Fe particles or with Al_2O_3 fibres, as measured in the inverted forced torsion pendulum, 1 Hz, 0.5 K/min.

higher volume fraction of the reinforcement material and due to the phase transformation occurring around the quasicrystalline grains, which disturbs the composition of the intermetallic matrix around the grains.

The shear modulus of both composites behaves normally, i.e. it decreases with increasing temperature (see Fig. 4.18). In the case of alumina, the modulus defect corresponds well to the relaxation peak. As for quasicrystalline particles, a decrease of modulus is observed after one thermal cycle. This reflects a permanent damage of the material.

The shift of the high temperature exponential background with the applied frequency in isochronal measurements, as described by the equation (3.7), allows the drawing of an Arrhenius plot (see Fig. 4.19). The measured activation enthalpy is $H = (0.38 \pm 0.03)$ eV.

The high-temperature exponential background is also observed in the free-free vibrating bar apparatus. The equation (3.7) gives an apparent value of the activation enthalpy of $H' = (0.314 \pm 0.002)$ eV.

The apparent activation enthalpy can be corrected by considering a distribution of relaxation times using the equation (3.8). A broadening factor can be obtained

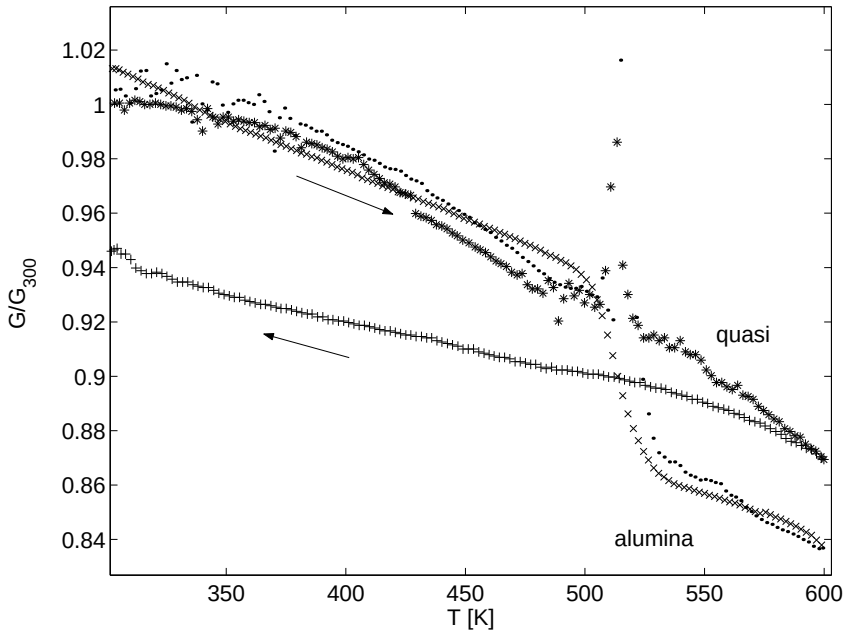

Figure 4.18: Relative shear modulus of the Al_3Mg_2 matrix composite reinforced either with Al-Cu-Fe particles or with Al_2O_3 fibres, as measured in the inverted forced torsion pendulum.

from the slope of an isothermal log-log plot (see Fig. 4.20). In the present case, the fit gives a broadening factor $1/\alpha = 3.7 \pm 0.3$. Thus, the true activation enthalpy is $H = (1.16 \pm 0.09)$ eV which is three times higher than the value given by the Arrhenius plot (0.38 eV). This difference can be explained by the fact that only the onset of the exponential background is observed in the forced pendulum (see Fig. 4.17). A change in the micro-structure of the sample with temperature cannot be excluded either, that is why in this case the Arrhenius method does not provide the correct activation enthalpy value.

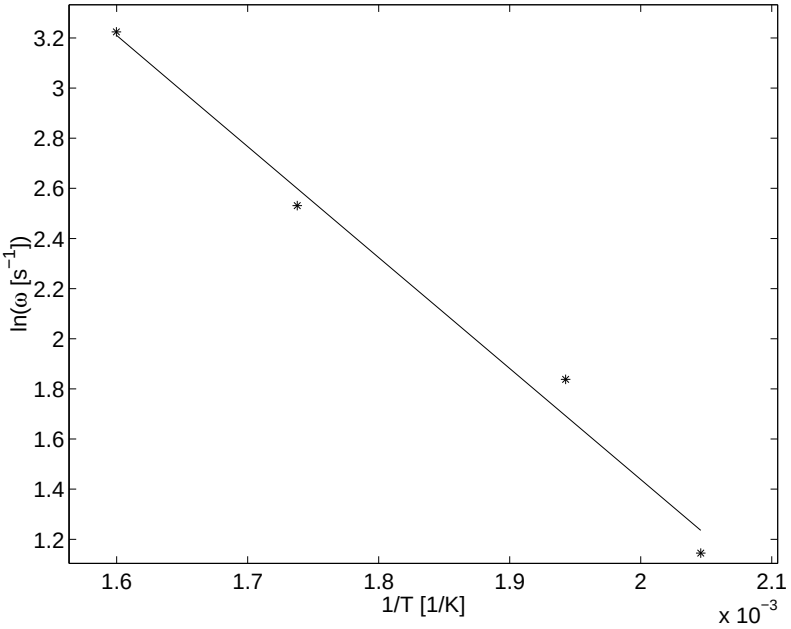

Figure 4.19: Arrhenius plot of the exponential background of the Al_3Mg_2 matrix composite reinforced with Al-Cu-Fe particles for frequencies of 0.5, 1, 2, and 4 Hz. The determined activation enthalpy of the exponential background is $H = (0.38 \pm 0.03)$ eV.

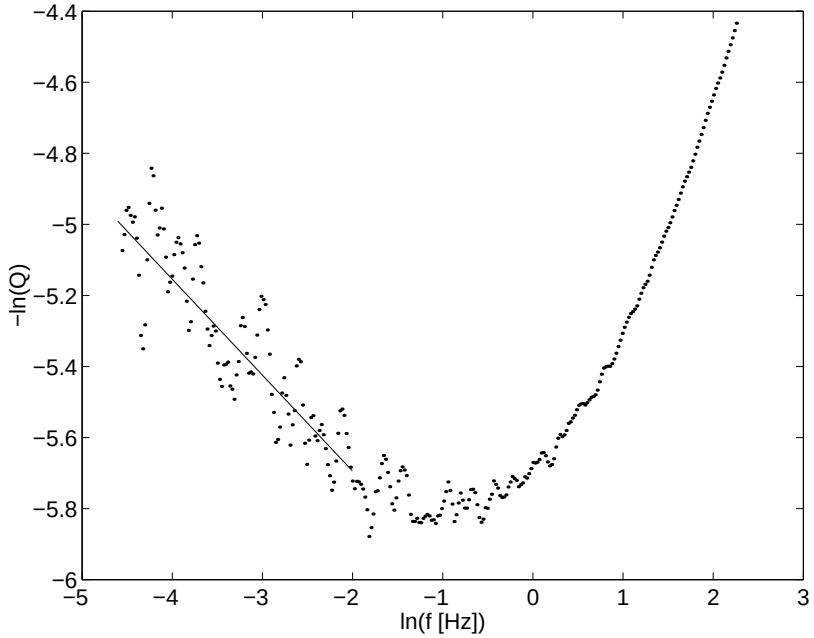

Figure 4.20: Fit giving the broadening factor $1/\alpha$ of the Al_3Mg_2 matrix composite; isothermal measurements at 500 K.

Chapitre 5

Discussion

In this chapter the shear modulus anomaly (see section 3.2.2) and the athermal maximum (see section 3.3.2) observed in internal friction measurements of the quasicrystalline coating will be treated in detail. They both seem to be related to the thermal stresses inside the coating and the substrate, that is why these stresses will be estimated, and then a model, explaining both the shear modulus anomaly and the athermal maximum, will be described.

Next, the high-temperature exponential background in the internal friction measurements of the coatings (see section 3.3.3) and also of the composites (see section 4.5) will be discussed and compared with the literature.

5.1 Thermal stresses and specimen bending

Thermal stresses are induced by the mismatch in thermal expansion coefficients of the coating α_1 and the substrate α_2, which may lead to a bending of a free specimen. In the following, we develop formulæ for the thermal stresses and the specimen bending for two cases. On the one hand, the specimen is free and can bend, which is the case e.g. in the free-free vibrating bar apparatus. Secondly, the sample is held straight, so that no bending is possible, which is the case e.g. in the inverted torsion pendulum.

5.1.1 Curved sample

The plate shaped specimen (see Fig. 5.1) is bended around the z-axis during a temperature change (see Fig. 5.2). If the radius of curvature R is much greater than the thickness of the plate $R \gg h_1 + h_2$, the bending strain can be calculated as the increase in length of

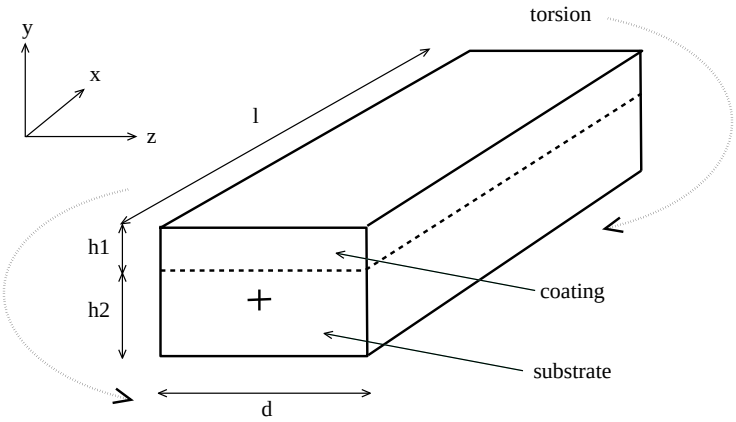

Figure 5.1: Plate shaped sample.

a small element divided by its initial length, which is equal to the length of the element at the neutral axis[1] (see Fig. 5.3)

$$\varepsilon_{bending} = \frac{\varphi\,(y+R) - \varphi\,R}{\varphi\,R} = \frac{y}{R}, \tag{5.1}$$

where y is the distance from the neutral axis. As the neutral axes may be at a different position within the coating and within the substrate, we choose the origin $y = 0$ at the interface between the coating and the substrate (see Fig. 5.2). Then the bending strain is expressed as

$$\varepsilon_{bending} = \frac{y-c}{R-c}, \tag{5.2}$$

where c is the y coordinate of the neutral axis. Since the curvature radius is much higher than the thickness $R \gg h_1 + h_2$ and thus $R \gg c$, we do not need to correct the denominator. However, we should still correct the numerator. We suppose that the curvature R is the same for the whole specimen and so the constant $-c/R$ from the bending term can be included into a constant term b. Assuming a small permanent deformation in the stress-free state with a curvature R_0 having the same sign as R, which was actually observed, we get the bending strain in the following form

$$\varepsilon_{bending} = y\left(\frac{1}{R} - \frac{1}{R_0}\right) + b. \tag{5.3}$$

The small permanent curvature radius of the specimen in the stress free state at room temperature was measured by means of a profile projector equipped with a digital

[1] neutral surface is a plane of zero bending strain; in a homogeneous material it is the middle of the cross-section

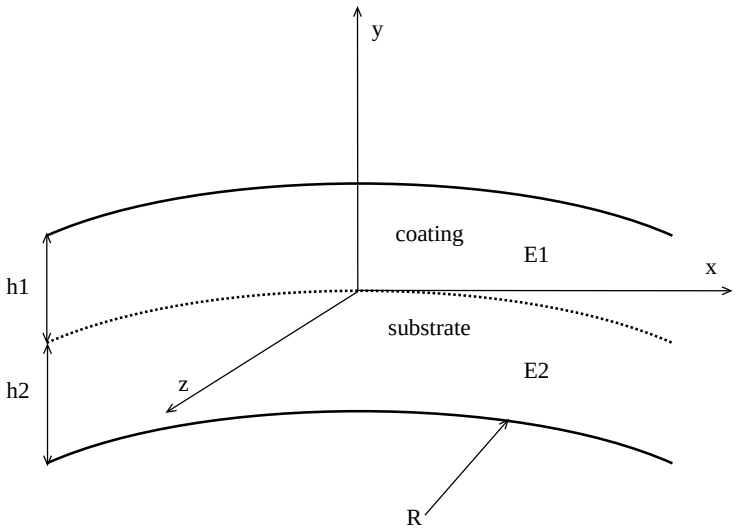

Figure 5.2: Curvature of the composite specimen.

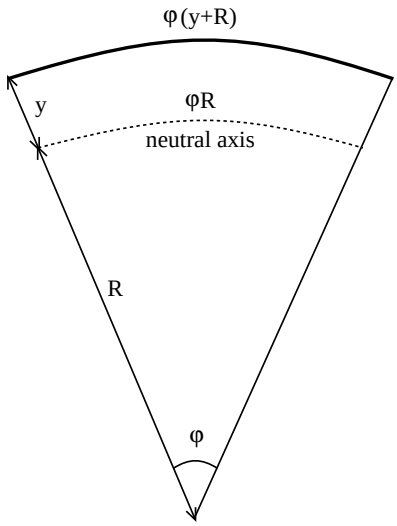

Figure 5.3: Bending strain.

microcalipers and it was found to be $R_0 = 0.5\,\mathrm{m}$ for the sample with dimensions $h_1 = 454\,\mu\mathrm{m}$, $h_2 = 593\,\mu\mathrm{m}$.

Then the total elastic strains of the coating ε_1 and the substrate ε_2 in the direction of the x-axis can be written in the form

$$\varepsilon_1 = \alpha_1 \Delta T + y\left(\frac{1}{R} - \frac{1}{R_0}\right) + b_1, \tag{5.4}$$

$$\varepsilon_2 = \alpha_2 \Delta T + y\left(\frac{1}{R} - \frac{1}{R_0}\right) + b_2, \tag{5.5}$$

where $\alpha\Delta T$ is the thermal strain, $y(1/R - 1/R_0)$ is the bending strain and b is a uniform strain induced by the second material and it also contains the $-c/R$ term. The reference temperature T_0 in the temperature difference $\Delta T = T - T_0$ is 300 K as we assume that all stresses are relaxed at room temperature.

The elastic stresses in the coating and the substrate can thus be expressed as follows[2]

$$\sigma_1 = E_1\left[y\left(\frac{1}{R} - \frac{1}{R_0}\right) + b_1\right], \tag{5.6}$$

$$\sigma_2 = E_2\left[y\left(\frac{1}{R} - \frac{1}{R_0}\right) + b_2\right], \tag{5.7}$$

where E_1 and E_2 are the Young's moduli and we suppose that only the elastic strains are involved. That is why the Von Mises criterion[3] [Hill, 1950] has to be verified subsequently by calculation.

As the bending takes place simultaneously also around the x-axis with the same strains, stresses and curvature radius, the Young's moduli E_1 and E_2 should be replaced by biaxial moduli

$$E_{biaxial} = \frac{E}{1-\nu}, \tag{5.8}$$

where ν is the corresponding Poisson's ratio. In order to simplify the notation, the biaxial moduli will also be denoted E_1 and E_2.

The deformation at the boundary $y = 0$ should be the same in both materials because the coating is firmly attached to the substrate

$$\varepsilon_1(0) = \varepsilon_2(0). \tag{5.9}$$

At any surface x =const. the sum of all forces should be zero

$$\Sigma F_i = d\int_0^{h_1} \sigma_1\, dy + d\int_{-h_2}^{0} \sigma_2\, dy = 0 \tag{5.10}$$

[2] the thermal expansion term $\alpha\Delta T$ does not appear here explicitly because the heating of a homogeneous material does not produce any stress, it only increases its dimensions

[3] maximal stresses in both the substrate and the coating are not higher than the yield stresses σ_{y1}, σ_{y2}

and the sum of all moments with respect to any axis[4] should be zero as well

$$\Sigma M_i = d \int_0^{h_1} \sigma_1 \, y \, dy + d \int_{-h_2}^{0} \sigma_2 \, y \, dy = 0. \tag{5.11}$$

By combining equations (2.43–5.11) we can calculate the curvature radius R and the stresses $\sigma\,(y)$

$$\frac{1}{R} = \frac{6 h_1 h_2 \,(h_1 + h_2)\, E_1 E_2 \,(\alpha_1 - \alpha_2)\, \Delta T}{4\, h_1\, h_2\, E_1\, E_2\, (h_1 + h_2)^2 + \left(h_1^2\, E_1 - h_2^2\, E_2\right)^2} + \frac{1}{R_0}, \tag{5.12}$$

$$\sigma_1\,(y) = -\frac{h_2 E_1 E_2\,(\alpha_1 - \alpha_2)\,\Delta T\left[h_1^3\, E_1 + h_2^3\, E_2 + 3\, h_1\, E_1\,(h_1 + h_2)\,(h_1 - 2\, y)\right]}{4\, h_1\, h_2\, E_1\, E_2\, (h_1 + h_2)^2 + \left(h_1^2\, E_1 - h_2^2\, E_2\right)^2}, \tag{5.13}$$

$$\sigma_2\,(y) = \frac{h_1 E_1 E_2\,(\alpha_1 - \alpha_2)\,\Delta T\left[h_1^3\, E_1 + h_2^3\, E_2 + 3\, h_2\, E_2\,(h_1 + h_2)\,(h_2 + 2\, y)\right]}{4\, h_1\, h_2\, E_1\, E_2\, (h_1 + h_2)^2 + \left(h_1^2\, E_1 - h_2^2\, E_2\right)^2}. \tag{5.14}$$

The inverted curvature radius $1/R$ increases almost linearly[5] with temperature as do also the stresses σ_1 and σ_2. Note that the stresses do not depend on the initial curvature radius R_0.

The resulting elastic strain at the interface $y = 0$ is

$$\varepsilon\,(0) = \Delta T \frac{\alpha_1\, h_1^4\, E_1^2 + \alpha_2\, h_2^4\, E_2^2 + h_1\, h_2\, E_1\, E_2\left[\alpha_1\, h_2\,(4\, h_2 + 3\, h_1) + \alpha_2\, h_1\,(4\, h_1 + 3\, h_2)\right]}{4\, h_1\, h_2\, E_1\, E_2\, (h_1 + h_2)^2 + \left(h_1^2\, E_1 - h_2^2\, E_2\right)^2}. \tag{5.15}$$

The whole calculation can be found in appendix A. The results are symmetric with respect to an exchange of the substrate and the coating[6], as $R \gg h_1 + h_2$ and the equations (5.4) and (5.5) are symmetric. For smaller curvature radii the equations are no more symmetric.

For the special case $h_1 \ll h_2$ the equations (5.12) and (5.13) can be reduced to Stoney's equation, which relates the stress σ_1 in a thin film deposited onto a substrate to the resulting curvature R [Stoney, 1909]

$$\sigma_1 = \frac{h_2^2\, E_2}{6\, h_1\, R}. \tag{5.16}$$

Nevertheless, as the thickness of our coating cannot be neglected with respect to the thickness of the substrate, we will use the general formulæ (5.12–5.15).

[4] as equation (5.10) holds, we can choose an arbitrary axis such as $y = 0$

[5] it is linear if the change of the moduli and the change of the dimensions with temperature are neglected

[6] exchanging all indices 1 and 2

5.1.2 Straight sample

Now the stresses in the simpler case of the sample being held straight are developed. The elastic strains of the coating and the substrate are given by equations (5.4) and (5.5) without the bending term

$$\varepsilon_1 = \alpha_1 \Delta T + b_1, \tag{5.17}$$
$$\varepsilon_2 = \alpha_2 \Delta T + b_2. \tag{5.18}$$

Thus, the stresses can be expressed similarly to equations (5.6) and (5.7)

$$\sigma_1 = E_1\, b_1, \tag{5.19}$$
$$\sigma_2 = E_2\, b_2, \tag{5.20}$$

where E_1 and E_2 are the biaxial elastic moduli of the coating and the substrate, respectively. The deformation at the interface $y = 0$ should be continuous as already described by equation (5.9). At any surface $x =$const. the sum of all forces should be zero as follows from equation (5.10). By combining equations (5.9) and (5.10) with equations (5.17–5.20) the stresses in the straight sample σ_1 and σ_2 can be calculated

$$\sigma_1 = \frac{-h_2\, E_1\, E_2\, (\alpha_1 - \alpha_2)\, \Delta T}{h_1\, E_1 + h_2\, E_2}, \tag{5.21}$$
$$\sigma_2 = \frac{h_1\, E_1\, E_2\, (\alpha_1 - \alpha_2)\, \Delta T}{h_1\, E_1 + h_2\, E_2}. \tag{5.22}$$

It is interesting to note that the stresses do not depend on y as in the case of the bended sample. On the other hand, they also increase linearly with increasing temperature as in the case of the bended sample.

The bending of the sample is constrained by applying an external moment M_z given by the sum of all moments (5.11)

$$M_z = \frac{1}{2} \frac{h_1\, h_2\, (h_1 + h_2)\, E_1\, E_2\, (\alpha_1 - \alpha_2)\, \Delta T}{h_1\, E_1 + h_2\, E_2}. \tag{5.23}$$

The strain of the whole composite is expressed as follows

$$\varepsilon = \varepsilon_1 = \varepsilon_2 = \frac{\alpha_1\, h_1\, E_1 + \alpha_2\, h_2\, E_2}{h_1\, E_1 + h_2\, E_2} \Delta T. \tag{5.24}$$

The detailed calculation can be found in appendix B. The thermal stresses either in the curved or the straight sample are reported in Fig. 5.4 as a function of the distance

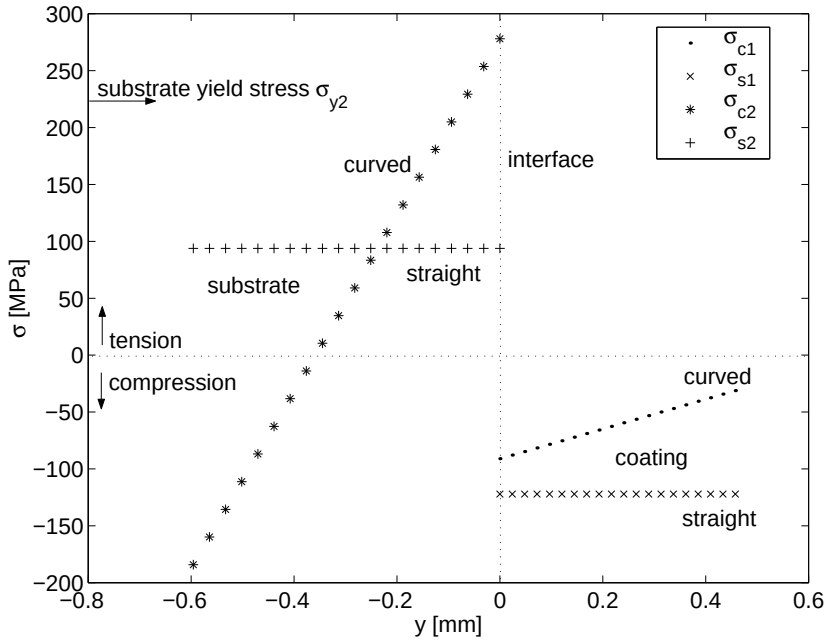

Figure 5.4: Calculated stresses in the coating and the substrate at 700 K for either the curved or the straight sample.

from the interface y for the temperature of 700 K and using the numerical values given in Tabs. 3.1 and 3.4. The negative stress sign refers to a compression and the positive sign to a tension.

The yield stress for the mild steel substrate, $\sigma_{y2} = 225$ MPa at 700 K, is reached near the interface in the case of the curved sample, while the stress in the quasicrystalline coating is always lower than its yield stress. The yield stress for icosahedral Al-Cu-Fe quasicrystals was measured to be $\sigma_{y1} = 800$ MPa in compression tests [Giacometti, 1999].

Reaching the substrate yield stress in the case of the curved sample implies a partial plasticity of a small part near the interface of the steel substrate and also a permanent bending deformation of the specimen, which was actually observed.

5.2 Young's modulus of composite

Although the following calculation is not directly related to the thermal stresses, the formulæ developed in the two previous sections can be also used with small changes to calculate the Young's modulus E_c of the whole composite in flexion from the known

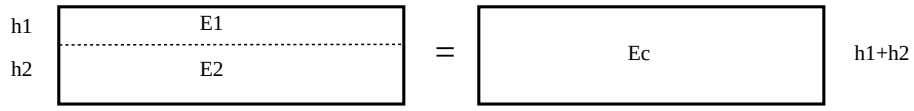

Figure 5.5: Calculation of the Young's modulus of the whole composite E_c knowing the Young's moduli of the coating and the substrate E_1 and E_2, respectively.

Young's moduli of the coating and the substrate E_1 and E_2 (see Fig. 5.5). This result has already been used in section 3.2.2 in order to find the Young's modulus of the coating from measurements of the substrate and the coating with the substrate.

The elastic strain equations (5.4) and (5.5) are used without the thermal expansion term, as the Young's modulus E_c is measured at room temperature, where the thermal stresses are already relaxed and thus $\Delta T = 0$. Then the elastic strains in the quasicrystalline coating and the mild steel substrate are given by

$$\varepsilon_1 = \frac{y}{R} + b_1, \tag{5.25}$$

$$\varepsilon_2 = \frac{y}{R} + b_2. \tag{5.26}$$

Consequently, the strong interface boundary condition (5.9) holds for $b_1 = b_2 = b$. The stresses are expressed by equations (5.6) and (5.7). The sum of all forces should be zero (5.10) but the sum of all moments with respect to $y = 0$ is $M \neq 0$, which is caused by the electrostatic force in the free-free vibrating bar apparatus

$$\Sigma M_i = d \int_0^{h_1} \sigma_1 \, y \, dy + d \int_{-h_2}^{0} \sigma_2 \, y \, dy = M. \tag{5.27}$$

From equations (5.27) and (5.10) the curvature radius R can be solved and it should equal to the radius R' for the whole composite being regarded as homogeneous (see Fig. 5.5), when it has only one component, the same thickness $h_2' = 0$, $h_1' = h_1 + h_2$, the Young's modulus $E_2' = E_c$ and it stands under the same torque $M' = M$. Accordingly

$$E_c = \frac{1}{(E_1 h_1 + E_2 h_2)(h_1 + h_2)^3} \left[E_1^2 h_1^4 + E_2^2 h_2^4 + E_1 E_2 \left(4h_1^3 h_2 + 4h_1 h_2^3 + 6h_1^2 h_2^2 \right) \right]. \tag{5.28}$$

The whole calculation can be found in appendix C. For the special case[7] $h_1 = h_2 = h/2$ and $E_1 = 0$ one gets $E_c = E_2/8$. This is quite surprising as for tension or compression

[7] no coating at all but we assume a double thickness of the sample

we would expect $E_2/2$, nevertheless, the result $E_2/8$ is in agreement with the formula (2.42) for calculating the Young's modulus from the resonance frequency f in a free-free vibrating bar apparatus [Vittoz et al., 1963] where for the whole composite[8] we get $E_c = E/8$ as well.

5.3 Shear modulus anomaly

A shear modulus anomaly was observed in the torsion pendulum, the modulus of the composite coating-substrate increases with increasing temperature (see Fig. 3.13) although the moduli of quasicrystals and steel are known to decrease with increasing temperature. However, the measured Young's modulus E of the composite behaves normally with increasing temperature in the free-free vibrating bar apparatus (see Fig. 3.12).

The shear modulus anomaly does not depend on the used torsion pendulum because the quantitatively same modulus anomaly was obtained in the forced torsion pendulum and in the free torsion pendulum as well.

The anomaly in the shear modulus G may be caused by a bowing of the specimen in the torsion pendulum, because of the different thermal expansions of the quasicrystalline coating and the steel substrate, which increases its torsional rigidity, or by a solid friction between cracked parts of the coating as the cracks tend to close with increasing temperature due to the thermally induced compression of the coating. These two possibilities will be discussed in detail now.

5.3.1 Specimen bending

Let's consider the sample as being homogeneous. Without bending, the external moment needed to maintain the torsion angle Θ of the rectangular specimen with dimensions $h \times d \times l$ is given by equations (2.10) and (2.16)

$$M = \frac{\beta\, G\, d\, h^3\, \Theta}{l}, \tag{5.29}$$

where G is the shear modulus of the sample and β is a numerical coefficient given in Tab. 2.2. The sample dimensions expand with the thermal expansion coefficients α_1 for h_1, α_2 for h_2, and α for d and l, where the average thermal expansion coefficient α is given by equation (5.15).

[8] $h_c = 2h$, $\rho_c = \rho/2$

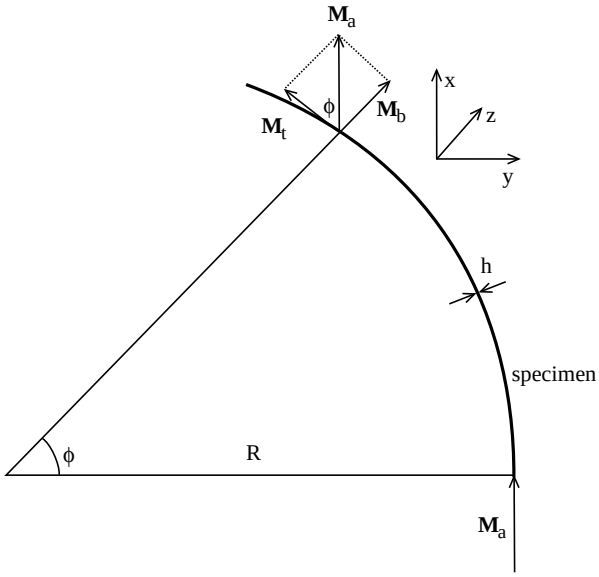

Figure 5.6: Torsion of the bended specimen, decomposition of the applied moment.

In the case of the bended specimen, when the radius of curvature R is much greater than the dimensions of cross-section of the specimen ($R \gg h$ and $R \gg d$), the applied moment M_a is decomposed into a torsion moment M_t and a bending moment M_b (see Fig. 5.6) [Ugural and Fenster, 1986]

$$M_t = M_a \cos\phi, \tag{5.30}$$

$$M_b = M_a \sin\phi. \tag{5.31}$$

The bending moment M_b can be neglected as it bends the specimen in the direction of z-axis, where the rigidity is high as $d > h$.

Next, the total angle of the twist in the bended case Θ' is calculated by integrating small torsion angles produced by a small element of length dl under torsional moment M_t

$$d\Theta' = \frac{M_t\, dl}{\beta\, G\, d\, h^3}. \tag{5.32}$$

They should also be projected in the direction of the x-axis (see Fig. 5.7)

$$d\Theta'_a = d\Theta' \cos\phi. \tag{5.33}$$

Then the total angle of the twist is calculated by integrating over the whole length l of the sample, i.e. over the angle $\phi = -l/2R \ldots l/2R$

$$\Theta' = \frac{2M_a\, R}{\beta\, G\, d\, h^3} \int_0^{\frac{l}{2R}} \cos^2\phi\, d\phi. \tag{5.34}$$

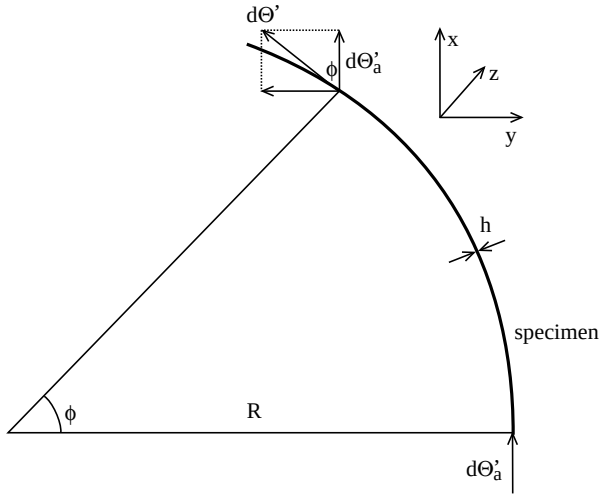

Figure 5.7: Torsion of the bended specimen, decomposition of the torsion angle.

Assuming $R \gg l$ the resulting apparent increase in torsional rigidity of the bended specimen G/G_{300} is

$$\frac{G}{G_{300}} = \left[1 - \left(\frac{l}{4R}\right)^2\right]^{-1}. \tag{5.35}$$

The specimen is also bended with the same curvature radius R in the cross-section, which can increase the torsional rigidity as well. We will approximate this effect by increasing the thickness of the sample to value h' (see Fig. 5.8) which certainly has a greater rigidity than the bended sample. Then the increased thickness h' equals to

$$h' = h + R - \sqrt{R^2 - \frac{d^2}{4}}. \tag{5.36}$$

Assuming $R \gg d$ this equation simplifies to

$$h' = h + \frac{d^2}{8R}. \tag{5.37}$$

Consequently, the total apparent increase of the torsional rigidity of the sample due to the specimen bi-directional bending and the thermal expansion of the specimen dimensions[9] should not be greater than[10]

$$\frac{G}{G_{300}} = \left(1 + \frac{d^2}{8R\,h}\right)^3 \left[1 - \left(\frac{l}{4R}\right)^2\right]^{-1} \frac{h^3}{h_0^3}, \tag{5.38}$$

[9] the expansions of l and d eliminate each other

[10] the small decrease of coefficient β with increased thickness of the sample h' is also neglected

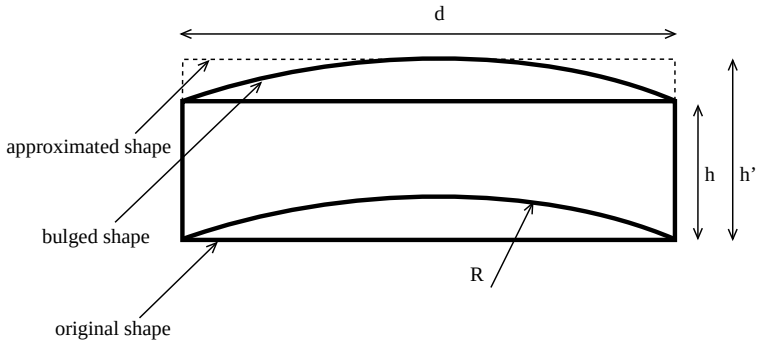

Figure 5.8: Bulging of the cross-section of the sample, the bended sample is approximated by rectangular cross-section $d \times h'$.

where h_0 is the thickness at room temperature T_0 and h is the thickness at temperature T.

The calculated values are presented in Fig. 5.9 and they are 3.4–5.9 times smaller than the measured values, moreover, they do not show the observed dependency on different thicknesses of the coating, i.e. even multiplying the equation (5.38) with a constant cannot reproduce the measured values for all thicknesses. Thus, the shear modulus anomaly cannot be caused by the change of geometry of the sample induced by the thermal expansion.

5.3.2 Solid friction

The quasicrystalline coating contains a network of cracks (see Fig. 3.5) which are responsible for breaking up the coating into pieces as illustrated in Fig. 5.10. The two segments of the coating separated by a crack are pressed against each other by the thermal stress σ_1 (see Fig. 5.10) which increases with increasing temperature. The cracks width w is also slowly decreasing with increasing temperature[11], however, a simple calculation shows that a temperature needed to the total closure of all cracks is several thousands kelvins.

Then the shear deformation in the inverted torsion pendulum causes a sliding accompanied with friction of the two segments in the direction of $z-$axis while the flexion in the free-free vibrating bar apparatus does not provoke any friction, it only slightly opens and closes the cracks.

[11] i.e. cracks closing

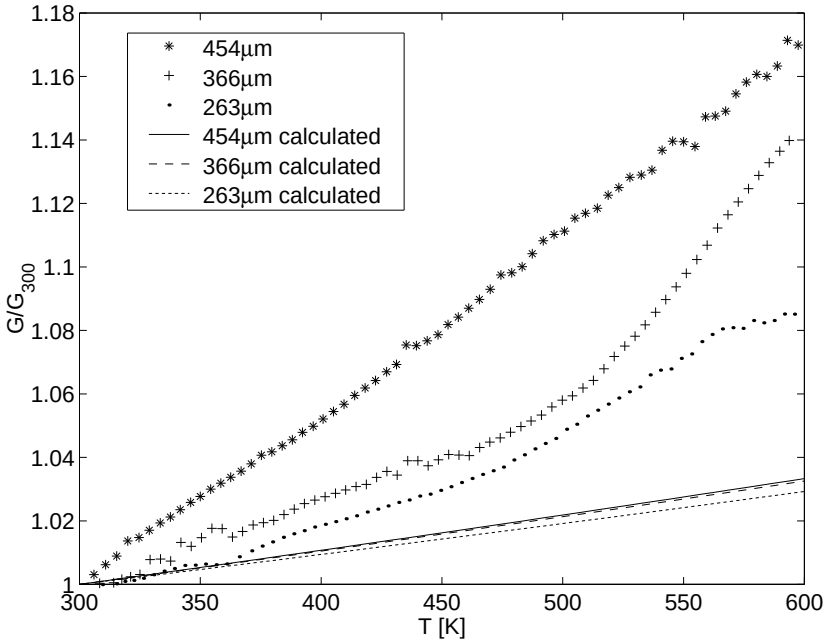

Figure 5.9: Shear modulus anomaly due to the specimen bowing; measured values for different thicknesses of the coating compared with calculated values.

This friction mechanism can be represented as a non-localised solid friction device in a rheological model (see Fig. 5.11). The first spring with modulus G_i corresponds to the elastic shear modulus of the composite G without cracks while the second spring with modulus G_{ii} corresponds to the elastic shear modulus of the substrate G_2 in the area of the crack. If w is the total width of the cracks in the whole length l of the sample then the spring moduli are given by

$$G_i = \frac{l}{l-w} G, \tag{5.39}$$

$$G_{ii} = \frac{l}{w} G_2. \tag{5.40}$$

$$\tag{5.41}$$

The stresses σ_i and σ_{ii} satisfy the equation

$$\sigma_i \, h_1 + \sigma_{ii} \, h_2 = \sigma \, h. \tag{5.42}$$

The critical stress σ_c of the non-localised solid friction device is proportional to the friction force between the two segments and consequently

$$\sigma_c = \mu \, S_c \, \frac{1}{d \, h_1^2} \int_0^{h_1} \sigma_1 \, dy, \tag{5.43}$$

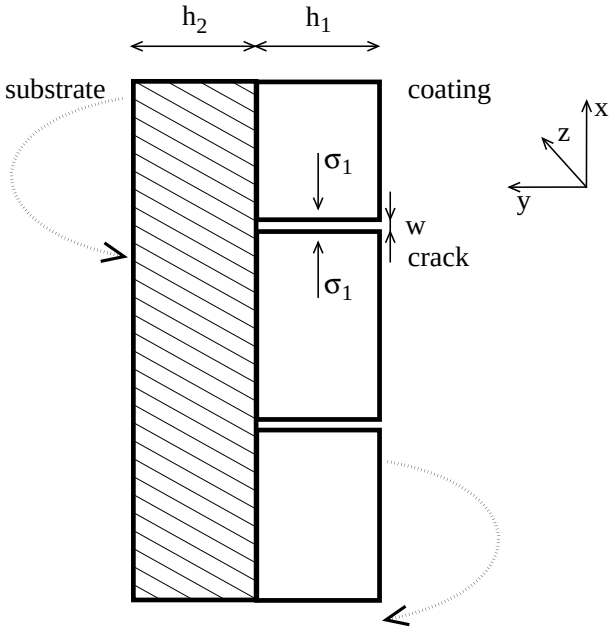

Figure 5.10: Solid friction in the cracked quasicrystalline coating.

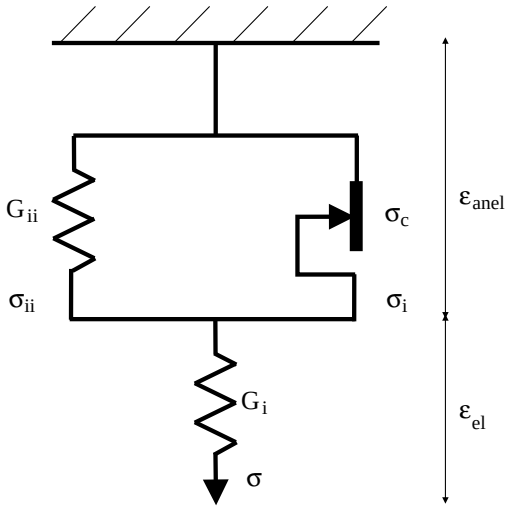

Figure 5.11: Rheological model with a non-localised solid friction device.

where the integration gives the average stress between the segments, μ is the friction coefficient which has to be derived from experimental results and S_c is the contact surface between the two segments. It is naturally limited by

$$0 < S_c \leq d\, h_1. \tag{5.44}$$

Two simple cases have been studied. Either the contact surface S_c does not depend on the thickness of the coating h_1, which can be explained by the wedge shape of the cracks[12], or S_c depends linearly on the thickness of the coating h_1, which can be explained by parallel faces of the cracks.

The first model with constant contact surface S_c predicts a higher modulus anomaly for smaller thicknesses of the coating contrary to the observations. That is why the second model will be developed. Then the contact surface is given by

$$S_c = c\, d\, h_1, \tag{5.45}$$

where the constant c represents the fraction of the contact surface with respect to the whole cross-section of the coating. It is naturally limited by $0 < c \leq 1$.

The behaviour of the rheological model in Fig. 5.11 is described by equations

$$\varepsilon = \begin{cases} \frac{\sigma}{G_i} + \frac{h}{h_2}\frac{\sigma \pm \sigma_c'}{G_{ii}} & \text{if} \quad \max(\sigma) \geq \sigma_c', \\ \frac{\sigma}{G_i} & \text{if} \quad \max(\sigma) < \sigma_c', \end{cases} \tag{5.46}$$

where $\sigma_c' = \sigma_c\, h_1/h$ and the sign in the term $\sigma \pm \sigma_c'$ is opposite to the sign of $\dot{\varepsilon}$. Applying a cyclic stress and using equation (1.16) one gets the strain amplitude ε_0

$$\varepsilon_0 = \begin{cases} \frac{\sigma_0}{G_i} + \frac{h}{h_2}\frac{\sigma_0 - \sigma_c'}{G_{ii}} & \text{if} \quad \sigma_0 \geq \sigma_c', \\ \frac{\sigma_0}{G_i} & \text{if} \quad \sigma_0 < \sigma_c', \end{cases} \tag{5.47}$$

where σ_0 is the stress amplitude. The critical stress σ_c' is zero at room temperature and then it increases with increasing temperature as does the stress in the coating σ_1. When $\sigma_0 \geq \sigma_c'$ the shear modulus anomaly can be expressed as

$$\frac{G}{G_{300}} = \left(1 - \frac{\sigma_c'}{\sigma_0}\frac{G_i\, h}{G_i\, h + G_{ii}\, h_2}\right)^{-1}. \tag{5.48}$$

Two cases can be distinguished, either the specimen is held straight and the stress in the quasicrystalline coating σ_1 is given by equation (5.21) or the specimen is curved and

[12] then the contact surface is close to the interface

the stress in the quasicrystalline coating σ_1 is given by equation (5.13). In both cases the thermal expansion term and the cross-section bulging term from equation (5.38) have to be considered, for the latter even the bending term can be included.

$$\frac{G_{straight}}{G_{300}} = \left(1 - \frac{\sigma_c'}{\sigma_0}\frac{G_i\,h}{G_i\,h + G_{ii}\,h_2}\right)^{-1}\left(1 + \frac{d^2}{8R\,h}\right)^3\frac{h^3}{h_0^3}, \tag{5.49}$$

$$\frac{G_{curved}}{G_{300}} = \left(1 - \frac{\sigma_c'}{\sigma_0}\frac{G_i\,h}{G_i\,h + G_{ii}\,h_2}\right)^{-1}\left(1 + \frac{d^2}{8R\,h}\right)^3\left[1 - \left(\frac{l}{4R}\right)^2\right]^{-1}\frac{h^3}{h_0^3}. \tag{5.50}$$

The calculated relative shear modulus is compared to the measured one in Figs. 5.12 and 5.13. The agreement is very good in the case of the straight sample. In the case of the curved sample the ratios between calculated moduli for different thicknesses of the coating are too small. The ratio between the modulus anomaly for the thickest and the thinnest sample is 1.25 while it is 1.71 in the straight case and the measured value is 2. This represents an argument supporting the idea that the sample is held straight in the inverted torsion pendulum rather than being free and curved.

It can be concluded that the measured shear modulus anomaly is an artifact caused by the solid friction between cracked pieces of the quasicrystalline coating which are pressed against each other by the thermal stresses. Obviously, this solid friction mechanism should influence also the mechanical loss measurements, which corresponds well to the observed athermal internal friction maximum as will be shown in the next section.

5.4 Athermal maximum

The internal friction maximum is observed around 600 K in the case of coatings (see Figs. 3.16 and 3.20) and it is not thermally activated since it is not present in isothermal measurements (see Fig. 3.17).

This athermal behaviour can be explained by the already presented solid friction rheological model (see Fig. 5.11). The internal friction can be calculated from equation (1.15) and it equals to

$$Q^{-1} = \begin{cases} \frac{4}{\pi}\frac{h}{h_2}\frac{G_i}{G_{ii}}\left(1 - \frac{\sigma_c'}{\sigma_0}\right)\frac{\sigma_c'}{\sigma_0} & \text{if} \quad \sigma_0 \geq \sigma_c', \\ 0 & \text{if} \quad \sigma_0 < \sigma_c'. \end{cases} \tag{5.51}$$

In order to confirm the validity of the solid friction model, the measurements with different thicknesses of the coating (see Figs. 3.16 and 3.20) are compared with the calculated values (see Figs. 5.14 and 5.15). The known amplitude of the applied shear

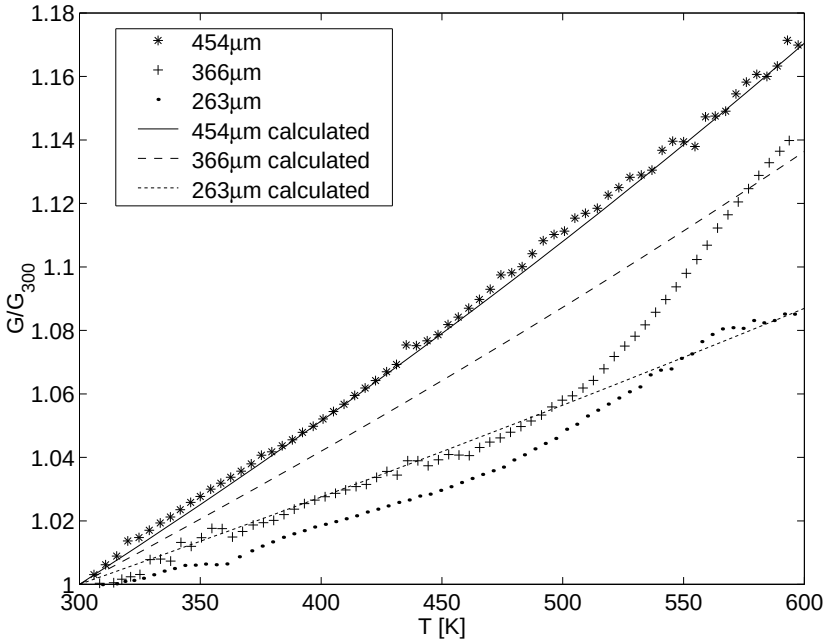

Figure 5.12: Shear modulus anomaly due to the solid friction in the cracked coating; measured values for different thicknesses of the coating compared with calculated values assuming straight sample; $w = 4\,\mathrm{mm}$; $c.\mu/\sigma_0$=52 GPa^{-1}.

stress $\sigma_0 = 1.7\,\mathrm{MPa}$ allows to calculate the friction coefficient μ multiplied by the unknown contact surface coefficient c. It equals to $c.\mu = 0.09$ and $c.\mu = 0.15$ in the case of the straight and curved sample, respectively. Comparing these values with measured friction coefficients $\mu = 0.216$–0.217 and $\mu = 0.305$–0.344 for Al-Cu-Fe-Cr alloy as measured with diamond and steel indenter tip, respectively [Dubois et al., 1991], leads to an acceptable range of 0.28–0.69 for the contact surface coefficient c.

The calculated maxima correspond well to the measured values, only they are shifted to the low temperatures. This may be caused by a transient damping as the measurements were carried out at 0.5 K/min or by the too simple model, as e.g. an introduction of a static friction 1.5 times greater than the kinetic friction leads to correct positions of the maxima.

The substantial decrease of internal friction as a result of a 40-hour long thermal cycling between 450 K and 570 K (see Fig. 3.19) can be explained by a slow relaxation of the thermal stress σ_1 in the quasicrystalline coating or by blocking of some cracks as a result of evolution of the friction surfaces towards the equilibrium position.

Moreover, the calculated maxima assuming the curved sample exhibit the observed relative shift, when the maximum for the thinner coating appears at lower temperature

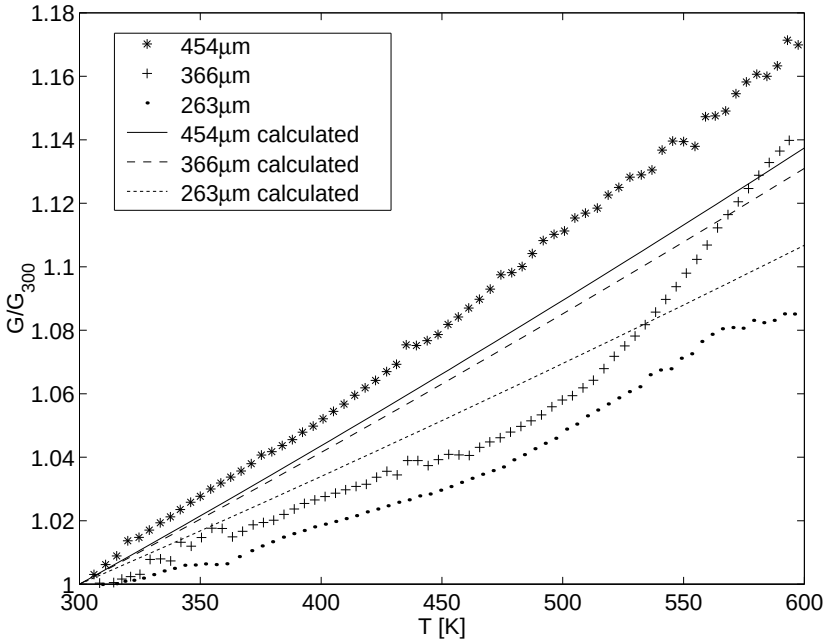

Figure 5.13: Shear modulus anomaly due to the solid friction in the cracked coating; measured values for different thicknesses of the coating compared with calculated values assuming bended sample; $w = 4\,\mathrm{mm}$; $c.\mu/\sigma_0$=91 GPa^{-1}.

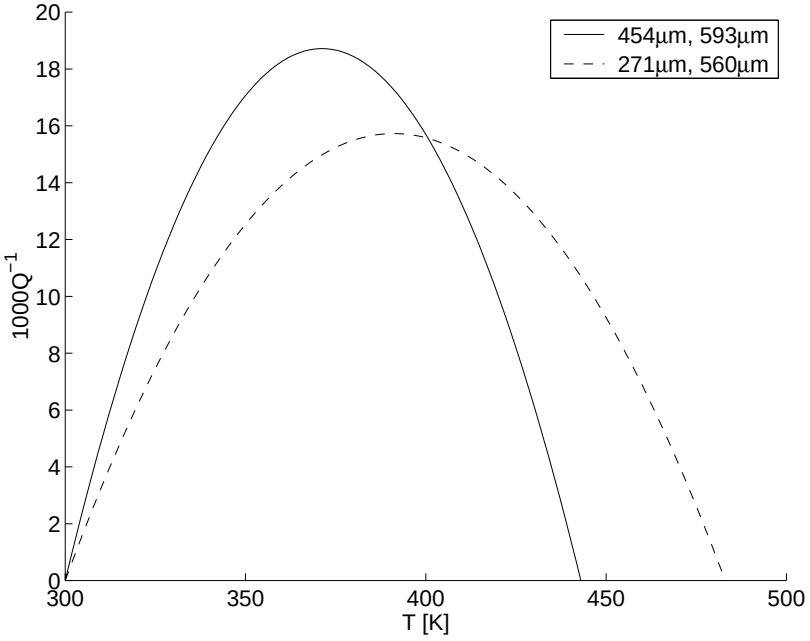

Figure 5.14: Calculated internal friction due to the solid friction in the cracked coating assuming straight sample; $w = 4\,\mathrm{mm}$; $c.\mu/\sigma_0$=52 GPa^{-1}.

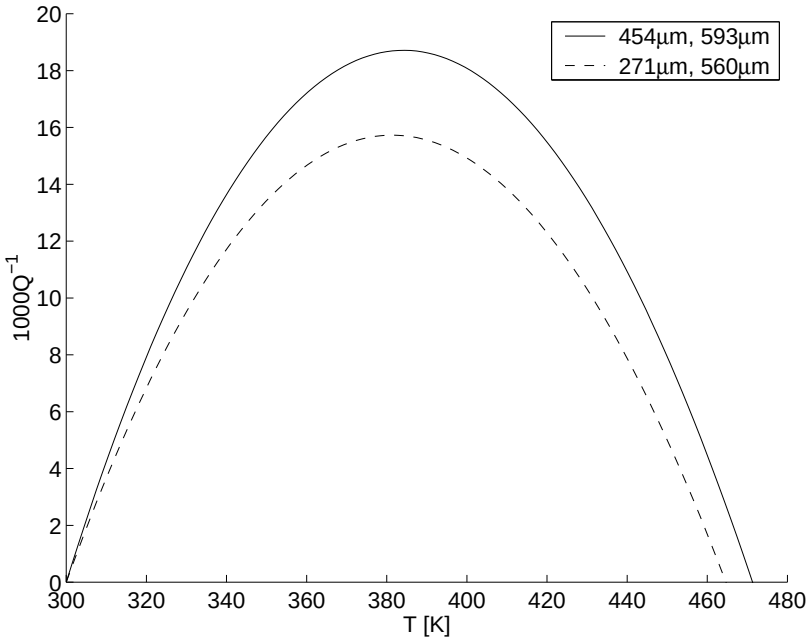

Figure 5.15: Calculated internal friction due to the solid friction in the cracked coating; assuming curved sample; $w = 4\,\text{mm}$; $c.\mu/\sigma_0$=91 GPa^{-1}.

than the maximum for the thicker coating. This conclusion is in contrast to the one of the shear modulus anomaly. In reality the sample is probably partially curved and that is why another more complex model has to be developed.

Nevertheless, the athermal maximum is very well explained by the solid friction between the cracked parts of the quasicrystalline coating and is closely related to the shear modulus anomaly measured in torsion. It is interesting to note that neither this maximum (see Fig. 3.23) nor the modulus anomaly (see Fig. 3.12) are present in flexion measurements in the free-free vibrating bar apparatus.

5.5 Exponential background

5.5.1 Coatings

The observed high-temperature exponential backgrounds in the case of coatings (see Figs. 3.21 and 3.25) are interpreted as the onset of the brittle-to-ductile transition in the quasicrystalline coating. The measured values of the activation enthalpies for two different thicknesses of the coating are in the range of (1.76–2.00) eV. They are close to

the value of 2 eV at 800 K, which was deduced from compression tests performed on icosahedral Al-Cu-Fe bulk material [Giacometti, 1999] and which certainly corresponds to the thermally activated brittle-to-ductile transition.

Surprisingly, a very similar phenomenon was observed in three other quasicrystalline materials. Furthermore, they are the only three internal friction measurements on quasicrystals, so this exponential background may be intrinsic to quasicrystals and can be probably related to the brittle-to-ductile transition.

A high-temperature exponential background around 600 K at 500 Hz was evidenced in quasicrystalline $Zr_{69.5}Cu_{12}Ni_{11}Al_{7.5}$ [Sinning et al., 2002] where it was interpreted as a sign of enhanced dynamics in the quasicrystalline phase itself.

The high-temperature exponential background for decagonal Al-Ni-Co quasicrystals (see Fig. 1.16) with an activation enthalpy of 2.3 eV appears around 1000 K for a frequency of 2 kHz. It was assigned to a diffusion-controlled viscoelastic relaxation [Damson et al., 2000b].

Finally, the observed exponential background can be related to the onset of the relaxation peak B found in icosahedral Al-Pd-Mn (see Fig. 1.14 and 5.16) with an activation enthalpy of 4.0 eV, broadening factor of 3–4 and an attempt frequency of $\tau_0^{-1} = 3 \times 10^{24}\,\mathrm{s}^{-1}$. This peak shows a non-linear Arrhenius behaviour for higher frequencies ($f > 1$ kHz, see Fig. 5.16) and it was attributed to a relaxation process in which the dislocation movement is controlled by the creation and movement of phason defects [Damson et al., 2000a,b].

The peak B may be also interpreted as a brittle-to-ductile transition. This transition is represented in quasicrystals by an extension of the disordered region (see Fig. 1.12) where the dislocations can move more easily, so this effect causes a decrease of the limit relaxation time τ_0, i.e. the Arrhenius plot shows a behaviour identical to Fig. 5.16 around the transition temperature. Moreover, the observed broadening factor of the B peak is close to the values of 4.25–4.45 found for the exponential background of the Al-Cu-Fe-Cr coatings. The difference in activation enthalpies can be probably explained by the different composition of Al-Pd-Mn and Al-Cu-Fe-Cr quasicrystals.

5.5.2 Composites

In the case of metal matrix composites reinforced with Al-Cu-Fe particles, the observed high-temperature exponential backgrounds (see Figs. 4.14 and 4.17 for the Al-Mg3% and Al_3Mg_2 matrix, respectively) have activation enthalpies of 0.56 eV and 1.16 eV. They

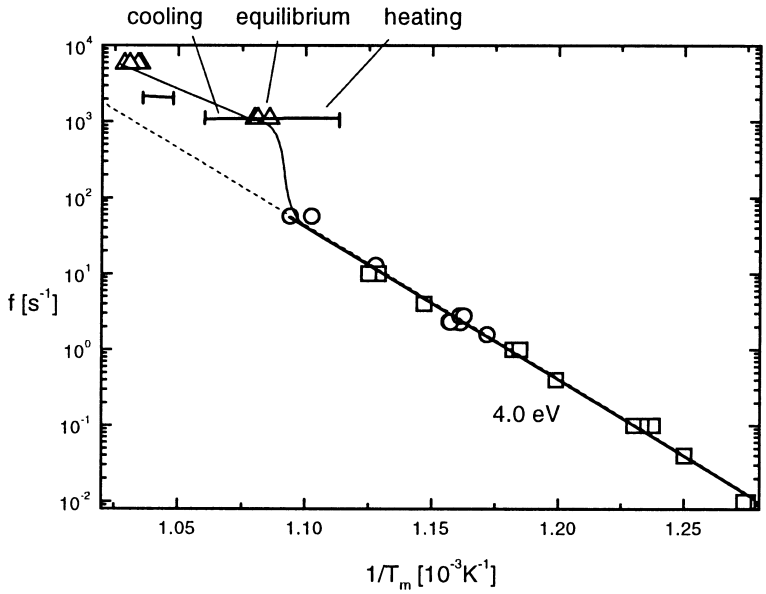

Figure 5.16: Arrhenius plot of maximum B in i-Al-Pd-Mn, brittle-to-ductile transition temperature 900 K [Damson et al., 2000b].

are probably caused by the dislocation motion in the matrix, nevertheless, the relation to the quasicrystalline reinforcement can be neither excluded nor confirmed with certainty.

The contribution of the interfaces is not known. In order to determine the origin of the mechanical loss, measurements with different amounts of quasicrystalline particles, as in the case of coatings, should be performed. This was not possible because the used fabrication technique does not allow an easy control of the volume fraction of the Al-Cu-Fe particles.

5.6 Proposition for further research

In the case of the quasicrystalline coatings, samples produced by different techniques and thus containing different amounts of cracks and with different substrates should be used and the precise measurements of the expansion coefficients and friction coefficients should be carried out to confirm the validity of the proposed solid friction model.

In order to verify the hypothesis about the brittle-to-ductile transition, internal friction measurements of the bulk quasicrystalline material at high temperature together with microstructure analysis and deformation tests are needed.

It would be interesting to process metal matrix composites by powder-metallurgy

and sintering techniques. The applied pressure in these cases would be higher than in the case of gas pressure infiltration, which may allow to decrease the processing temperature and consequently to avoid any phase transformation of the quasicrystalline reinforcement material. Furthermore, it will permit a better control of the volume fraction of quasicrystalline particles.

Chapitre 6

Conclusion

Since bulk quasicrystals are very brittle at room temperature, mechanical spectroscopy measurements were performed on two types of materials: decagonal quasicrystalline Al-Cu-Fe-Cr coatings deposited on a mild steel substrate and aluminium or magnesium matrix composites reinforced with icosahedral quasicrystalline Al-Cu-Fe particles.

In the case of the coatings, the origin of the mechanical loss was determined. Internal friction spectra of the substrate with three different thicknesses of the coating indicate that the internal friction of such composites is mostly caused by the quasicrystalline coating and that the contributions of the steel substrate and of the interface are small.

Thermal stresses provoked by the mismatch in thermal expansions between the substrate and the coating cause a compression of the coating, a tension of the substrate and may lead to a bending of the specimen at temperatures above room temperature. The thermal stresses and the specimen bending were estimated numerically.

A shear modulus anomaly was observed and interpreted as due to the solid friction between cracked segments of the quasicrystalline coating induced by the thermal stresses. This phenomenon can also explain the broad athermal maximum, which was found to occur in isochronal internal friction measurements. A quantitative model successfully reproducing the observed behaviour was developed.

Finally, the reversible high-temperature exponential background was interpreted as due to the onset of the brittle-to-ductile transition, which may be associated with a dislocation motion controlled by collective phason flips in the quasicrystalline coating. The measured activation enthalpy fits well the value that was deduced from compression tests performed on icosahedral Al-Cu-Fe bulk material.

In the case of the composites, optimal processing conditions were found, which restrict the phase transformation of the quasicrystalline particles and which provide good

mechanical properties of the samples.

The internal friction spectra of the composites also show a high-temperature exponential background, while measurements of the matrix alone or of the matrix with Al_2O_3 short fibres exhibit a different behaviour. The difference can be explained by a partial phase transformation of the matrix due to the presence of the quasicrystalline particles.

The exponential background is probably caused by dislocation motion in the matrix, however, the effect of the quasicrystalline reinforcement can be neither excluded nor confirmed with certainty. In order to determine the origin of the mechanical loss, measurements with different amounts of quasicrystalline particles should be performed.

Appendix A

Stress calculation in curved sample

The source code is meant for MAPLE[1] version 6.01. Listing of stress-curved.mws:

```
> restart;

> epsilon1:=b1+y*(1/R-1/R0);
```

$$\varepsilon 1 := b1 + y\,(\frac{1}{R} - \frac{1}{R0})$$

```
> epsilon2:=b2+y*(1/R-1/R0);
> % elastic strains
```

$$\varepsilon 2 := b2 + y\,(\frac{1}{R} - \frac{1}{R0})$$

```
> I1:=int(epsilon2*E2,y=-h2..0)+int(epsilon1*E1,y=0..h1);
> % sum of all forces = 0
```

$$I1 := -\frac{1}{2}\,(\frac{1}{R} - \frac{1}{R0})\,E2\,h2^2 + b2\,E2\,h2 + \frac{1}{2}\,(\frac{1}{R} - \frac{1}{R0})\,E1\,h1^2 + b1\,E1\,h1$$

```
> I2:=int(epsilon2*E2*y,y=-h2..0)+int(epsilon1*E1*y,y=0..h1);
> % sum of all moments = 0
```

$$I2 := \frac{1}{3}\,(\frac{1}{R} - \frac{1}{R0})\,E2\,h2^3 - \frac{1}{2}\,b2\,E2\,h2^2 + \frac{1}{3}\,(\frac{1}{R} - \frac{1}{R0})\,E1\,h1^3 + \frac{1}{2}\,b1\,E1\,h1^2$$

```
> I3:=b1-b2+da;
> % boundary condition; da=dT(alpha1-alpha2)
```

$$I3 := b1 - b2 + da$$

```
> solution:=simplify(solve({I1,I2,I3},{R,b1,b2}));
> % solution of I1, I2 and I3
```

[1] http://www.maplesoft.com

$$solution := \{R = R0\,\%1/(E2^2\,h2^4 + 6\,E2\,h2^2\,E1\,h1^2 + 6\,E2\,h2^2\,E1\,h1\,R0\,da + E1^2\,h1^4 + 4\,E2\,h2^3\,E1\,h1 + 4\,E1\,h1^3\,E2\,h2 + 6\,E1\,h1^2\,R0\,da\,E2\,h2),$$

$$b2 = \frac{(4\,E2\,h2^3 + 3\,E2\,h1\,h2^2 + E1\,h1^3)\,da\,h1\,E1}{\%1},$$

$$b1 = -\frac{da\,E2\,h2\,(3\,h2\,E1\,h1^2 + E2\,h2^3 + 4\,E1\,h1^3)}{\%1}\}$$

$$\%1 := E2^2\,h2^4 + 6\,E2\,h2^2\,E1\,h1^2 + E1^2\,h1^4 + 4\,E2\,h2^3\,E1\,h1 + 4\,E1\,h1^3\,E2\,h2$$

```
> simplify(subs(solution,{sigma1=E1*epsilon1,sigma2=E2*epsilon2}));
> %elastic stresses
```

$$\{\sigma1 = \frac{E1\,da\,E2\,h2\,(-3\,h2\,E1\,h1^2 - E2\,h2^3 - 4\,E1\,h1^3 + 6\,y\,E1\,h1\,h2 + 6\,y\,E1\,h1^2)}{E2^2\,h2^4 + 6\,E2\,h2^2\,E1\,h1^2 + E1^2\,h1^4 + 4\,E2\,h2^3\,E1\,h1 + 4\,E1\,h1^3\,E2\,h2},$$

$$\sigma2 = \frac{E2\,E1\,h1\,da\,(4\,E2\,h2^3 + 3\,E2\,h1\,h2^2 + E1\,h1^3 + 6\,y\,E2\,h2^2 + 6\,y\,E2\,h2\,h1)}{E2^2\,h2^4 + 6\,E2\,h2^2\,E1\,h1^2 + E1^2\,h1^4 + 4\,E2\,h2^3\,E1\,h1 + 4\,E1\,h1^3\,E2\,h2}\}$$

```
> epsilon0:=simplify(subs(da=dt*(alpha1-alpha2),subs(solution,b1+dt*alp
> ha1)));
> %elastic strain of interface y=0
```

$$\varepsilon0 := dt(3\,E2\,h2^2\,\alpha1\,E1\,h1^2 + 3\,E2\,h2^2\,\alpha2\,E1\,h1^2 + E2^2\,h2^4\,\alpha2 + 4\,E2\,h2\,\alpha2\,E1\,h1^3 + \alpha1\,E1^2\,h1^4 + 4\,\alpha1\,E2\,h2^3\,E1\,h1)/(E2^2\,h2^4 + 6\,E2\,h2^2\,E1\,h1^2 + E1^2\,h1^4 + 4\,E2\,h2^3\,E1\,h1 + 4\,E1\,h1^3\,E2\,h2)$$

Appendix B

Stress calculation in straight sample

The source code is meant for MAPLE[1] version 6.01. Listing of stress-straight.mws:

```
> restart;
> epsilon1:=b1;
```

$$\varepsilon 1 := b1$$

```
> epsilon2:=b2;
> % elastic strains
```

$$\varepsilon 2 := b2$$

```
> I1:=int(epsilon2*E2,y=-h2..0)+int(epsilon1*E1,y=0..h1);
> % sum of all forces = 0
```

$$I1 := b2\,E2\,h2 + b1\,E1\,h1$$

```
> I2:=int(epsilon2*E2*y,y=-h2..0)+int(epsilon1*E1*y,y=0..h1);
> % sum of all moments = M
```

$$I2 := -\frac{1}{2}\,b2\,E2\,h2^2 + \frac{1}{2}\,b1\,E1\,h1^2$$

```
> I3:=b1-b2+da;
> % boundary condition; da=dT(alpha1-alpha2)
```

$$I3 := b1 - b2 + da$$

```
> solution:=solve({I1,I3},{b1,b2});
> % solution of I1 and I3
```

$$solution := \{b2 = \frac{E1\,h1\,da}{E2\,h2 + E1\,h1},\ b1 = -\frac{da\,E2\,h2}{E2\,h2 + E1\,h1}\}$$

```
> factor(subs(solution,{sigma1=E1*epsilon1,sigma2=E2*epsilon2}));
> %elastic stresses
```

$$\{\sigma 1 = -\frac{da\,E2\,h2\,E1}{E2\,h2 + E1\,h1},\ \sigma 2 = \frac{E1\,h1\,da\,E2}{E2\,h2 + E1\,h1}\}$$

```
> M:=factor(subs(solution,I2));
> %external moment M needed to keep the sample straight
```

[1] http://www.maplesoft.com

$$M := -\frac{1}{2}\,\frac{E1\,h1\,da\,E2\,h2\,(h2+h1)}{E2\,h2+E1\,h1}$$

```
> epsilon0:=simplify(subs(da=dt*(alpha1-alpha2),subs(solution,b1+dt*alp
> ha1)));
```

> %elastic strain of the whole composite

$$\varepsilon 0 := \frac{dt\,(E2\,h2\,\alpha 2+\alpha 1\,E1\,h1)}{E2\,h2+E1\,h1}$$

Appendix C

Calculation of Young's modulus in flexion

The source code is meant for MAPLE[1] version 6.01. Listing of flexion.mws:

```
> restart;
```

```
> epsilon1:=b+y/R;
```

$$\varepsilon 1 := b + \frac{y}{R}$$

```
> epsilon2:=b+y/R;
> % elastic strains; boundary condition holds as b1=b2=b
```

$$\varepsilon 2 := b + \frac{y}{R}$$

```
> I1:=int(epsilon2*E2,y=-h2..0)+int(epsilon1*E1,y=0..h1);
> % sum of all forces = 0
```

$$I1 := -\frac{1}{2}\frac{E2\,h2^2}{R} + b\,E2\,h2 + \frac{\frac{1}{2}E1\,h1^2}{R} + b\,E1\,h1$$

```
> I2:=int(epsilon2*E2*y,y=-h2..0)+int(epsilon1*E1*y,y=0..h1)-M;
> % sum of all moments = M
```

$$I2 := \frac{1}{3}\frac{E2\,h2^3}{R} - \frac{1}{2}\,b\,E2\,h2^2 + \frac{\frac{1}{3}E1\,h1^3}{R} + \frac{1}{2}\,b\,E1\,h1^2 - M$$

```
> solution_ii:=factor(solve({I1,I2},{R,b}));
> % solution of I1 and I2
```

[1] http://www.maplesoft.com

$$solution\_ii := \{$$

$$R = \frac{1}{12}\,\frac{E2^2\,h2^4 + 4\,E2\,h2^3\,E1\,h1 + 6\,E2\,h2^2\,E1\,h1^2 + 4\,E1\,h1^3\,E2\,h2 + E1^2\,h1^4}{M\,(E2\,h2 + E1\,h1)},$$

$$b = 6\,\frac{(E2\,h2^2 - E1\,h1^2)\,M}{E2^2\,h2^4 + 4\,E2\,h2^3\,E1\,h1 + 6\,E2\,h2^2\,E1\,h1^2 + 4\,E1\,h1^3\,E2\,h2 + E1^2\,h1^4}\}$$

```
> epsilon:=b+y/R;
```

> % strain for one component material

$$\varepsilon := b + \frac{y}{R}$$

```
> I1:=int(epsilon*E,y=-h2..h1);
```

> % sum of all forces = 0

$$I1 := \frac{1}{2}\,\frac{E\,(h1^2 - h2^2)}{R} + b\,E\,(h1 + h2)$$

```
> I2:=int(epsilon*E*y,y=-h2..h1)-M;
```

> % sum of all moments = M

$$I2 := \frac{1}{3}\,\frac{E\,(h1^3 + h2^3)}{R} + \frac{1}{2}\,b\,E\,(h1^2 - h2^2) - M$$

```
> solution_i:=factor(solve({I1,I2},{R,b}));
```

> % solution of I1 and I2

$$solution\_i := \{R = \frac{1}{12}\,\frac{E\,(h1 + h2)^3}{M},\ b = 6\,\frac{(h2 - h1)\,M}{E\,(h1 + h2)^3}\}$$

```
> temp:=subs(solution_i,solution_ii);
```

> % R should be the same in 1 or 2 component case for the same M

$$temp := \{\frac{1}{12}\,\frac{E\,(h1 + h2)^3}{M} =$$

$$\frac{1}{12}\,\frac{E2^2\,h2^4 + 4\,E2\,h2^3\,E1\,h1 + 6\,E2\,h2^2\,E1\,h1^2 + 4\,E1\,h1^3\,E2\,h2 + E1^2\,h1^4}{M\,(E2\,h2 + E1\,h1)},$$

$$6\,\frac{(h2 - h1)\,M}{E\,(h1 + h2)^3} =$$

$$6\,\frac{(E2\,h2^2 - E1\,h1^2)\,M}{E2^2\,h2^4 + 4\,E2\,h2^3\,E1\,h1 + 6\,E2\,h2^2\,E1\,h1^2 + 4\,E1\,h1^3\,E2\,h2 + E1^2\,h1^4}\}$$

```
> E:=simplify(solve(temp[1],E));
```

> % the average elastic modulus of the composite in flexion

$$E := \frac{E2^2\,h2^4 + 4\,E2\,h2^3\,E1\,h1 + 6\,E2\,h2^2\,E1\,h1^2 + 4\,E1\,h1^3\,E2\,h2 + E1^2\,h1^4}{(E2\,h2 + E1\,h1)\,(h1 + h2)^3}$$

Bibliography

M. Abedl-Rahman, E. Badawi, E. M. Hassan, and G. Yahya. Formation energy in Al-Mg alloy by positron annihilation lifetime technique (PALT). *Turkish Journal of Physics*, 26: 381–389, 2002.

P. A. Bancel and P. A. Heiney. Icosahedral aluminium-transition-metal alloys. *Physical Review*, B33:7917–7922, 1986.

F. Banhart and P. M. Ajayan. Carbon onions as nanoscopic pressure cells for diamond formation. *Nature*, 382:443, 1996.

J. G. Bednorz and K. A. Müller. *Zeitschrift für Physik*, B64:189, 1986.

J. Belson, D. Lemercier, P. Moser, and P. Vigier. Concentration dependence of internal friction in Al-Mg alloy. *Physica Status Solidi*, 40:647–655, 1970.

L. Bendersky. Quasicrystal with one-dimensional translational symmetry and a tenfold rotational axis. *Physical Review Letters*, 55:1461–1463, 1985.

M. F. Besser and T. Eisenhammer. *MRS Bulletin*, 59:69, 1997.

R. Busch. The thermophysical properties of bulk metallic glass-forming liquids. *The Journal of the Minerals, Metals & Materials Society*, 52:39, 2000.

J. W. Cahn, D. Shechtman, and D. Gratias. Indexing of icosahedral quasiperiodic crystals. *Journal of Materials Research*, 1:13–26, 1986.

Y. Calvayrac, A. Quivy, M. Bessière, S. Lefebvre, M. Cornier-Quinquandon, and D. Gratias. Icosahedral AlCuFe alloys: towards ideal quasicrystals. *Journal de Physique*, 51: 417–431, 1990.

W. Cao, H. Q. Ye, and K. H. Kuo. A new octagonal quasicrystal and related crystalline phases in rapidly solidified Mn_4Si. *Physica Status Solidi (a)*, 107:511–519, 1988.

E. Carreño-Morelli, T. Cutard, R. Schaller, and C. Bonjour. Processing and characterization of aluminium-based MMCs produced by gas pressure infiltration. *Materials Science and Engineering A*, 251:48–57, 1998.

K. Chattopadhyay, S. Lele, N. Thangaraj, and S. Ranganathan. Vacancy ordered phases and one-dimensional quasiperiodicity. *Acta Metallurgica*, 35:727–733, 1987.

H. Chen, D. X. Li, and K. H. Kuo. New type of two-dimensional quasicrystal with twelvefold rotational symmetry. *Physical Review Letters*, 60:1645–1648, 1988.

T. Christman, A. Needleman, and S. Suresh. *Acta Metallurgica*, 37(11):3029, 1989.

T. W. Clyne and P. J. Withers. *An Introduction to Metal Matrix Composites*. Cambridge University Press, 1993.

M. Cornier-Quiquandon, A. Quivy, S. Lefebvre, E. Elkaim, G. Heger, A. Katz, and D. Gratias. Neutron-diffraction study of icosahedral Al-Cu-Fe single quasicrystals. *Physical Review*, B44(5):2071–2084, 1991.

B. Damson, M. Weller, M. Feuerbacher, B. Gruschko, and K. Urban. *Journal of Alloys and Compounds*, 310:184, 2000a.

B. Damson, M. Weller, M. Feuerbacher, B. Gruschko, and K. Urban. Mechanical spectroscopy of i-Al-Pd-Mn and d-Al-Ni-Co. *Materials Science and Engineering A*, 294–296: 806–809, 2000b.

N. G. de Brujin. *Mathematics proceedings*, A84, 1981.

P. G. de Gennes. Quelques états de la matière. *Helvetica Physica Acta*, 57:157, 1984.

C. Dong and J. M. Dubois. Quasicrystals and crystalline phases in $Al_{65}Cu_{20}Fe_{10}Cr_5$ alloy. *Journal of Materials Science*, 26:1647–1654, 1991.

C. Dong, Z. K. Hei, L. B. Wang, Q. H. Song, and Y. K. Wu anf K. H. Kuo. A new icosahedral quasicrystal in rapidly solidified $FeTi_2$. *Scripta Metallurgica*, 20:1155–1158, 1986.

J. M. Dubois, S. S. Kang, and J. von Stebut. Quasicrystalline low-friction coatings. *Journal of Materials Science Letters*, 10:537–541, 1991.

H. Ehmler, A. Heesemann, K. Rätzke, and F. Faupel. Mass dependence of diffusion in a supercooled metallic melt. *Physical Review Letters*, 80:4919, 1999.

E. Fleury, S. M. Lee, G. Choi, W. T. Kim, and D. H. Kim. Comparison of Al-Cu-Fe quasicrystalline particle reinforced Al composites fabricated by conventional casting and extrusion. *Journal of Materials Science*, 36:963–970, 2001.

K. K. Fung, C. Y. Yang, Y. Q. Zhou, J. G. Zhao, W. S. Zhan, and B. G. Shen. Icosahedrally related decagonal quasicrystal in rapidly cooled Al-14-at.%-Fe alloy. *Physical Review Letters*, 56:2060–2063, 1986.

F. W. Gayle, A. J. Shapiro, F. S. Biancaniello, and W. J. Boettinger. *Metallurgical and Materials Transactions A*, 23:2409, 1992.

E. Giacometti. *Contribution à l'étude des propriétés mécaniques de l'alliage quasicristallin icosaédrique Al-Cu-Fe*. Thèse N° 2088, Ecole Polytechnique Fédérale de Lausanne, 1999.

E. Giacometti, N. Baluc, and J. Bonneville. Activation parameters of plastic flow in icosahedral Al-Cu-Fe. *Philosophical Magazine Letters*, 79(1):1–7, 1999.

E. Giacometti, N. Baluc, and J. Bonneville. Creep behaviour of icosahedral Al-Cu-Fe. *Materials Science and Engineering A*, 294–296:777–780, 2000.

E. Giacometti, P. Guyot, N. Baluc, and J. Bonneville. Plastic behaviour of icosahedral Al-Cu-Fe quasicrystals: experiment and modelling. *Materials Science and Engineering A*, 319–321:429–433, 2001.

D. Gratias, J. W. Cahn, and B. Mozer. Six-dimensional Fourier analysis of the icosahedral $Al_{73}Mn_{21}Si_6$ alloy. *Physical Review*, B38:1643–1646, 1988.

D. Gratias, Y. Calvayrac, J. Devaud-Rzepski, F. Faudot, M. Harmelin, A. Quivy, and P. A. Bancel. The phase diagram and structures of the ternary AlCuFe system in the vicinity of the icosahedral region. *Journal of Non-Crystlline Solids*, 153–154:482–488, 1993.

P. Guyot and G. Canova. The plasticity of icosahedral quasicrystals. *Philosophical Magazine*, A79(11):2815–2832, 1999.

L. X. He, X. Z. Li, Z. Zhang, and K. H. Kuo. One-dimensional quasicrystal in rapidly solidified alloys. *Physical Review Letters*, 61:1116–1118, 1988a.

L. X. He, Y. K. Wu, and K. H. Kuo. Decagonal quasicrystals with different periodicities along the tenfold axis in rapidly solidified $Al_{65}Cu_{20}M_{15}$ (M=Mn, Fe, Co, or Ni). *Journal of Materials Science*, 7:1284–1286, 1988b.

R. Hill. *The Mathematical Theory of Plasticity*. Clarendon Press, Oxford, 1950.

S. Iijima. Helical microtubules of graphitic carbon. *Nature*, 354:56, 1991.

T. Ishimasa, H.-U. Nissen, and Y. Fukano. New ordered state between crystalline and amorphous in Ni-Cr particles. *Physical Review Letters*, 55:511–513, 1985.

M. G. Karkut, J.-M. Triscone, D. Ariosa, and Ø. Fischer. Quasiperiodic metallic multilayers: Growth and superconductivity. *Physical Review*, B34:4390–4393, 1986.

K. F. Kelton and P. C. Gibbons. Hydrogen storage in quasicrystals. *MRS Bulletin*, 22:69, 1997.

K. F. Kelton, P. C. Gibbons, and P. N. Sabes. New icosahedral phases in Ti-transition metal alloy. *Physical Review*, B38:7810–7813, 1988.

J. Kong, C. Zhou, S. Gong, and H. Xu. Low pressure plasma sprayed Al-Cu-Fe-Cr quasicrystalline coating for Ti-base alloy oxidation protection. *Surface and Coatings Technology*, submitted, 2002.

A. M. Korsunsky, A. I. Salimon, I. Pape, A. M. Polyakov, and A. N. Fitch. The thermal expansion coefficient of mechanically alloyed Al-Cu-Fe quasicrystalline powders. *Scripta Materialia*, 44:217–222, 2001.

H. W. Kroto, J. R. Heath, S. C. O'Brien, R. F. Curl, and R. E. Smalley. C60: buckminsterfullerene. *Nature*, 318:162, 1985.

K. H. Kuo. Some new icosahedral and decagonal quasicrystals. *Material Science Forum*, 22–24:131–140, 1987.

K. H. Kuo, D. S. Zhou, and D. X. Li. Quasicrystalline and Frank-Kasper phases in a rapidly solidified $V_{41}Ni_{36}Si_{23}$ alloy. *Philosophical Magazine Letters*, 55:33–37, 1987.

L. Landau and E. Lifchitz. *Théorie de l'élasticité*. Editions Mir, Moscou, 1967.

S. M. Lee, J. H. Jung, E. Fleury, W. T. Kim, and D. H. Kim. Metal matrix composites reinforced by gas-atomised Al-Cu-Fe powders. *Materials Science and Engineering A*, 294–296:99–103, 2000.

S. Y. Li, H. H. Zhou, J. L. Gu, and J. Zhu. Does carbyne really exist? — carbynes in expanded graphite. *Carbon*, 38(6):934–937, 2000.

A. L. Mackay. *Sov. Phys. Cristallogr.*, 26:517, 1981.

A. L. Mackay. Crystallography and the Penrose pattern. *Physica*, 114A:609–613, 1982.

Z. Mai, B. Zhang, M. Hui, Z. Huang, and X. Chen. Study of large size quasicrystal in Al_6CuLi_3 alloy. *Material Science Forum*, 22–24:591–600, 1987.

A. Mourisco, N. Baluc, J. Bonneville, and R. Schaller. Mechanical loss spectrum of Ni_3(Al,Ta) single crystals. *Materials Science and Engineering A*, 239–240:281–286, 1997.

J.-O. Nilsson, A. Hultin Stigenberg, and P. Liu. Isothermal formation of quasicrystalline precipitates and their effect on strength in a 12Cr-9Ni-4Mo maraging stainless steel. *Metallurgical and Materials Transactions A*, 25:2225–2233, 1994.

Y. Nishino and S. Asano. The constitutive equations for internal friction in thin-layer materials. *Physica Status Solidi (a)*, 193(2):K97–K100, 1993.

A. S. Nowick and B. S. Berry. *Anelastic relaxation in crystalline solids*. Academic Press, New York and London, 1972.

R. Penrose. *The Bulletin of the Institute of Mathematics and its Applications*, 10, 1974.

S. J. Poon, A. J. Drehmann, and K. R. Lawless. Glassy to icosahedral phase transformation in Pd-U-Si alloys. *Physical Review Letters*, 55:2324–2327, 1985.

V. Rékatch. *Théorie de l'élasticité*. Editions Mir, Moscou, 1980.

J. P. Salvetat, G. A. D. Briggs, J. M. Bonard, R. R. Bacsa, A. J. Kulik, T. Stöckli, N. A. Burnham, and L. Forró. Elastic and shear moduli of single-walled carbon nanotube ropes. *Physical Review Letters*, 82:944, 1999a.

J. P. Salvetat, A. J. Kulik, J. M. Bonard, G. A. D. Briggs, T. Stöckli, K. Méténier, S. Bonnamy, F. Béguin, N. A. Burnham, and L. Forró. Elastic modulus of ordered and disordered multiwalled carbon nanotubes. *Advanced Materials*, 11:161, 1999b.

R. Schaller. private communication, 2001.

G. Schoeck, E. Bisogni, and J. Shyne. *Acta Metallurgica*, 12:1466, 1964.

F. Semadeni, N. Baluc, and J. Bonneville. Mechanical properties of Al-Li-Cu icosahedral quasicrystals. *Materials Science and Engineering A*, 234–236:291–294, 1997.

D. Shechtman, I. Blech, D. Gratias, and J. W. Cahn. *Physical Review Letters*, 53:1951–1953, 1984.

H.-R. Sinning, R. Scarfone, and I. S. Golovin. Mechanical spectroscopy of hydrogen-absorbing quasicrystals. *Materials Science and Engineering A*, submitted, 2002.

D. J. Sordelet, S. D. Widener, Y. Tang, and M. F. Besser. Characterization of a commercially produced Al-Cu-Fe-Cr quasicrystalline coating. *Materials Science and Engineering A*, 294–296:834–837, 2000.

W. Steurer. The structure of quasicrystals. *Zeitschrift für Kristallographie*, 190:179–234, 1990.

G. G. Stoney. *Proceedings of the Royal Society*, A82(172), 1909.

H. Takagi, S. Uchida, K. Kitazawa, and S. Tanaka. *Japanese Journal of Applied Physics*, 26: L 123, 1986.

T. Takeuchi, Y. Yamada, T. Fukunaga, and U. Mizutani. Studies of Mg-Al-Pd icosahedral quasicrystals and approximant crystals synthesized by the mechanical alloying process. *Materials Science and Engineering A*, 181–182:828–832, 1994.

J. Todd, R Merlin, R. Clarke, K. M. Mohanty, and J. D. Axe. Synchrotron X-ray study of a Fibonacci superlattice. *Physical Review Letters*, 57:1157–1160, 1986.

A. P. Tsai, K. Aoki, A. Inoue, and T. Masumoto. *Journal of Materials Research*, 8:5, 1993.

A. P. Tsai, A. Inoue, and T. Masumoto. New quasicrystals in $Al_{65}Cu_{20}M_{15}$ (M=Cr, Mn or Fe) systems prepared by rapid solidification. *Journal of Materials Science Letters*, 7: 322–326, 1988.

A. P. Tsai, Y. Yokoyama, A. Inoue, and T. Masumoto. Quasicrystals in Al-Pd-TM (TM=transition metal) systems prepared by rapid solidification. *Japanese Journal of Applied Physics*, 29:L 1161–L 1164, 1990.

A. C. Ugural and S. K. Fenster. *Advanced strength and applied elasticity*. Elsevier, 1986.

B. Vittoz, B. Secrétan, and B. Martinet. Frottement interne et anélasticité des solides. *Zeitschrift für angewandte Mathematik und Physik*, 14:46–69, 1963.

N. Wang, H. Chen, and K. H. Kuo. Two-dimensional quasicrystal with eightfold rotational symmetry. *Physical Review Letters*, 59:1010–1013, 1987.

N. Wang, K. K. Fung, and K. H. Kuo. Symmetry study of the Mn-Si-Al octagonal quasicrystal by convergent beam electron diffraction. *Applied Physics Letters*, 52:2120–2121, 1988.

Z. M. Wang and K. H. Kuo. The octagonal quasilattice and electron diffraction patterns of the octagonal phase. *Acta Crystallographica*, A44:857–863, 1988.

M. Weller. Anelastic relaxation of point defects in cubic crystals. *Journal de Physique IV*, 6(C8):63, 1996.

M. Weller. Thin-layer materials. *Material Science Forum*, 366–368:549–559, 2001.

A. Yamamoto and K. N. Ishihara. Penrose patterns and related structures. II. Decagonal quasicrystals. *Acta Crystallographica*, A44:707–714, 1988.

I. Yoshida, T. Sugai, S. Tani, M. Motegi, K. Minamida, and H. Hayakawa. Automation of internal friction measurement apparatus of inverted torsion pendulum type. *Journal of Physics E*, 14:1201–1206, 1981.

H. Zhang and K. H. Kuo. The decagonal quasicrystal and its orientation relationship with the vacancy ordered CsCl phase in Al-Cu-Ni alloy. *Scripta Metallurgica*, 23:355–358, 1989.

X. Zhang, R. M. Stroud, J. L. Libbert, and K. F. Kelton. *Philosophical Magazine*, B70:927, 1994.

Z. Zhang, H. Q. Ye, and K. H. Kuo. A new icosahedral phase with m35 symmetry. *Philosophical Magazine*, A52:L49–L52, 1985.

Acknowledgements

I would like to particularly thank Dr. Robert Schaller and Dr. Nadine Baluc who closely guided this work with a great deal of enthusiasm and patience. They were always available for efficient discussions, tolerant and open-minded.

This work has been performed at the Laboratoire de Génie Atomique which became Institut de Physique de la Matière Complexe, in the group of Prof. Willy Benoit. I would like to thank him for accepting me into his group and for his constructive remarks and advice.

I wish to express my thanks to Dr. Tomáš Kruml for his help with TEM observations, compression tests, and proofreading the manuscript.

I am grateful to Nathalie Guilbaud for her contribution to the study of the metal matrix composites during her stay at EPFL.

This thesis would not have been possible without the efficient help of Bernard Guisolan who performed a lot of work in repairing the pendulum, preparing the infiltrated samples, and mounting them. I am grateful to Philippe Bugnon for teaching me how to utilise the X-ray diffractometer and the furnaces. Gérald Beney deserves my thanks for sample cutting and polishing. I thank Alessandro Ichino for keeping the electronics always working.

I gratefully acknowledge Centre Interdépartemental de Microscopie Electronique at EPFL for providing the microscopy facilities as well as Fonds National Suisse de la Recherche Scientifique for the financial support.

I thank also my past and present colleagues for the nice atmosphere during the three and half years I spent at IGA and IPMC.

Finally, I would like to thank my girlfriend Jana for correcting my English and for supporting me during these years.

Curriculum Vitæ

Jan Fikar

born on 17th January 1974 in Znojmo, the Czech republic, Czech nationality

Education:

- **1999 - 2003:** Assistant and postgraduate studies at Institut de Physique de la Matière Complexe (IPMC), Ecole Polytechnique Fédérale de Lausanne (EPFL), specialisation in mechanical properties of quasicrystals, Ph.D. thesis director Dr. N. Baluc and Dr. R. Schaller.
- **1997 - 1999:** Assistant at Masaryk University (MU) Brno, the Czech republic, Department of Theoretical Physics and Astrophysics, specialisation in general relativity.
- **1992 - 1997:** M.Sc. in physics on "Exact Axially Symmetric Solutions of Einstein-Maxwell Equations" at MU, the Faculty of Science.
- **1988 - 1992:** Grammar school specialised in mathematics.

Didactic activities:

- **2001 - 2002:** Assistant in the advanced laboratory work in physics of Dr. Sanjinés at EPFL.
- **1999 - 2001:** Assistant in the laboratory work in physics of Dr. Schaller and Dr. Gremaud at EPFL.
- **1997 - 1999:** Assistant in the course of complex mathematical analysis of Dr. Musilová at MU.

Publications:

- J. Fikar, R. Schaller, and N. Baluc: Mechanical spectroscopy of Al-Cu-Fe quasicrystalline coatings, accepted to *Materials Science and Engineering A*, 2002.
- J. Fikar, C. Dupas, B. Viguier, and T. Kruml: Searching for the proper law of dislocation multiplication in covalent crystals, *Journal of Physics: Condensed Matter*, 14(48):12887–12895, 2002.
- E. Giacometti, J. Fikar, N. Baluc, and J. Bonneville: Mechanical behaviour versus structure of $Al_{63.6}Cu_{24.0}Fe_{12.4}$, *Philosophical Magazine Letters*, 82(4):183–189, 2002.
- J. Fikar, R. Schaller, N. Guilbaud, and N. Baluc: Mechanical spectroscopy of icosahedral Al-Cu-Fe quasicrystals metal-based composites, *Defect and Diffusion Forum*, 203–205:289–292, 2002.
- J. Fikar, J. Bonneville, J. Rabier, N. Baluc, A. Proult, P. Cordier, and I. Stretton: Low temperature behaviour of icosahedral Al-Cu-Fe quasicrystals, *Materials Research Society Symposium Proceedings*, 643:K7.4, 2001.
- J. Fikar, N. Baluc, J. Bonneville, and P. Guyot: High temperature plastic behaviour of icosahedral Al-Cu-Fe quasicrystals, *Materials Research Society Symposium Proceedings*, 643:K7.3, 2001.
- J. Fikar and J. Horský: Generating conjecture and Einstein-Maxwell field of plane symmetry, *Czechoslovak Journal of Physics*, 49(10):1423-1432, 1999, http://arxiv.org/abs/gr-qc/0004028.

Conferences without proceedings:

- J. Fikar, N. Baluc, and R. Schaller: Mechanical spectroscopy of icosahedral quasicrystals metal-based composites, *Plasticité*, Lyon, 2002.
- J. Fikar, N. Baluc, J. Bonneville, P. Guyot: Plasticité à haute température de la phase quasicristalline AlCuFe, *Plasticité*, Toulouse, 2001.
- J. Fikar, J. Bonneville, J. Rabier, N. Baluc, A. Proult, P. Cordier, and I. Stretton: Plasticité à basse température de quasicristaux à structure icosaédrique, *Plasticité*, Toulouse, 2001.
- J. Fikar, R. Schaller, N. Baluc, and J. Bonneville: Powder metallurgy of icosahedral Al-Cu-Fe, *Groupement Quasicristaux*, Marseille, 2000.